Geophysical modelings of co- and postseismic gravity changes from satellite gravimetry

（衛星重力観測に基づいた地震時及び地震後重力変化の地球物理学的なモデル構築）

Yusaku Tanaka

Department of Natural History Sciences, Graduate School of Science,
Hokkaido University

Submitted for the degree of Doctor of Philosophy

February 2017

Contents

Abstract

Space geodesy is a practice in which we perform geophysical studies based on geodetic data observed using space techniques. It has been providing large advances to various disciplines in earth and environmental sciences. Some of them comes from satellite gravimetry. For example, the earth's static global gravity field has been a target of space geodetic studies since its early age, and first space geodetic determination of the flattering of the earth dates back to 1950s.

The GRACE (Gravity Recovery And Climate Experiment) satellite system, launched in 2002, has enabled us to track the time-variable gravity field with spatial resolution of ~300 km and the temporal resolution of ~30 days. There are numbers of geophysical phenomena accompanying mass redistribution and consequent changes in the gravity field. Tracking such changes help us investigate physical processes governing the phenomena.

An earthquake also causes mass redistribution, and has been a scientific target of time-variable gravity studies. The present study aims at finding new insights into physical processes associated with earthquakes through the analysis of gravity changes and providing an overview on earthquake-origin gravity changes. This thesis is separated into seven chapters. In Chapters 1 – 6, I give detailed seismological studies made by analyzing GRACE data. In Chapter 7, I conclude the thesis. Summaries of Chapters 1 – 6 are given below.

[Chapter 1] Introduction

Space-geodesy includes seismology based on the satellite gravimetry. This aims to reveal physical processes of earthquakes from mass redistribution through observing gravity changes. I also briefly review the history of satellite gravimetry.

[Chapter 2] Data processing

The GRACE data are provided by several data analysis centers. In this study, those by UTCSR (Level-2, RL05) are mainly used, and I apply several kinds of noise reduction filters to them. The contributions of terrestrial water storage are often reduced by the GLDAS model, one of the land hydrological models. Gravity time series at grid points with 1 degree separation in longitude and latitude are individually fit to appropriate functions by using the least-squares method. Other approaches are also reviewed in this chapter.

[Chapter 3] Phenomena responsible for gravity changes

In order to distinguish gravity changes related to earthquakes, we need knowledge about other phenomena that may change gravity fields. Such phenomena include seasonal movements of soil moisture, melting of mountain glaciers and continental ice sheets, anthropogenic groundwater depletion, and glacial isostatic adjustment.

[Chapter 4] Coseismic gravity changes

Theoretical models for coseismic gravity changes have been established decades ago, and the validity of such models have been tested repeatedly by GRACE observations coseismic gravity changes. This thesis also includes the study on the

mechanism of gravity changes associated with the 2013 Okhotsk deep-focus earthquake. Now, we could compare earthquake fault parameters derived from gravity change observations with those derived by seismological observations. One of the merits of satellite gravimetry is that we can observe gravity changes both on land and ocean with uniform accuracies.

[Chapter 5] Postseismic gravity changes

Two major processes responsible for postseismic gravity changes are considered to be afterslips and viscoelastic relaxation from both observational and theoretical points of view. However, it is often difficult to separate signals from the two processes espatially by surface displacement observations using GNSS stations on land. On the other hand, gravity changes by the two processes might emerge in opposite polarities, and this let us separate the two processes easily.

[Chapter 6] Coseismic and long-term postseismic gravity changes of the 2004 Sumatra-Andaman earthquake revisited with the latest GRACE data

The 2004 Sumatra-Andaman earthquake is the first very large earthquake after the launch of the GRACE satellites in 2002. In this study, I analyze the time series of various components of the gravity, i.e., (1) vertical component, (2) north component, and (3) up component of the gradient of the vertical component of the gravity changes using the GRACE data sets from two analysis centers (UTCSR and CNES/GRGS). All these time series suggest that the postseismic gravity changes of the 2004 Sumatra-Andaman earthquake have almost ended. These observation data help us determine time scales of the postseismic gravity changes and to constrain viscosity

structure of the upper mantle. Moreover, it may allow us to research interseismic gravity changes because the static gravity anomaly is formed by the repeat of inter-, co-, and postseismic gravity changes and the static anomaly and co- and postseismic gravity changes are being revealed.

概要

人工衛星データに代表される宇宙測地技術を利用した地球科学，すなわち宇宙測地学は 1950 年代に始まり，今日までに宇宙測地学は地球科学の様々な分野で多くの成果を上げてきた．特に静的な地球重力場の研究は，宇宙測地学の黎明期に，人工衛星の軌道とその変化の観測に始まり，地球の扁平率の測定などで地球科学の発展に貢献した．

2002 年に打ち上げられた人工衛星 GRACE (Gravity Recovery And Climate Experiment) は，静的な地球重力場や数千 km という長波長成分の時間変化のみならず，時間分解能およそ 1 か月・空間分解能およそ 300 km という精度で重力の時間変化の追跡を可能にした．地球上で起こる様々な自然現象の多くは質量移動を伴う．それらを重力変化観測によって追跡する事によって，地球上で起こっている様々な現象の物理過程が解き明かされるのである．

人工衛星 GRACE が可能にした研究の一つは, 地震に伴う重力変化の観測研究である．本研究の目的は，衛星重力観測に基づく重力時系列の解析によって，地震に伴う重力変化に関連した新たな知見を得ること，および現在までにこの分野で明らかにされた知見を整理してまとめることである. 本論文では全体を 7 つの章(Chapter)に分け，まず 6 つの Chapter で「重力衛星 GRACE に基づいた地震学」の全体像を体系的に整理して詳細を述べ，その中でも特に本研究で初めて明らかになったことについて詳しく説明する．Chapter 7 は全体のまとめである．最初の 6 つの Chapter の概要は以下の通りである．

[Chapter 1] 導入

宇宙測地学は，その目的を人工衛星や宇宙技術を用いて得られた測地データ

に基づいて達成しようとする学問である．その中には，人工衛星 GRACE を始めとした重力観測衛星のデータを利用して行われる地震研究がある．この研究は，地震に伴う質量の移動を捉え，そこから地震現象が内包する物理過程の解明に貢献しようとするものである．

[Chapter 2] データ及びデータ解析の手法

人工衛星 GRACE のデータは複数の研究機関から公開されている．本研究では主に UTCSR が球面調和関数の係数として公開する Level-2，RL05 データを用いた．データ解析の際にはファンフィルターと縦縞除去フィルターというノイズ軽減フィルターを用いている．地震に伴う重力変化の解析には，ノイズとなる陸水のシグナルの補正に様々な陸水モデルが用いられる場合があり，本研究の中にも，その中の一つ GLDAS モデルを用いている部分がある．本研究では時系列解析は全球的な球面調和関数の展開係数から，経緯 1 度刻みのグリッド点ごとに時系列データを作成した上で，その時系列に最小二乗法で関数を当てはめて行なっている．更に，ここでは本研究で使われた手法以外の方法も紹介する．

[Chapter 3] 重力変化を引き起こす諸現象

地震に伴う重力変化を識別するためには地震以外に起因する重力変化についての知識が必要である．たとえば陸水の季節的な移動や，氷河・氷床の融解，人為的な灌漑に伴う地下水の枯渇，後氷期回復である．

[Chapter 4] 地震時重力変化

地震時の重力変化の理論は以前からあり，GRACE 打ち上げ後に発生した地震の重力観測によってそれらが検証された．特に本研究では 2013 年に発生したオ

ホーツク深発地震(M_w8.3)の地震時重力変化の主要因が地表の上下変位であることを突き止めた．地震時重力変化の観測結果は今後，たとえば他の観測に基づいて仮定された地震の物理過程が，海域まで含めた重力の観測結果を説明しうるかを検証するような目的で利用されるだろう．

[Chapter 5] 地震後重力変化

地震後変動の物理過程は，観測と理論の双方の観点から，短期的にはアフタースリップ，長期的にはマントルの粘性緩和が支配的であると考えられている．しかし現状では観測データに含まれる各々のシグナルの十分な分離は困難である．本研究では，沈み込み帯で発生した地震の地震後変動に関して，短期・長期成分が島弧上の GNSS では同じ極性で観測される一方，重力変化では異なった極性で観測される事を発見した．これは地震後の物理過程の解明に役立つ可能性がある．

[Chapter 6] 最新のデータを利用した 2004 年スマトラーアンダマン地震に伴う重力変化の再解析

2004 年スマトラーアンダマン地震は 2002 年 GRACE 打ち上げ後に最初に起こった大地震である．本研究では，重力の下向き成分と北向き成分，そして下向き重力の上下方向の勾配という 3 種類の成分の時系列を，UTCSR 及び CNES/GRGS という 2 機関が公開する最新のデータを利用し，計 6 種の時系列解析を行なった．いずれの結果も 2004 年スマトラーアンダマン地震に伴う地震後の重力変化が，現時点でほとんど終息していることを示唆した．更に継続的な調査を要するものの，これは粘性緩和の時間スケールを拘束できる結果であり，たとえば上部マントルの粘性構造を知る上で有用であろう．また，現在知られ

ている静的な重力異常が地震間・地震時・地震後の重力変化が繰り返されながら形成されていることから，地震時と地震後の重力変化の合算を静的な重力異常と比較することで，地震間の重力変化についても調査できるようになる可能性があることを示した.

Acknowledgment

I would like to express my profound gratitude to everyone who has helped and supported me.

First, my deepest gratitude goes to my supervisor, Prof. Kosuke Heki. He always gave me warm eyes, many advices, many chances for me to take part in scientific meetings, jobs as a teaching assistant to solve my economic problems, and everything I needed. Moreover, his studies and presentations are always interesting to me, which have also encouraged me to study more. I would like to show my appreciation to him but it is beyond description.

I thank Prof. Masato Furuya, Assoc. Prof. Youichiro Takada, Prof. Makoto Murakami, Prof. Kiyoshi Yomogida, Assoc. Prof. Kazunori Yoshizawa, Prof. Emeritus Junji Koyama, and Prof. Shoshiro Minobe. They gave me constructive comments for my study. Also, I strongly thank Dr. Koji Matsuo at Geospatial Information Authority of Japan and Dr. Nikolay V. Shestakov at Far Eastern Federal University. I did my study shown in Chapter 4 and Chapter 5 with the cooperation of them. And I thank Assistant Prof. Yoshiyuki Tanaka at Tokyo University. Figure 5.6 is made from the calculation data given by him.

I would like to show my appreciation to JSPS for a grant and I am grateful to every center giving scientific data I used in this thesis.

Last but not least, I give my sincere gratitude to my family and friends. Without them, I could not have completed this thesis.

Chapter 1
Introduction

1.1 Purpose and outline of this thesis

Through this study, I try to understand physical processes in earthquake cycles of subduction zones based on satellite gravimetry. In this thesis I provide a comprehensive review about what has already been revealed, and detailed description of my own results.

Chapter 1 describes several important points in the background of the study. Chapter 2 explains data mainly used in this study and standard procedures of time series analysis. Chapter 3 introduces several geophysical phenomena giving rise to gravity changes that we need to understand to isolate gravity changes due to earthquakes. Then, Chapter 4 gives brief reviews related to the theories, observation results, discussions, about coseismic gravity changes. Those of postseismic gravity changes are given in Chapter 5. Chapter 6 compares several examples of analyses based on latest GRACE data sets about the gravity changes associated with the 2004 Sumatra-Andaman earthquake. At last, Chapter 7 concludes this thesis.

Our review article about satellite gravimetry for earthquake studies has already been in press (Tanaka and Heki, 2016), and some parts of this thesis overlap with that

paper.

1.2 Space-geodesy in geophysics

Geophysics is the discipline in which we study phenomena in the solar system with physical approaches. Space geodesy serves this purpose using space techniques as represented by artificial satellites orbiting the earth, and other celestial bodies. It originates from 1957, when the first artificial satellite “Sputnik-1” was launched by the Soviet Union, and then it has been applied to many disciplines in earth science, contributing to their advances. For instance, Global Navigation Satellite System (GNSS) and Synthetic Aperture Radar (SAR) became important tools for seismology, volcanology, meteorology, solar terrestrial physics, and so on. VLBI (Very Long Baseline Interferometry) and SLR (Satellite Laser Ranging) proved the plate tectonics by the observation of the surface movement of the earth in 1980s.

The observations using artificial satellites are often superior to ground-based observations in various aspects. As for satellite gravity data, satellites keep providing observation data until they stop functioning and huge amount of data are available to researchers, offering scientists chances to use them. One more aspect for gravity satellites is that they provide two-dimensional observation data with uniform and very high quality. Today, for example, you can get information of the ground deformation or sea level with the accuracy of several mm, ionosphere with several TECU (Total Electron Content Unit), gravity field with several μGal (1 Gal = 1 cm/s^2). This cannot be achieved by simply deploying many sensors on the ground. These aspects make space-geodesy indispensable tool for geophysics.

1.3 Observation of the earth's gravity field

Gravity measurements in general have played and will keep playing important roles in geosciences because they provide various information on the mass (re-)distribution on and beneath the surface. The gravity field of the earth can be measured by the ground-based and the space-based observations. Here, I explain some basic facts about each type of observations.

1.3.1 Ground-based gravity observation

In ground-based observations, we use absolute and relative gravimeters. The absolute gravimeter measures the gravity acceleration directly from the velocity change of a falling object in vacuum with the accuracy of μGal. On the other hand, typical relative gravimeters use a spring (e.g. Lacoste-Romberg gravimeter) or a magnetic ball floating by superconductivity (Superconducting gravimeter) to measure the change of the gravitational force from the extension of the spring or the electric current to keep the position of the floating ball. Ground-based gravity observations have been performed over a long time perioid [e.g. Iida *et al.*, 1951], and they revealed static mass distribution and mass movements under the ground.

1.3.2 Space-based gravity observation (Satellite gravimetry)

[A] ***Beginning of satellite gravimetry***

Satellite gravimetry started in 1957, when Soviet Union launched the first artificial satellite named "Sputnik". Tracking of this satellite enabled us to estimate low degree/order gravity field of the earth for the first time. By this satellite, the flattening of the earth, which is expressed as the value of the spherical harmonics of J_2 term

(equivalent to $-C_{20}$) was first determined by the observation. After that, the J_3 term was determined by Kozai (1959). This clarified that the gravity field of the earth is asymmetric in north-south, i.e. more mass exists in the Northern Hemisphere and the shape of the equipotential surface of the earth looks like a pear.

[B] ***SLR technique***

In 1970s, the Satellite Laser Ranging (SLR), one of the space geodetic techniques, started to observe the global gravity field of the earth. Satellites for SLR observations have many corner-cube-reflectors (CCR) on their surfaces, and laser pulses transmitted from ground stations bounce back at these reflectors (Figure 1.1). By dividing the two-way travel time of the laser pulses between the stations and the satellites by the speed-of-light, the satellite-station distances are calculated. Small perturbations in the Kepler's orbital elements stem from the deviation of the gravity field from spherical symmetry, and one could recover the global gravity field by analyzing such perturbations. SLR satellites have the long life time because all they need to do is to reflect laser pulses with CCRs.

SLR has provided many important discoveries. Here I quote line 5 – 13 in the page 4 of the 2013 Doctoral Thesis of Dr. Koji Matsuo, Geospatial Information Authority of Japan, submitted to the Graduate School of Science, Hokkaido University (http://www.ep.sci.hokudai.ac.jp/~geodesy/pdf/Matsuo_Dsc_Thesis.pdf).

Yoder et al. (1983) found the decreasing trend of the J_2 term due to the viscous rebound of the solid Earth by Glacial Isostatic Adjustment (GIA) and the Earth's secular spin-down by the friction of external tidal forces (tidal breaking). Nerem et al., (1993) estimated monthly values of the J_2 and J_3 term and detected seasonal changes of them caused by the change in water storage on land by precipitation. Cox and Chao

(2002) found a sudden shift in the J_2 trend from decrease to increase around 1998. The cause of this sudden change still remains unclear even today. Cheng and Tapley (1999) confirmed secular and annual changes in higher degrees of spherical harmonics from J_2 to J_8.

Here, I would like to add that Matsuo *et al.* (2013) estimated the change of the ice mass on Greenland from 1991 to 2011. This was the first result of two-dimensional gravity change observations over Greenland over the period spanning 20 years or more.

Although SLR provides such important information, its spatial resolution is limited to a few thousands of kilometers due to three reasons. At first, most SLR satellites orbit at altitudes of 6000 km or more. Secondly, there are only ~50 SLR ground stations around the world and most of them are only in the northern hemisphere (Figure 1.2). At last, SLR observations are impossible only at a station with fair weather. For these reasons, SLR are inferior to other gravity satellites, such as CHAMP, GRACE, and GOCE, described below in terms of the spatial resolution.

[C] *CHAMP satellite*

In 2000, Challenging Mini-satellite Payload (CHAMP) was launched by GeoForschungsZentrum (GFZ) in Potsdam, German, which flies at the altitude of ~500 km along near-polar orbit and has a Global Positioning System (GPS) receiver in it (Figure 1.3). This technique is called High-Low Satellite-to-Satellite Tracking (H-L SST) because the GPS satellites at ~20,000 km height track and the CHAMP at ~500 km height. This satellite provided the data of the gravity field with better spatial and temporal resolutions than those by SLR.

[D] ***GRACE satellites***

In 2002, the "twin" satellites named Gravity Recovery And Climate Experiment (GRACE) was launched by NASA (National Aeronautics and Space Administration) and DLR (Deutsches Zentrum für Luft- und Raumfahrt). GRACE consists of two satellites (GRACE-A and GRACE-B, about 200 km apart) flying at the altitude of approximately 500 km with the orbital inclination of 89 degrees (near-polar orbit). The gravity irregularities change their along-orbit velocities and they change inter-satellite distance. The GRACE satellite observes the gravity by measuring the distance between the two satellites and their temporal changes (Figure 1.4 and Figure 1.5). The spatial resolution of the GRACE observation is ~100 km for the static global gravity field data, 300–500 km for monthly data, and ~700 km for weekly data. Monthly data are usually used to study gravity changes by earthquakes. Further information and details about the data, analysis processes, examples of contributions to geosciences, and so on are shown in Chapters 2 and 3.

[E] ***GOCE satellite***

In 2009, the Gravity field and steady-state Ocean Circulation Explorer (GOCE) satellite was launched (Figure 1.6) by European Space Agency (ESA) into the near-polar orbit at altitude slightly lower than 300 km. This is the lowest orbit for artificial satellites, and GOCE is consequently the fastest satellite ever launched. This makes the GOCE satellite called "Ferrari of satellites". The GOCE satellite was equipped with a highly-sensitive gravity gradiometer, an equipment to measure spatial derivative of the gravity, as well as a GNSS receiver and 3-axis accelerometers. This Satellite Gravity Gradiometry (SGG) technique provided gravity gradient data with a

high spatial resolution, which led to improve the model of the static global gravity field (Figure 1.7).

The data used to draw the Figure 1.7 was provided by ESA, and can be downloaded through the GOCE Virtual Online Archive from ESA's website *http://earth.esa.int*.

The GOCE satellite is launched to improve the spatial resolution of static gravity fields, and its data are not suitable for time series analyses. The GOCE satellite has already ended its mission in 2013.

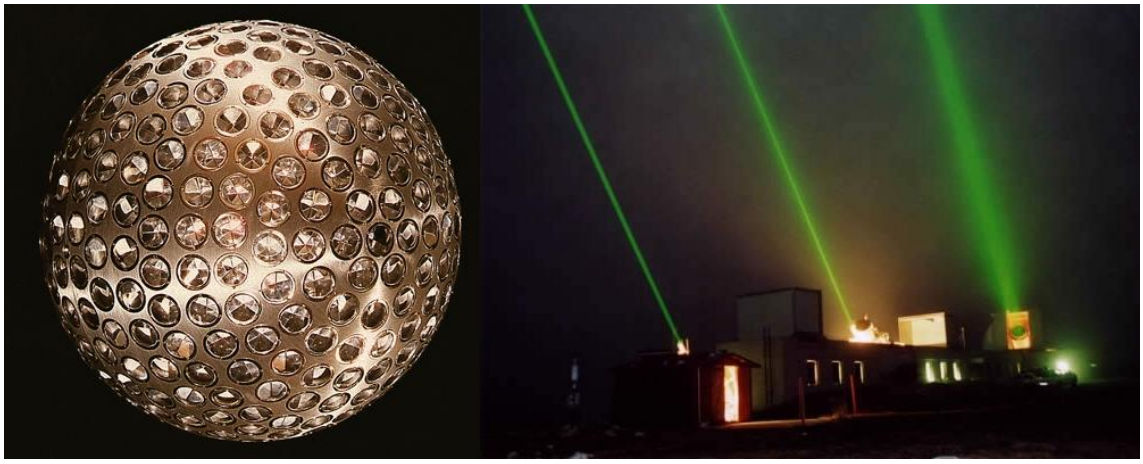

Figure 1.1 An SLR satellite (LAGEOS) and an SLR ground observation station. This picture was downloaded from the website of "l'information grandeur nature" (http://recherche.ign.fr/labos/lareg/page.php?menu=En%20savoir%20plus) on 18 October, 2016.

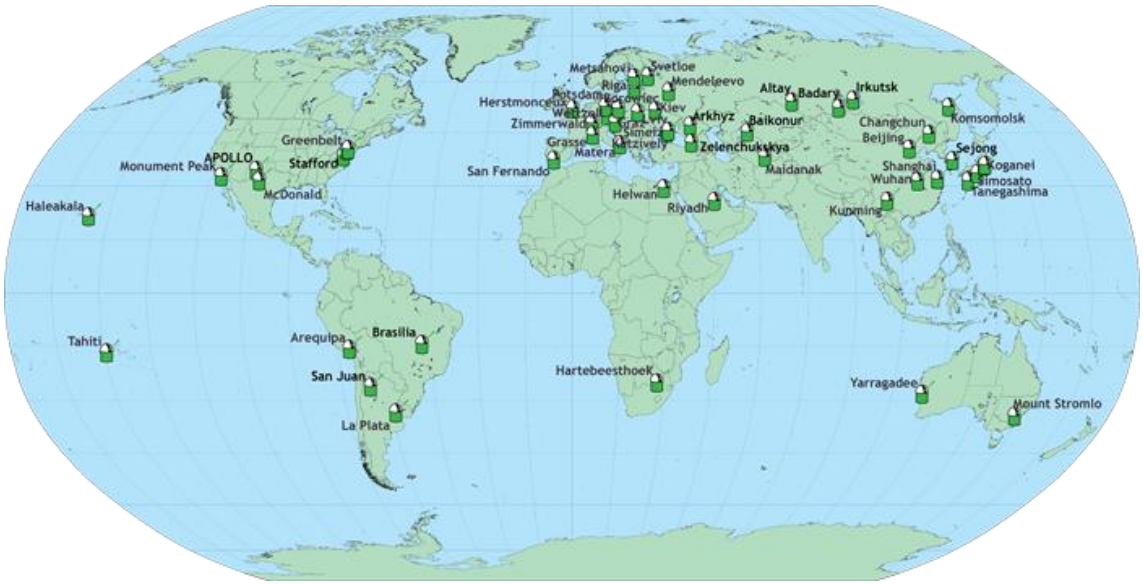

Figure 1.2 The distribution of the worldwide SLR observation stations. Downloaded from the website of ILRS (International Laser Ranging Service) on 18 October, 2016. (http://ilrs.gsfc.nasa.gov/network/stations/)

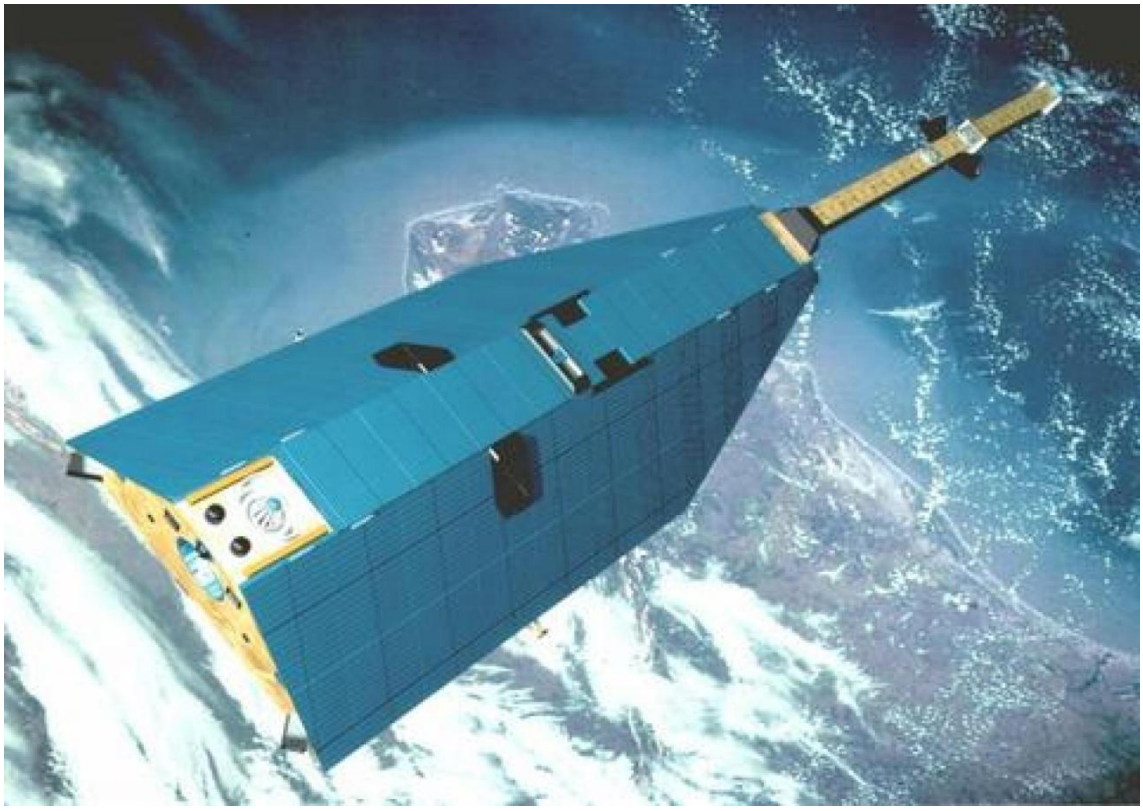

Figure 1.3 An image of the CHAMP satellite downloaded from the NASA website on 18 October, 2016. (https://science.nasa.gov/missions/champ)

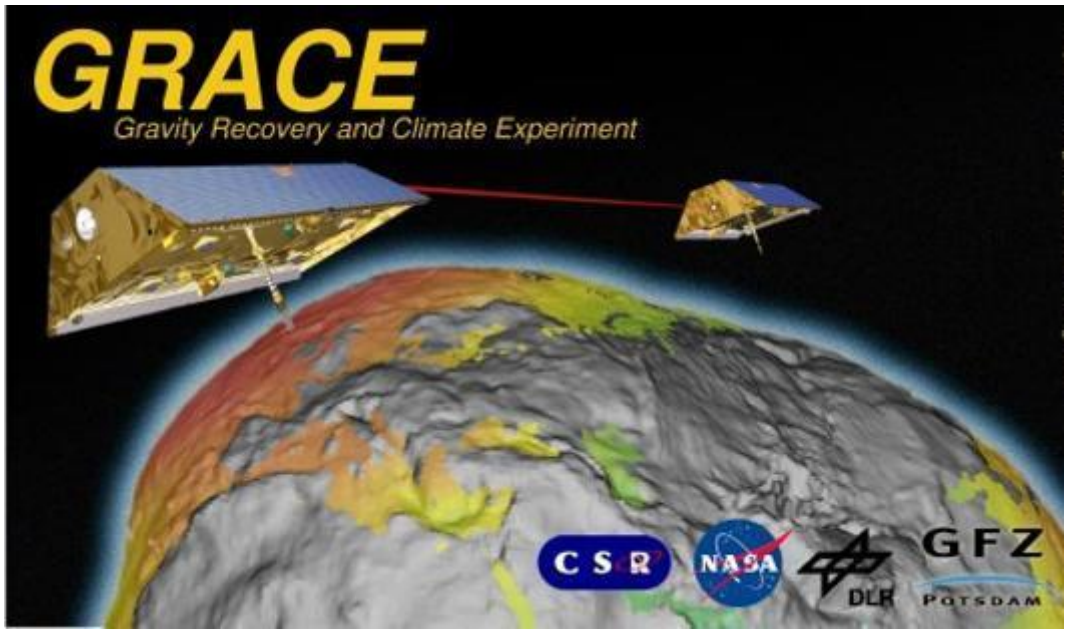

Figure 1.4 An image of the GRACE satellite downloaded from the website of NASA on 18 October, 2016. (http://podaac.jpl.nasa.gov/GRACE)

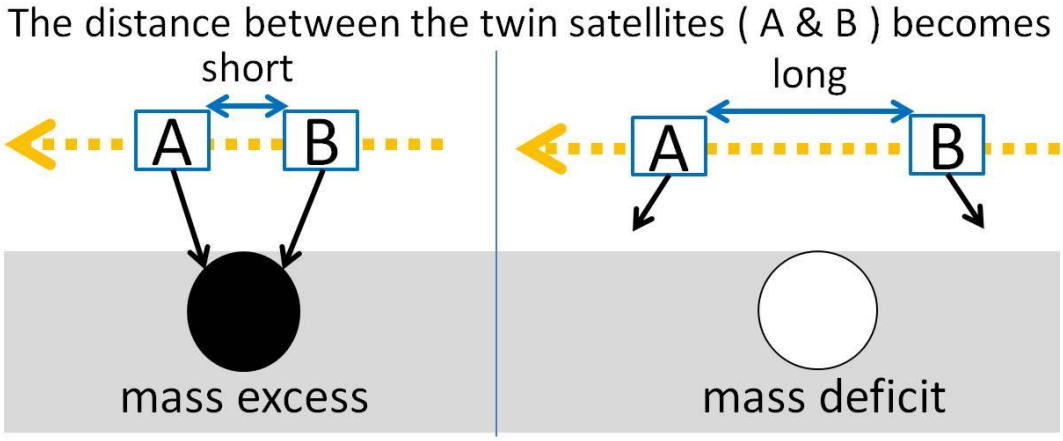

Figure 1.5 The GRACE satellite system is composed of two identical satellites, GRACE-A and GRACE-B. This figure shows how local mass anomalies (excess mass and mass deficit) change the inter-satellite distance. The gravity irregularities make the two satellites in the same orbit accelerate or decelerate with a certain time lag, which is responsible for the distance changes between the two satellites.

Figure 1.6 An image of the GOCE satellite downloaded from the website of Delft University of Technology on 18 October, 2016. (http://www.tudelft.nl/en/current/latest-news/article/detail/lancering-esas-zwaartekrachtmissie-goce/)

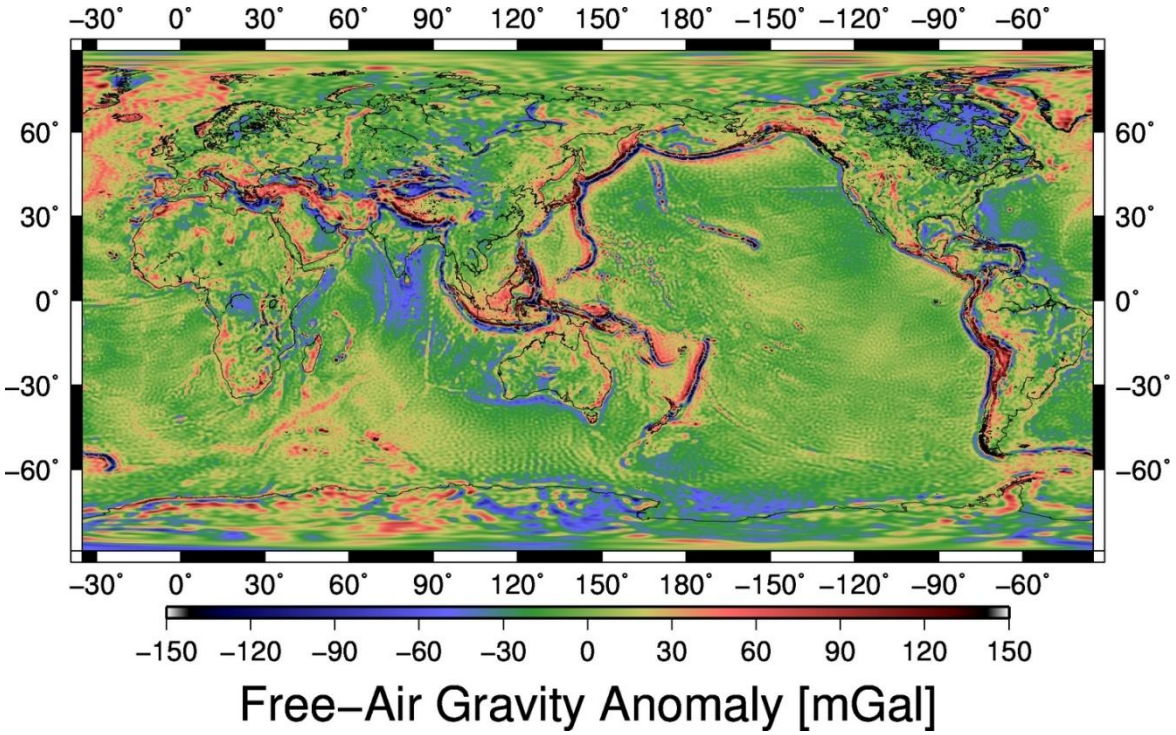

Figure 1.7 A map showing the static global free-air gravity anomaly provided by the GRACE and GOCE satellites. The gravity model is GO_EGM_GOC2 (based on the observation from 1st November 2009 to 21st October 2013) with degrees and orders up to 240, available at GOCE Virtual Online Archive in ESA's website.

1.4 Gravity observations for earthquake researches

In an earthquake, rocks on the two sides of the fault move with respect to one another. It naturally involves movements of mass, and is consequently associated with the change of the local gravity field. However, the research of earthquakes based on two-dimensional mapping of gravity changes became possible only after the launch of the GRACE satellites in 2002.

The most important sensor of earthquakes is seismometers that observe elastic (seismic) waves. The second most important sensor would be GNSS (Global Navigation Satellite System) and SAR (Synthetic Aperture Radar) that observe static displacements

of the ground surface. Gravity observation might be considered the third sensor of earthquakes. Gravimetry observes the mass transportation on and beneath the ground surface (Figure 1.8), and may provide new and unique insights into earthquakes.

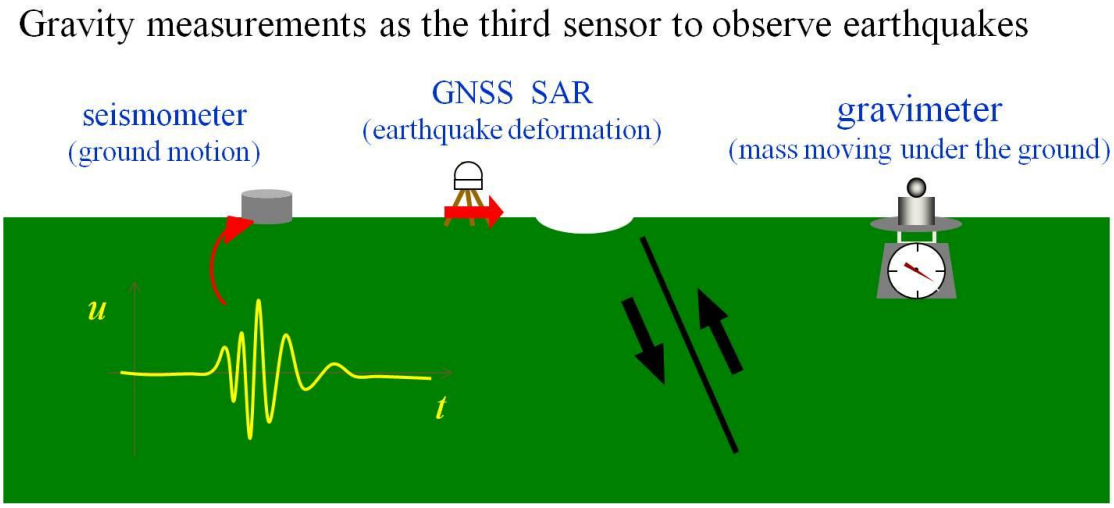

Figure 1.8 A schematic image of three different sensors to observe earthquakes.

Chapter 2
Data and processing

2.1 GRACE data

The GRACE data can be downloaded from http://podaac.jpl.nasa.gov/ (PO.DAAC: Physical Oceanography Distributed Active Archive Center) or http://isdc.gfz-potsdam.de/ (ISDC: Information Systems and Data Center). These data are provided by the three official analysis centers, i.e., Center for Space Research, University of Texas (UTCSR), Jet Propulsion Laboratory, Caltech (JPL), and GFZ Potsdam, Germany. UTCSR and JPL are in USA. These three institutions analyze the GRACE data taking somewhat different approaches, so the data sets differ slightly from center to center. In addition, many other unofficial institutions provide data analyzed with their own data analysis methods. They are available at http://icgem.gfz-potsdam.de/ICGEM/.

There are three levels of the GRACE data available to users: Level-1B, Level-2, and Level-3. Level-1B data consist of the ranges (distances) between the twin satellites with their changing rates and accelerations (relative velocities and accelerations). It demands expertise in the technical details to use such Level-1B data sets. Level-2 data

are provided as monthly sets of spherical harmonic (Stokes') coefficients. To use them, we need only certain mathematical knowledge of the spherical harmonics. Analysis centers routinely improve the data processing methods by introducing better geophysical models of atmosphere, ocean, and so on, to produce Level-2 data. Today RL05 (Release-05) data are the latest. Level-3 data are composed of spatial domain gravity data. These data have already been filtered to reduce noises in several ways. The Level-3 data are the most user-friendly, and we do not need spatial technical or mathematical knowledge to analyze them. However, we need to be aware that the filters may have reduced useful information as well as noises.

Level-2 data are composed of spherical harmonic coefficients (Stokes' coefficients), which can be converted to various components of the static gravity field, i.e., vertical components $G_r(h,\theta,\varphi)$, northward components $G_\theta(h,\theta,\varphi)$, and upward spatial derivative of the downward component $G_{rr}(h,\theta,\varphi)$, by using the equations (2.1), (2.2), and (2.3), respectively [Kaula, 1966; Heiskanen and Moritz, 1967; Wang L. *et al.*, 2012a].

$$G_r(h,\theta,\varphi) = -\frac{GM}{R^2}\sum_{n=2}^{nmax}(n+1)\left(\frac{R}{R+h}\right)^{n+2}\sum_{m=0}^{n}\left(C_{nm}\cos m\varphi + S_{nm}\sin m\varphi\right)P_n^m(\sin\theta) \qquad (2.1)$$

$$G_\theta(h,\theta,\varphi) = -\frac{GM}{R}\sum_{n=2}^{nmax}\left(\frac{R}{R+h}\right)^{n+1}\sum_{m=0}^{n}\left(C_{nm}\cos m\varphi + S_{nm}\sin m\varphi\right)\frac{dP_n^m(\sin\theta)}{d\theta} \qquad (2.2)$$

$$G_{rr}(h,\theta,\varphi) = \frac{GM}{R^3}\sum_{n=2}^{nmax}(n+1)(n+2)\left(\frac{R}{R+h}\right)^{n+3}\sum_{m=0}^{n}\left(C_{nm}\cos m\varphi + S_{nm}\sin m\varphi\right)P_n^m(\sin\theta) \qquad (2.3)$$

where θ and φ are colatitudes and longitudes, respectively, *G* is the universal gravity

constant, M is the mass of the earth, R is the equatorial radius, h is the height of the observation point from the earth's surface, $P_n^m(cos\,\theta)$ is the n-th degree and m-th order fully-normalized associated Legendre function. The h should be zero when we analyze the gravity on the surface of the earth. The terms of C_{10}, C_{11}, and S_{11} reflects the geocenter position. It may move seasonally and secularly relative to the figure center of the earth due to, for example, water redistribution between the Southern and the Northern Hemispheres. However, the gravity field is always expressed in geocentric coordinates, so these terms should be fixed to zero for the satellite gravimetry data analysis. An example of the static gravity field of the earth is shown in the Figure 2.1. (In this thesis, unless noted otherwise, RL05 Level-2 data with degrees and orders up to 60 analyzed by UTCSR are used, and the downward components of the gravity field are discussed).

In addition to the conventional expression using spherical harmonics, the mascon solutions ("mascon" is a shortened word of "mass concentration") are also available. These solutions show mass distributions calculated with an assumption that gravity anomalies come from mass on the earth's surface [Chao, 2016]. This approach is inappropriate to study gravity changes related to earthquakes because such gravity changes may reflect mass redistributions at depth (details are given in the Chapters 4 and 5).

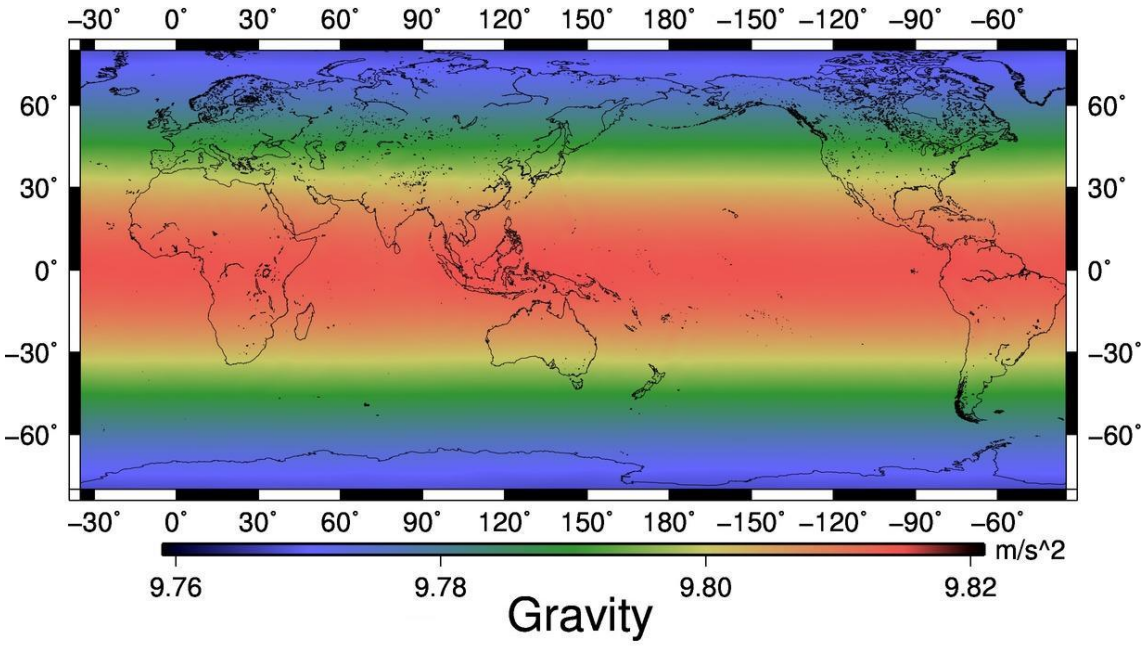

Figure 2.1 The map of the global static downward gravity field in August 2015 calculated from Level-2 GRACE data composed of Stokes' coefficients with degrees and orders complete to 60. Degree 2 components are predominant.

This figure shows the mean of the gravity is ~9.8 m/s^2 and the gravity in low latitude region is stronger than those at higher latitudes. It is well known that the gravity field is weaker in the low latitude region because of the centrifugal force due to the spin of the earth weakens the gravity field. This inconsistency comes from the fact that the gravity fields measured by satellites from space do not include centrifugal forces and excess gravitational pull by the equatorial bulge emerges.

The contribution of the C_{20} term predominates in the global gravity field. In Figure 2.2, I show only the contributions of coefficients other than C_{20}.

Such a long-wavelength component as C_{20} can be measured more accurately by high-altitude SLR satellites rather than low-altitude satellites like GRACE. Hence, C_{20} terms in the GRACE gravity models are usually replaced with those measured by SLR when we discuss time-variable gravity fields.

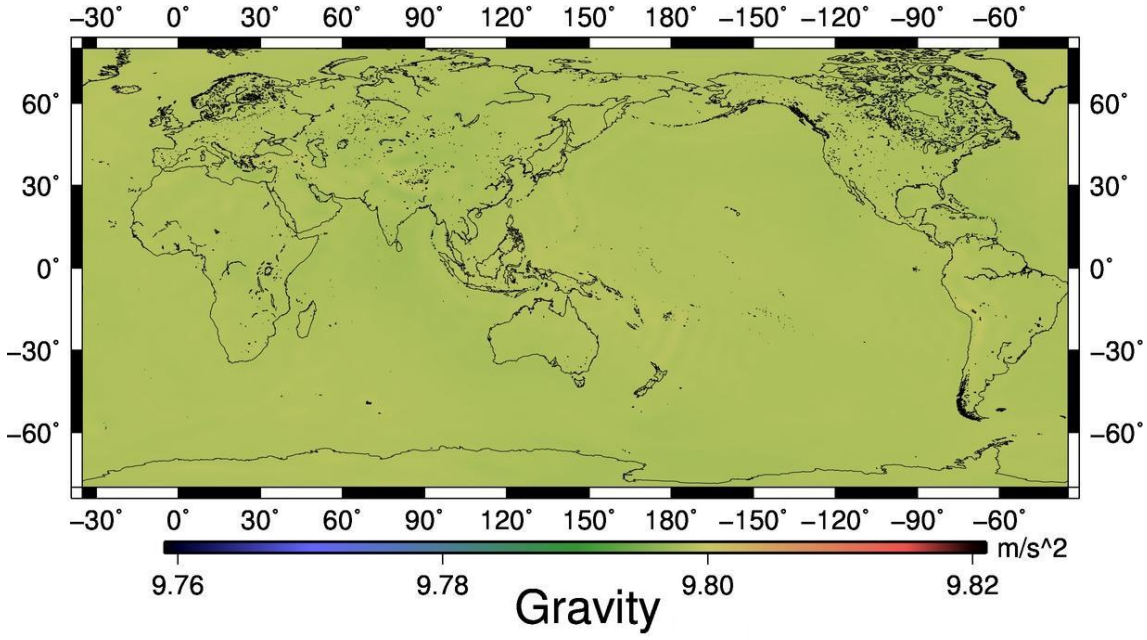

Figure 2.2 The same as Figure 2.1 but the C_{20} component is removed.

Figure 2.2 shows that the gravity anomalies are so small that the gravity acceleration is almost uniformly 9.8 m/s^2 throughout the surface when the contributions of the equatorial bulge (C_{20} component) are removed. In order to highlight the static gravity anomalies, the unit (m/s^2) has to be changed into mGal (1 Gal = 1 cm/s^2) and the C_{00} term has been set to zero (C_{00} provides the mean value of the global gravity field). The anomalies are shown in Figures 2.3 and 2.4.

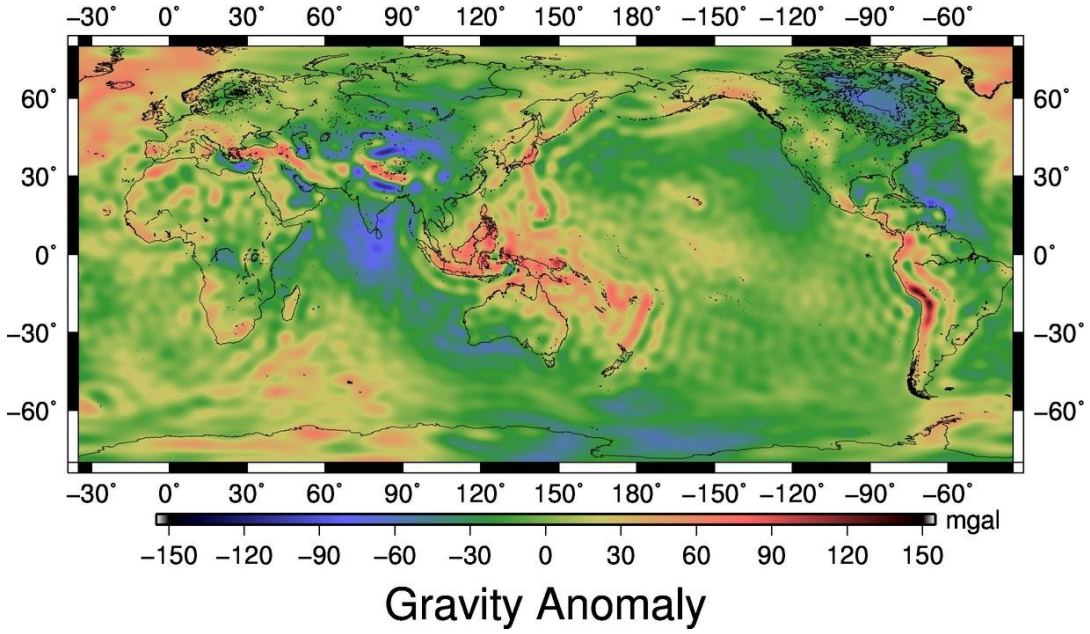

Figure 2.3 The global gravity anomaly map in August 2015 calculated from Level-2 GRACE data. The C_{20} and C_{00} components are removed.

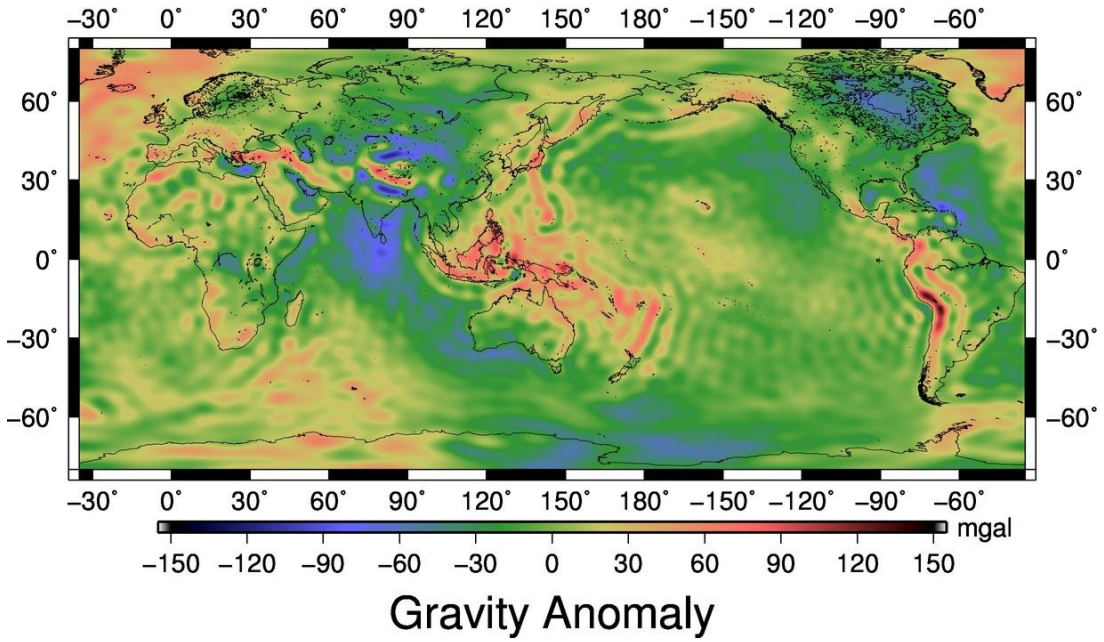

Figure 2.4 The same as Figure 2.3 except the epoch (February 2016).

Figures 2.3 and 2.4 show the global gravity fields in August 2015 and in February 2016, respectively. They represent different time epochs but they look alike because the temporal changes of the gravity fields are very small compared to the static spatial differences. In order to study time-variable gravity, the unit has to be changed to μGal. The difference of the gravity fields between the two epochs is shown in Figure 2.5.

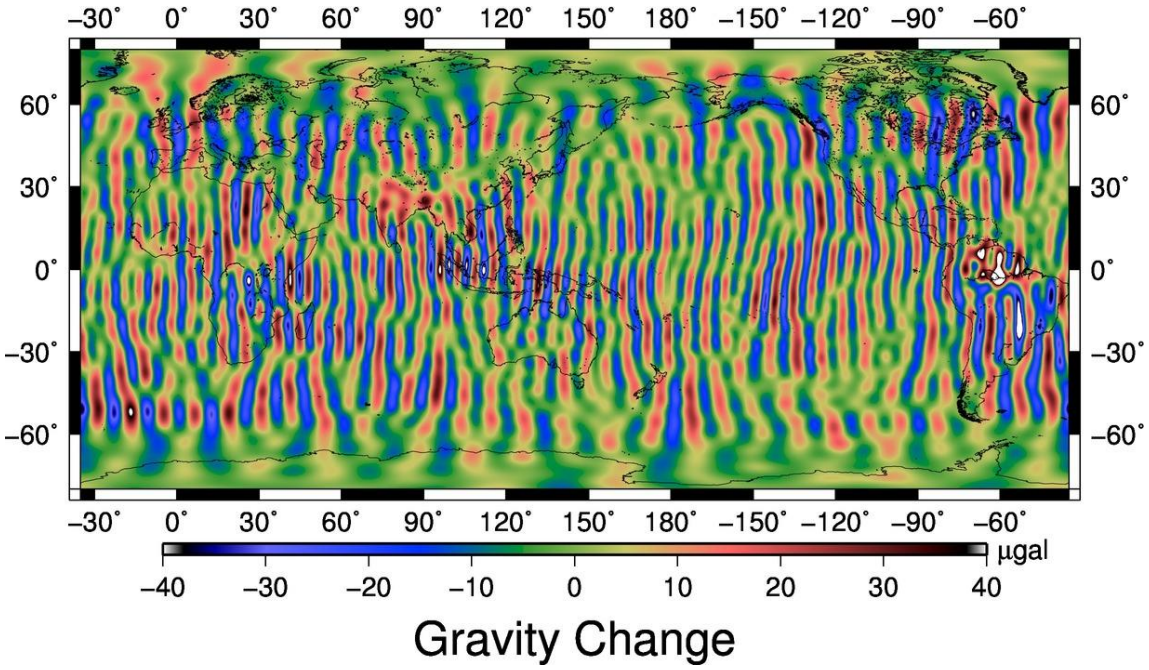

Figure 2.5 The difference of the gravity fields in August 2015 from those in February 2016.

Figure 2.5 shows strong longitudinal (north-south) stripes. These stripes stem from the north-south movements of the GRACE satellites. The GRACE satellites employ a near-polar circular orbit, taking ~90 minutes per one cycle (they experience

about 550 revolutions every month), so spatial gravity changes in north-south direction are measured continuously by the GRACE satellites. However, those in the east-west direction are measured at different times; for example, the difference in gravity between (a (E), b (N)) and (a (E), b+1 (N)) is measured using data from one continuous orbit, but those at (a, b) and (a+1, b) are measured in different arcs of polar orbits. Thus, the spatial gravity changes in east-west direction are calculated separately from different arcs of their orbits. Hence, they include more systematic errors in the direction orthogonal to the orbit (east) than in parallel with the orbit (north). This anisotropic structure of systematic noises appears as the longitudinal stripes.

Moreover, the GRACE data include other random noises in short-wavelength components because of its limited spatial resolution of ~300 km coming from its orbital altitude of ~500 km. These problems suggest that certain means (e.g. applying spatial filters) are necessary to analyze time variable gravity with the GRACE data.

2.2 Methods to reduce noises

There are several methods to reduce noises [*Munekane*, 2013]. In this thesis, I used four of such methods to study gravity changes related to earthquakes.

2.2.1 Two filters to reduce noises of the GRACE data

The stripe noises and the short-wavelength noises are reduced to a large extent by using two filters, i.e., the fan filter and the de-striping filter. Details of the two filters are described in following paragraphs, and their demonstrations are shown in Figure 2.6.

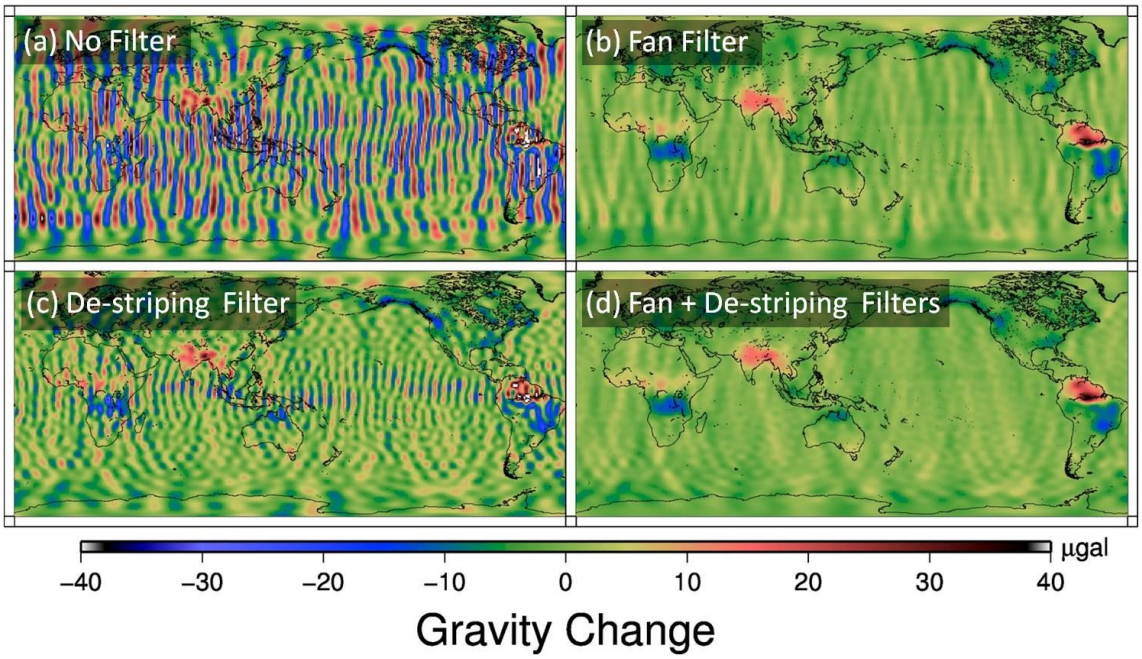

Figure 2.6 The demonstration of the two filters widely used in the GRACE data processing. The four panels show: (a) no filters (same as Figure 2.5), (b) only the fan filter (anisotropic Gaussian filter, averaging radius is 250 km), (c) only the de-striping filter (cubic function is fitted on degrees and orders of 15 and more), (d) both the fan filter and the de-striping filter.

[A] ***Fan filter***

The best filter for the smoothing of the spatial distribution of gravity changes is the two-dimensional spatial Gaussian filter [*Wahr et al.*, 1998], and its anisotropic version "fan filter" [*Zhang et al.*, 2009]. The definition of this filter and the way to apply it to the coefficients are shown with equations (2.4)-(2.8). Here, the *h*, representing the height of the observation point in the equation (2.1), is set at zero.

$$\Delta G(\theta,\varphi) = -\frac{GM}{R^2}\sum_{n=2}^{nmax}(n-1)W_n\sum_{m=0}^{n}W_m(\Delta C_{nm}\cos m\varphi + \Delta S_{nm}\sin m\varphi)P_n^m(\sin\theta) \quad (2.4)$$

$$W_0 = 1 \quad (2.5)$$

$$W_1 = \frac{1 + e^{-2b}}{1 - e^{-2b}} - \frac{1}{b} \quad (2.6)$$

$$W_{n+2} = -\frac{2n + 1}{b} W_{n+1} + W_n \quad (2.7)$$

$$b = \frac{\ln(2)}{1 - \cos\frac{r}{R}} \quad (2.8)$$

where W_n is the weighting function with Gaussian distribution for coefficients with degree n, and r is the averaging radius. Weights, with different values of r, are shown in Figure 2.7. This filter gives smaller weights to coefficients of higher degrees and orders, which reduces the short-wavelength noises. We apply the Gaussian filter to the order (m) as well as the degree (n) in order to reduce short-wavelength noises more efficiently. This anisotropic filter is called Fan filter. The contribution of this filter is shown in Figure 2.6 (a) and (b).

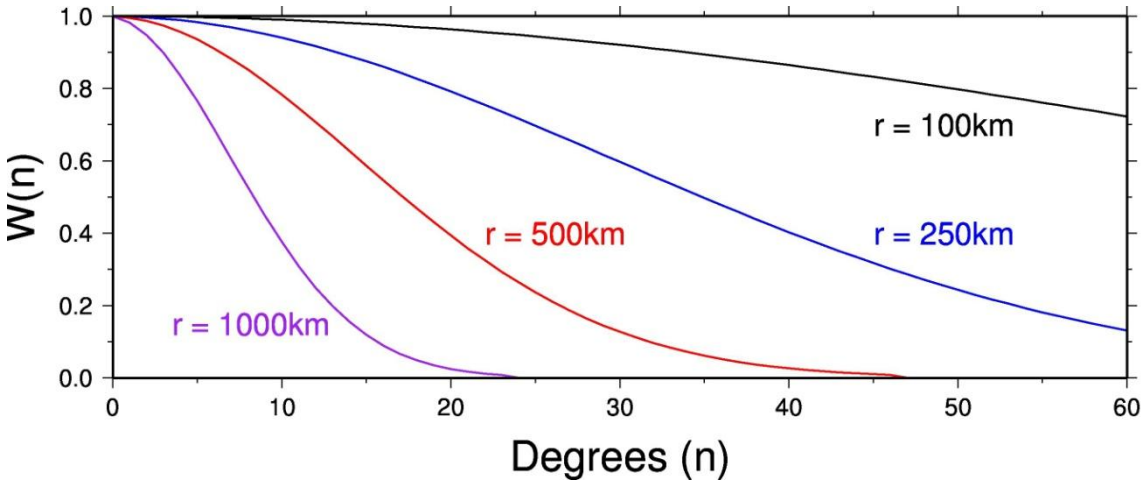

Figure 2.7 The values of W_n as a function of degree n for the different values of r, i.e., 100 km, 250 km, 500 km, and 1000 km. The weight becomes smaller for larger degrees and for larger r.

[B] ***De-striping filter***

The fan filter reduces shortwave noises, but stripe noises still remain in Figure 2.6 (b). Hence, another filter ("de-striping filter") is necessary to reduce such longitudinal stripes as proposed by *Sweson and Wahr* [2006]. They found the stripes stem from the highly systematic behavior of the Stokes' coefficients in the GRACE data. The Stokes' coefficients of ΔC_{n25} (C_{n25} in August 2015 – C_{n25} in February 2016), are shown in Figure 2.8 as an example. There the red points (the evens of coefficients) are always bigger than blue points (odds) except for the degrees 25 and 27, and the black line connecting them goes zigzag strongly. *Swenson and Wahr* [2006] considered that this is responsible for the stripes, and proposed to suppress them by getting rid of such systematic behaviors. For this purpose, two polynomial functions were fitted with the least-square method to evens and odds of coefficients separately, and residuals from the fitted polynomials were taken as the new "de-striped" coefficients. Another example is given in Figure 2.9, where the polynomial of degree 7 is used. In this case, the values of de-striped coefficients become almost zero. Although the stripes are almost removed completely, this also means that valuable information might be removed together with stripe noises. Thus, the filter has to be used carefully.

Figure 2.6 (c) shows the gravity change calculated using the "de-striped" coefficients. This de-striping filter is called as P3M15, which means that polynomials of degree 3 (cubic function) were fitted to the coefficients of degrees and orders 15 or more. Figure 2.6 (d), the result after applying both of the two filters, demonstrates that both of the fan and de-striping filters need to be used to reduce noises in the downward gravity components from the GRACE data.

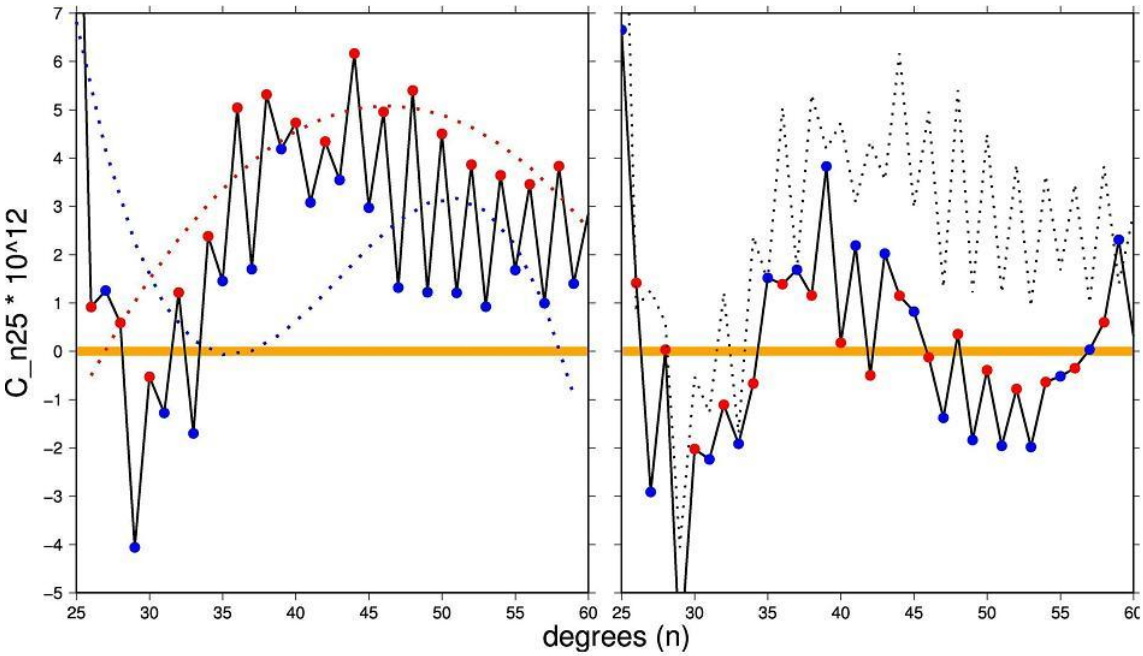

Figure 2.8 A conceptual explanation of the de-striping filter. (left) The solid black line indicates the Stokes' coefficients of degrees 25-60 and of order 25, i.e., ΔC_{n25} (C_{n25} in August 2015 – C_{n25} in February 2016) as a function of degree n. The red and blue points denote the values of coefficients with even and odd n, respectively. The red and blue broken curves are polynomials with the degree 3 fitted to the two groups of the data. (right) The broken black line is the same as the solid black line in the left figure. The solid black line indicates the "de-striped" Stokes' coefficients, whose values are shown as the red and blue points. The red/blue points are differences between the red/blue points and the red/blue curves in the left figure. The orange horizontal straight line means zero.

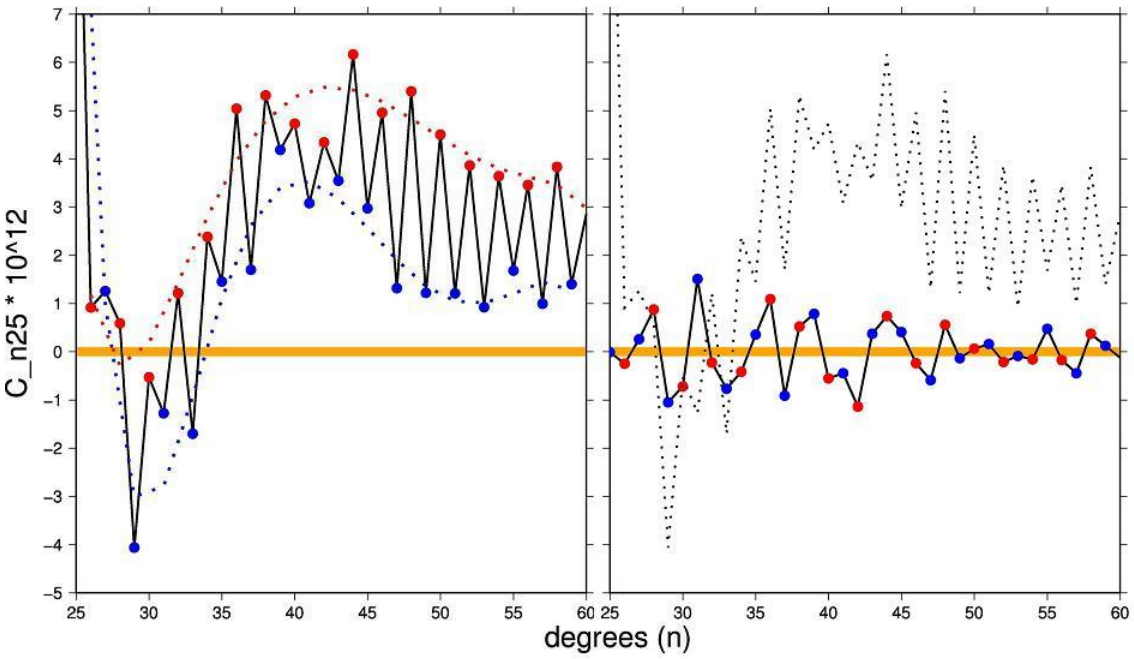

Figure 2.9 The same figure as Figure 2.8, except that polynomials with the degree 7 are used.

2.2.2 Northward components of the GRACE data

To weaken the stripes, northward gravity components from the GRACE data are useful. The northward components are free from the stripes because the GRACE satellites move in the north-south direction. These components are calculated by differentiating the gravity potential with respect to the latitude [*Wang et al.*, 2012a]. The differences of the northward gravity components in August 2015 from those in February 2016 are shown in Figure 2.10. We still need to apply the fan filter, but the de-striping filter is not necessary.

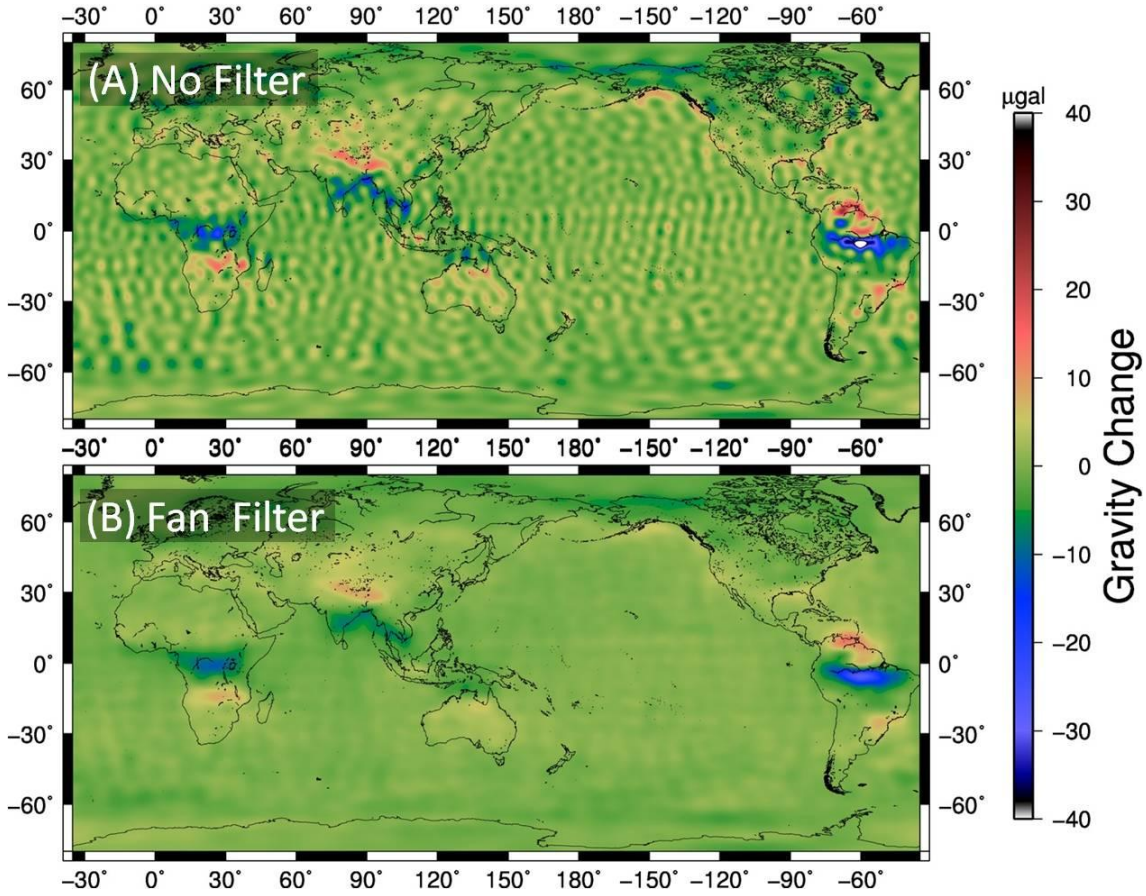

Figure 2.10 The map showing the deviation of the northward gravity components in August 2015 relative to those in February 2016. (A) No filters are applied. Strong north-south stripes do not appear but shortwave noises are present. (B) Only fan filter (averaging radius = 250 km) is applied to reduce short-wavelength noises.

2.2.3 The Slepian functions

The third method to analyze downward components without relying to noise-reduction filters is to localize the GRACE data by mathematical techniques. A localization technique for signals of gravity changes by earthquakes is achieved by using the "Slepian functions" [*Simons et al.*, 2006], a set of functions for wavelet analyses of characteristic spatial distributions of data on a sphere. In particular, local

components of gravity changes are extracted by the principal component analysis with several basis functions consisting of simple spatial patterns. The signals of coseismic gravity changes are often extracted in this way because of their simple spatial patterns [e.g. *Han et al.*, 2013; 2015].

2.2.4 Stochastic filter

In order to remove the noises, *Wang et al.* [2016] presented "Stochastic filter", which removes the striping noises by using a covariance matrices on the assumption of the randomness of the appearance of the stripes. This filter is based on statistical principles, and will become one of major numerical techniques to analyze the GRACE data in the future. However, any studies based on this method are not introduced in this thesis, and its details are mentioned here.

2.3 Land water models

As "C" of "GRACE" indicates "Climate", study of climate signals, especially those from land hydrology, was one of the most important targets of the GRACE mission. However, these signals are treated as noises for the study of signals related to earthquakes. Contributions of land water such as ice, snow pack, canopy water, groundwater, or soil moisture have to be treated carefully (details are provided in Chapter 3). To correct them, we often use models such as Global Land Data Assimilation System (GLDAS) [*Rodell et al.*, 2004] or Water-Global Assessment Prognois (WaterGAP) [*Döll et al.*, 1999; *Aus der Beek et al.*, 2011]. They are forced by many analysis results and observation data. However, because all of them are based on meteorological observations, these models often include significant errors especially

where insufficient amount of data are available to make the model. Thus, "land hydrology correction" with these models often results in increasing the hydrological noises, and these models have to be used carefully.

In this study, I use GLDAS-NOAH model. This model provides data of the land water (soil moisture, canopy, and snow). According to GRACE Tellus (https://grace.jpl.nasa.gov/data/get-data/land-water-content/) in a website of NASA, the total water content by this model can directly be compared to those by GEACE and they are well matched to a certain extent. However, this does not include groundwater, rivers, lakes, and so on. Also, ice sheet of Antarctica and Greenland is not contained because hydrological models and meteorological data are not available.

2.4 Time series analysis of the GRACE data

Time series of the GRACE monthly gravity data are often modeled as follows.

$$G(t) = a_1 + a_2 t + \alpha \sin(2\pi t + \theta_1) + \beta \sin(4\pi t + \theta_2) + f(t) \qquad (2.9)$$

where a_1, a_2, α, β, θ_1, and θ_2 are constants, the third and forth terms are annual and semi-annual seasonal changes, respectively, and $f(t)$ is used for transient components when necessary.

The third and fourth terms can be reformed by a trigonometric addition formula as following.

$$\begin{aligned} \alpha \sin(2\pi t + \theta_1) &= \alpha \cos\theta_1 \sin(2\pi t) + \alpha \sin\theta_1 \cos(2\pi t) \\ &= a_3 \sin(2\pi t) + a_4 \cos(2\pi t) \end{aligned} \qquad (2.10)$$

$$\beta \sin(4\pi t + \theta_2) = \beta \cos\theta_2 \sin(4\pi t) + \beta \sin\theta_2 \cos(4\pi t)$$
$$= a_5 \sin(4\pi t) + a_6 \cos(4\pi t) \quad (2.11)$$

where $a_3 = \alpha\cos\theta_1$, $a_4 = \alpha\sin\theta_1$, $a_5 = \beta\cos\theta_2$, and $a_6 = \beta\sin\theta_2$.

Pre-, co-, and post-seismic terms have to be separated to research gravity changes by earthquakes. Thus, $f(t)$ in equation (2.7) should be:

$$f(t) = H(t - t_{eq}) \times \{C + P(t - t_{eq})\} \quad (2.12)$$
$$H(t - t_{eq}) = \begin{cases} 0, & t < t_{eq} \\ 1, & t \geq t_{eq} \end{cases}$$

where H is the Heaviside step function, t_{eq} is the time of the occurrence of a target earthquake, C is the constant term representing the coseismic gravity steps, and $P(t - t_{eq})$ is a function representing postseismic gravity changes. Coseismic gravity changes observed by the GRACE satellites appear as steps, whereas postseismic gravity changes show slowly decaying changes, so C and P have to be a constant and a function of time from the target earthquake, respectively.

Putting (2.10) – (2.12) into (2.9) makes (2.13).

$$G(t) = a_1 + a_2 t + a_3 \sin(2\pi t) + a_4 \cos(2\pi t) + a_5 \sin(4\pi t) + a_6 \cos(4\pi t) + H(t - t_{eq}) \times \{C + P(t - t_{eq})\} \quad (2.13)$$

The first line of (2.13) represents the offset and the secular trend, the second line represents seasonal changes, and the third line represents co- and post-seismic changes.

Time series of gravity changes associated with earthquakes are analyzed by fitting the function (2.13) to the GRACE data with the least-squares method. For example, coseismic gravity changes can be mapped by plotting values of estimated at each grid point in this way.

We often perform time series analysis of the coefficients of functions used to express gravity changes, such as the Slepian functions and the spherical harmonics using similar models for temporal changes [e.g. *Han et al.*, 2015].

Chapter 3
Non-earthquake gravity changes

The GRACE satellites observe very small gravity changes. Gravity changes of ~1 μGal can be measured as described in Chapter 2. This means that the GRACE data are useful to study various kinds of geophysical phenomena accompanying mass redistribution. We also need to have enough background knowledges on such phenomena in order to distinguish earthquake-origin gravity changes from them. There are four main phenomena whose gravity changes have amplitudes comparable to those of earthquakes. They include (1) changes of the soil moisture [e.g. *Tapley et al.*, 2004], and (2) changes in groundwater, often caused by human activities such as irrigation [e.g. *Rodell et al.*, 2009]. Other important factors are, (3) long-term ice mass changes by climate changes [e.g. *Jacob et al.*, 2012], and (4) glacial isostatic adjustment (GIA), also called post glacial rebound [e.g. *Tamisiea et al.*, 2007].

Changes of the soil moisture are the main factor responsible for the seasonal gravity changes (Figures 3.1 - 3.3), and short-term changes, including seasonal variations, appear more in the time series of the GRACE data than those in the GNSS site coordinate data. Tracking these changes provides valuable information on global water budget. They stem from water stored in the ground, so they emerge clearly around

tropical monsoon climate area and subarctic humid climate area. They are, however, unclear around desert climate area and on the ocean.

Long-term ice mass changes, due possibly to the recent global warming, can be seen around Greenland, the Antarctic Peninsula, Southern Alaska, Patagonia, and Asian High Mountain region (Figures 3.4 - 3.6). The amount of ice mass loss per year can be inferred from the GRACE time-variable gravity data [e.g. *Matsuo and Heki*, 2014; *Harig and Simons*, 2012; 2015], but it is difficult to distinguish their signals from those of groundwater depletion in the Northern India [e.g. *Rodell et al.*, 2009] because of the insufficient spatial resolution of the GRACE data. In addition, the ice becomes water getting into the ocean, slightly increasing the gravity over the world-wide oceanic area.

Certain high-latitude regions have been uplifting since ice sheets disappeared at the end of the last glacial age. This phenomenon is called glacial isostatic adjustment (GIA) or postglacial rebound (PGR). GIA increases the gravity because the GRACE satellites feel the ground mass increasing beneath them (Figure 3.4). This appears as the secular increase of gravity. The maximum rates of the uplift around the north-east Canada and Scandinavia exceed 1 cm/year according to recent GNSS observations [*Milne et al.*, 2012].

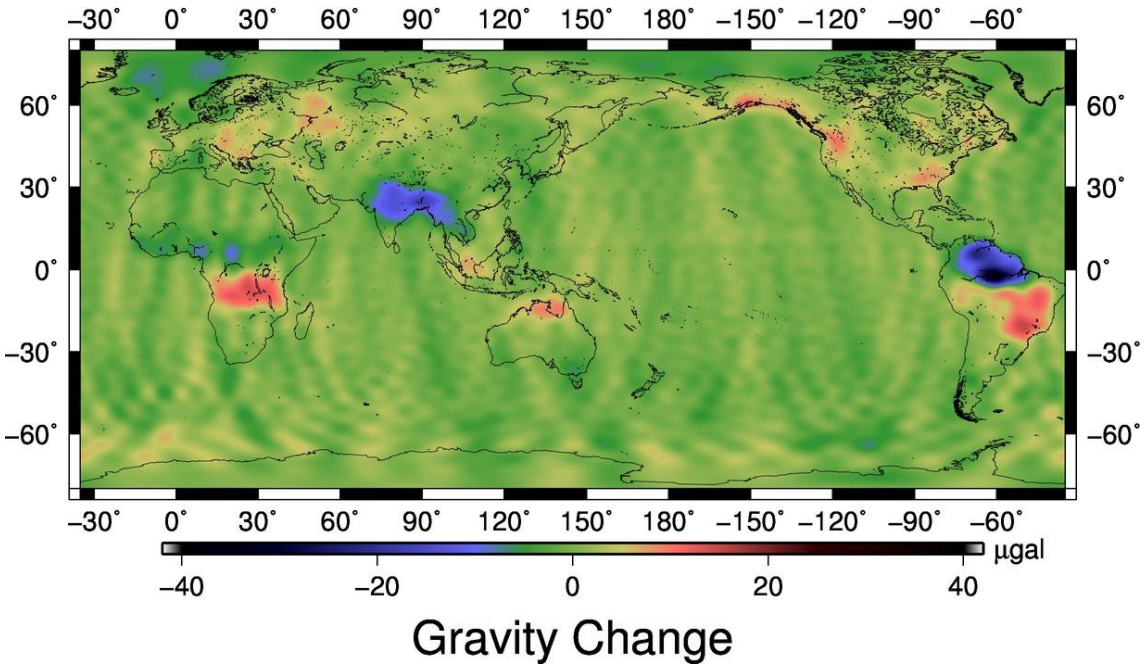

Figure 3.1 The gravity changes from August 2015 to February 2016 around the world (Figure 2.6 showed the gravity distribution in August 2015 relative to February 2016). The gravity changes mainly come from seasonal variabilities. A clear gravity contrast appears around the Amazon River, i.e., dry season on the north side and rainy season on the south side. The larger gravity in rainy seasons reflects water stored in the ground until dry seasons. Similar signals are seen in equatorial Africa, southern Asia, and northern Australia. The positive signals along the coastline of Alaska and Canada perhaps reflects the snow mass in winter.

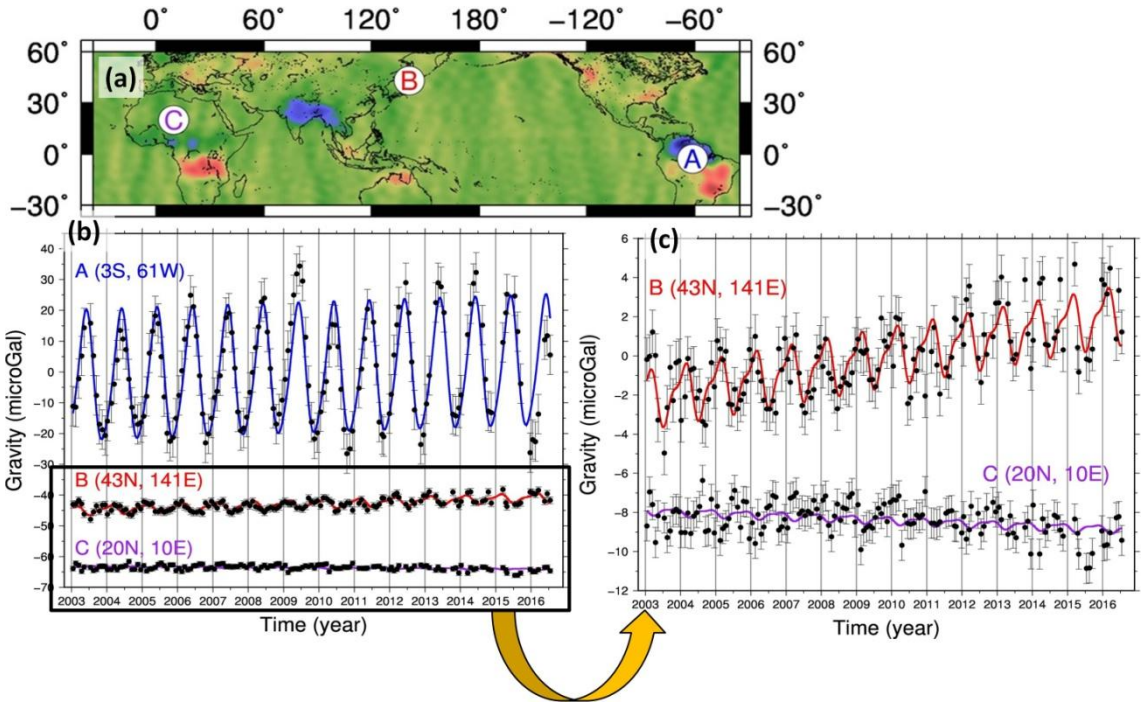

Figure 3.2 (a) The same as Figure 3.1 apart from symbols A, B, and C showing points where gravity time series are shown in (b) and (c). (b, c) The time series of gravity at A, B, and C in (a). A (3S, 61W), located at the north side of the Amazon Basin, shows the strongest seasonal changes, and B (43N, 141E), in Hokkaido, Japan, shows mild seasonal changes. C (20N, 10E), in the Sahara desert, shows little seasonal changes. Model curves are derived to fit the GRACE data (black dots) with the least-squares method using a function composed of terms such as constant offset, secular trend, and annual and semiannual changes. The error bars are scaled using the post-fit residuals between the GRACE data and the model curves. These examples demonstrate that land hydrology governs the seasonal gravity changes.

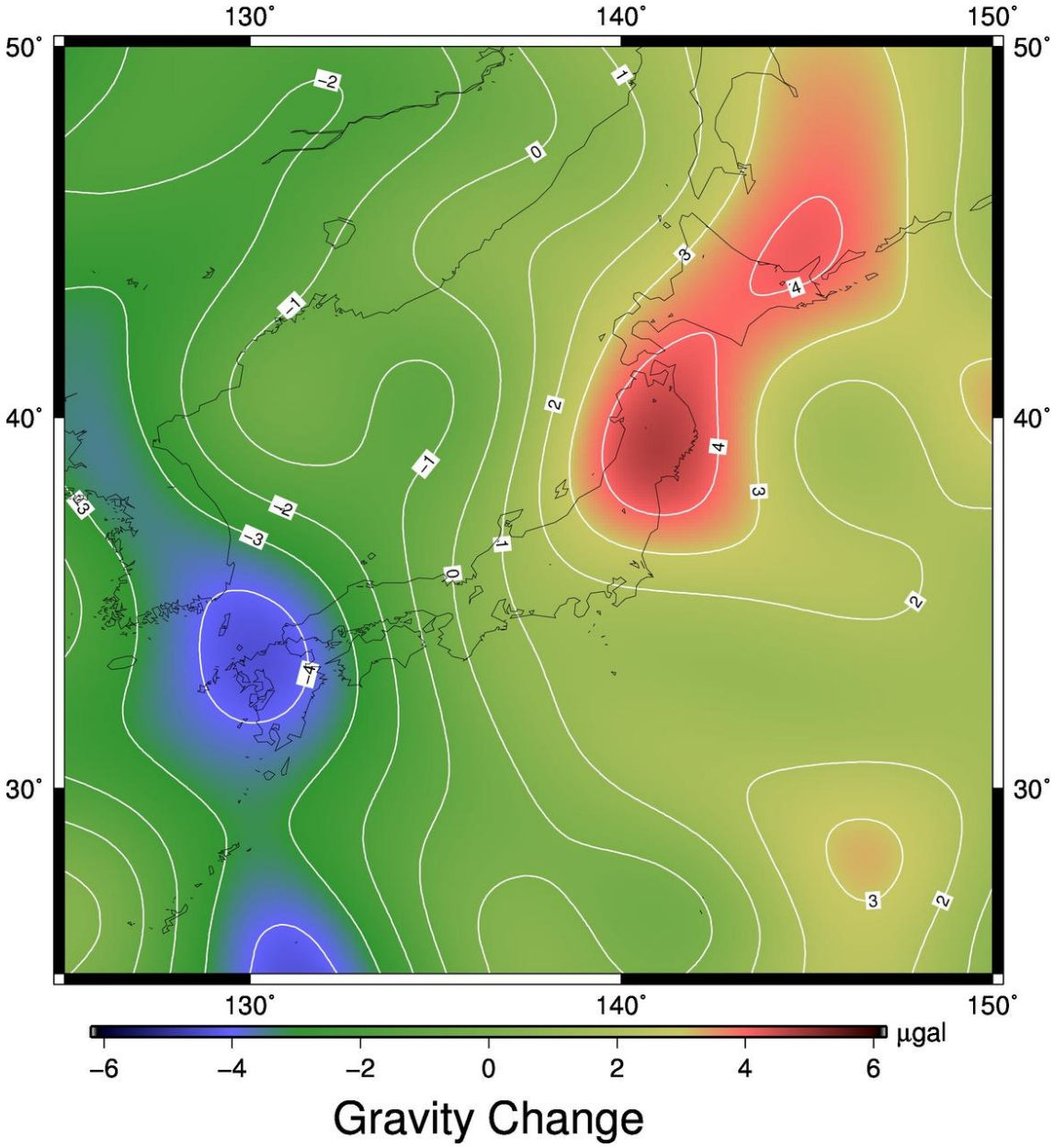

Figure 3.3 The gravity changes from August 2015 to February 2016 around the Japanese Islands. Please note that the color scale is different from Figure 3.1. The contour interval is 1 µGal. The winter snow let the gravity increase around Tohoku and Hokkaido area, and small precipitation may have decreased the soil moisture and gravity around Kyushu.

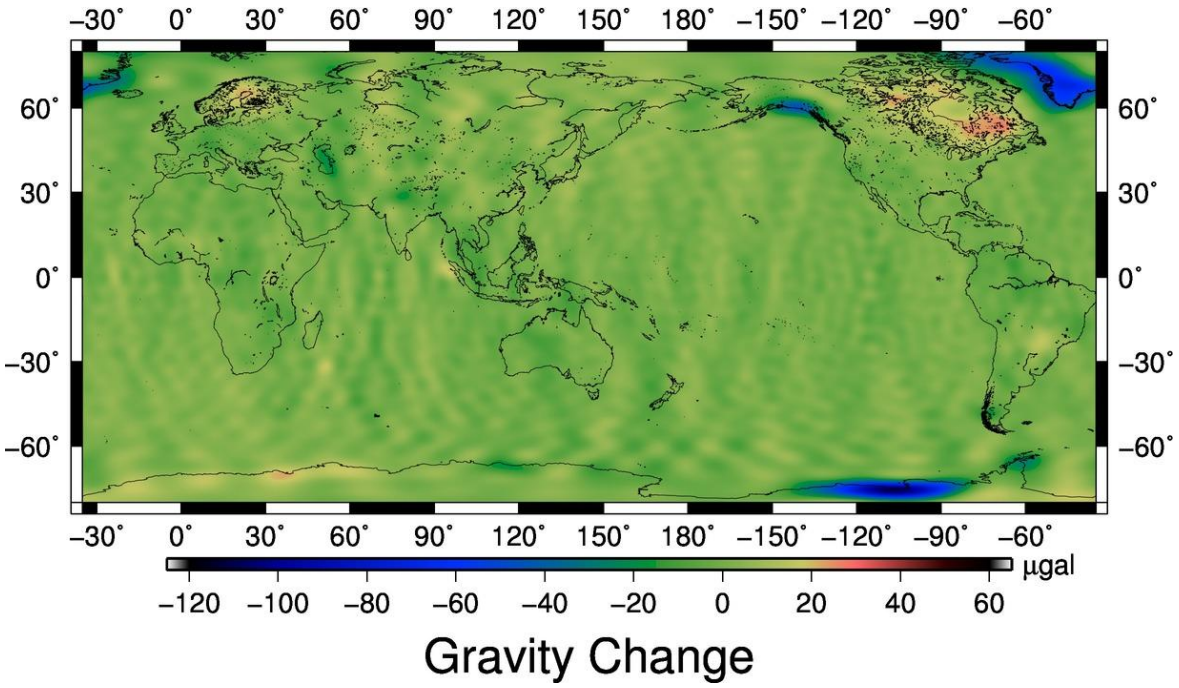

Figure 3.4 The gravity changes from January 2003 to January 2016 around the world. The negative signals in the Antarctic, southern Alaska, and Greenland indicate the decreasing of snow/ice mass. The positive signals in northern Canada and Scandinavia come from GIA.

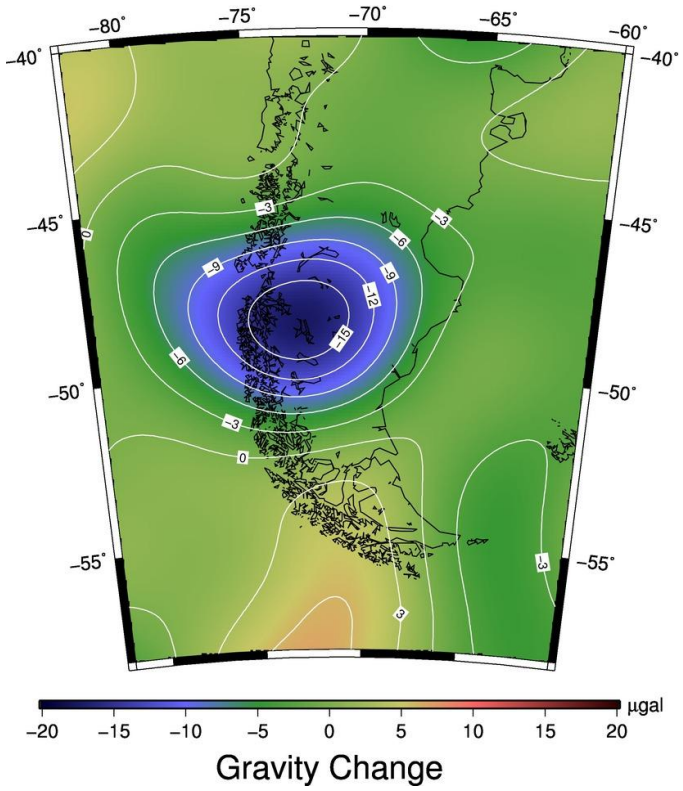

Figure 3.5 The gravity changes from January 2003 to January 2016 in the southern South America. The color scale is different from Figure 3.4. The contour interval is 3 µGal. The negative signal indicates the shrinking of mountain glaciers in Patagonia.

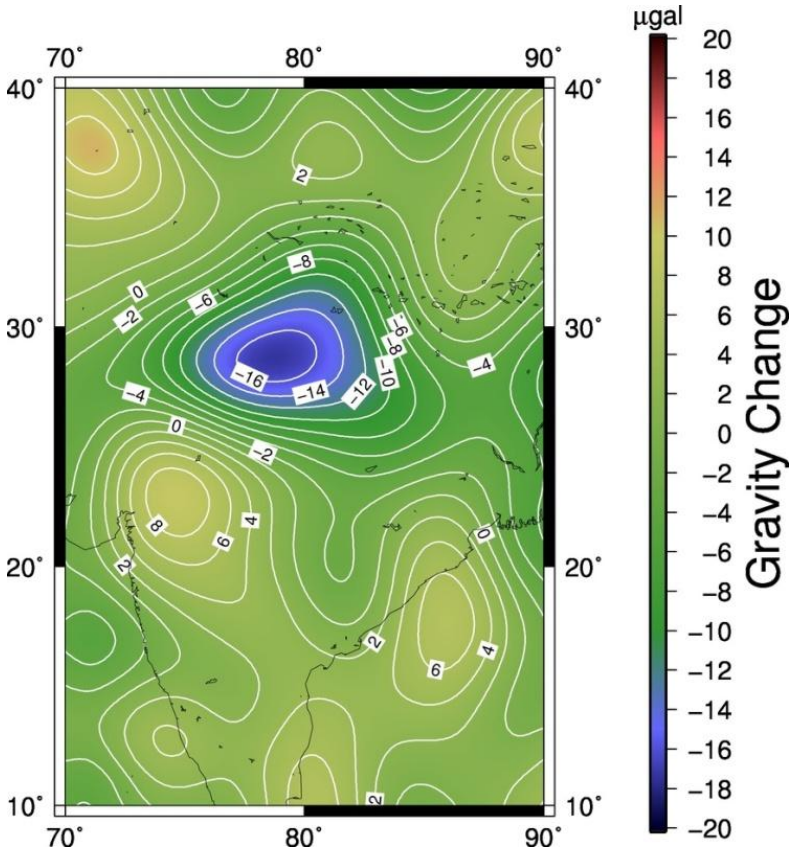

Figure 3.6 The gravity changes from January 2003 to January 2016 in the central and southern Asia. The color scale is different from the previous figures. The contour interval is 2 μGal. The negative signal indicates the decreasing of ice mass in Asian High Mountain region and partly the groundwater in northern India.

Chapter 4
Coseismic gravity changes

4.1 Mechanisms

Coseismic gravity changes are caused by the following two processes, i.e., (1) movements of the boundaries with density contrasts (e.g. the surface and the Moho), and (2) density changes in crust and mantle (Figure 4.1). Additionally, for submarine earthquakes, movement of sea water by ocean floor uplift/subsidence also plays a secondary role to change the gravity. Also, horizontal movements of slant surfaces bring similar effects to surfaces uplift/subsidence (Figure 4.2). However, these topographic contributions are often much smaller than the other mechanisms [*Li et al.*, 2016], and I do not consider this in my thesis.

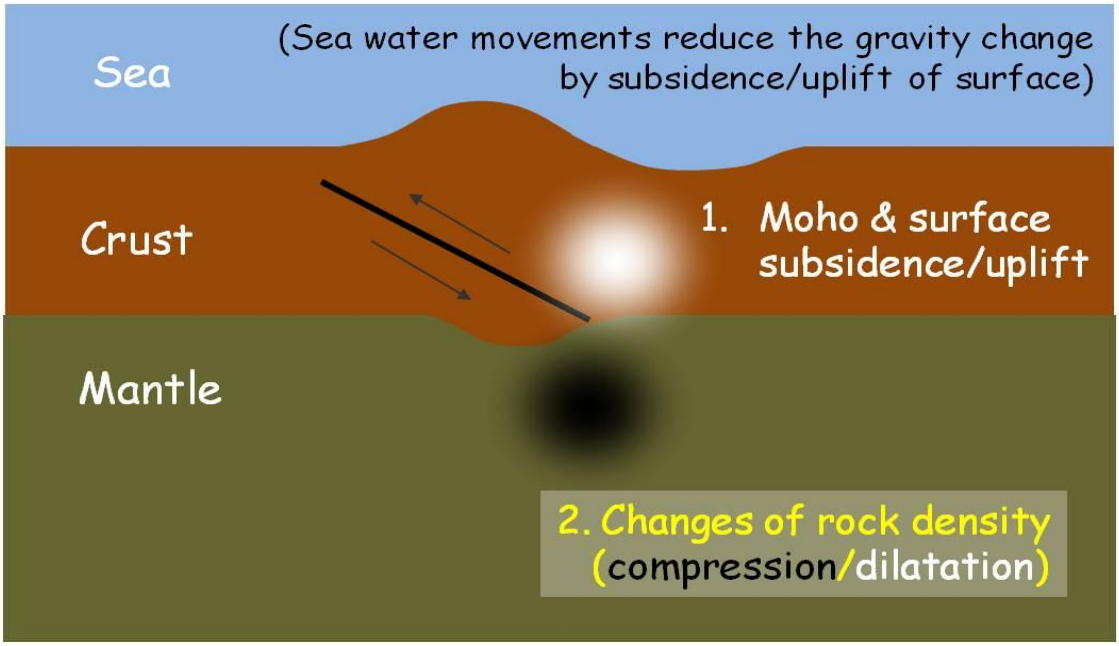

Figure 4.1 The major mechanisms responsible for coseismic gravity changes.

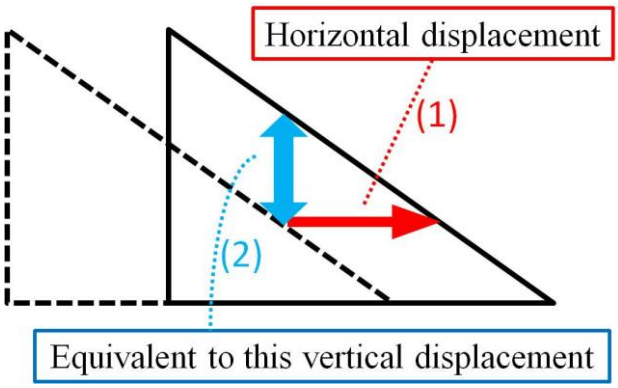

Figure 4.2 A schematic image showing that the horizontal displacements of slant surfaces (1) leave similar gravity change signatures to the vertical displacements (2).

Algorithms to calculate coseismic gravity changes by fault dislocations have been developed for an elastic half space [*Okubo*, 1992] and the realistic earth [*Sun et al.*,

2009]. However, neither of them includes contributions of sea water movements, so that part of the calculation need to be done by ourselves using the equation (4.1) similar to the equation used to derive the Bouguer gravity anomaly.

$$\Delta g = -2\pi G \Delta\rho \Delta h, \tag{4.1}$$

where G is the universal gravity constant, $\Delta\rho = 1{,}700\ (\mathrm{kg/m^3})$ is the difference between the density of water (1,000 kg/m^3) and that of averaging crustal rock at ocean bottom (2,700 kg/m^3), and $\Delta h(\mathrm{m})$ is the amount of vertical movements of the ocean bottom. The negative sign represents the difference between the polarities of Δg and Δh, i.e., gravity changes derived from the above programs must be reduced if the ocean floor experienced coseismic uplifts.

4.2 Previous studies

4.2.1 Ground-based observation

The attempts to observe coseismic gravity changes have been done for a long time. *Barnes* [1966] observed coseismic gravity change by the 1964 Alaska earthquake (M_w9.2) using a relative gravimeter and compared the value of the gravity change to vertical crustal deformation measured by leveling. In Japan, *Tanaka et al.,* [2001] caught a signal of coseismic gravity change of an earthquake with M_w6.1 using an absolute gravimeter. *Imanishi et al.* [2004] first observed coseismic gravity changes on multiple observation points over Japan for the 2003 Tokachi-oki earthquake (M_w8.0) using an array of superconducting gravimeters.

4.2.2 Space-based observation (Satellite gravimetry)

[A] ***The 2004 Sumatra-Andaman earthquake***

The GRACE satellites enabled us to study two-dimensional coseismic gravity changes. The first such report was published by *Han et al.* [2006]. They detected coseismic gravity changes of the 2004 Sumatra-Andaman earthquake (M_w9.2) by calculating the change of gravity distributions over a large area (80E-110E, 10S-20N), using the GRACE data in the same months to cancel contributions of seasonal hydrological gravity changes. They also compared the observation to the gravity changes calculated assuming a fault model and an elastic half space, and concluded that the observed coseismic gravity change was dominated by gravity decrease at the back arc side caused by crustal dilatation. Because the GRACE satellites is more sensitive to longer wavelength components of gravity changes, the crustal dilatation contributed more to the coseismic gravity changes than surface vertical movements.

This research is epoch-making as the first report of a two-dimensional observation of coseismic gravity changes, but has several drawbacks. For example, removal of land hydrology contributions by comparing data from the same month in different years may not work if seasonal changes varied from year to year. In fact, the seasonal gravity changes revealed by the GRACE data are quite irregular (Figure 3.2 c). Moreover, they do not consider postseismic gravity changes, which were not discovered yet in 2006. Another problem is that the coseismic gravity changes by the 2005 Nias earthquake (M_w8.6) are not taken into account. Considering these points, we adopted the methods for time series analysis as explained in Chapter 3. In addition to that, we reanalyzed the co- and postseismic gravity changes of the 2004 Sumatra-Andaman earthquake using the latest GRACE data, and they are explained in detail in Chapter 6.

[B] ***The 2010 Maule earthquake and The 2011 Tohoku-Oki earthquake***

In the early reports about the coseismic gravity changes of the 2010 Maule (Chilean) earthquake (M_w8.8) and the 2011 Tohoku-oki earthquake (M_w9.0), they leveraged the method explained in Chapter 2 (2.2.1 and 2.4) [*Heki and Matsuo*, 2010; *Matsuo and Heki*, 2011]. *Heki and Matsuo* [2010] detected coseismic gravity changes of the 2010 Maule earthquake by using the GLDAS model to remove land water contributions and fitting the function (2.12) with $P(t - t_{eq}) = 0$ for the GRACE data from July 2006 to May 2010. The earthquake occurred on 28 February 2010, the period after the earthquake is even shorter than before, and the temporal resolution of the GRACE data is approximately one month, so the results of analysis do not include postseismic processes. Thus, the $P(t - t_{eq})$ can be ignored. They mapped the value C in the function (2.12) estimated with the least-squares method, and this value corresponds to the coseismic gravity changes. *Matsuo and Heki* [2011] also took the same method to detect the coseismic gravity changes of the 2011 Tohoku-Oki earthquake. *Heki and Matsuo* [2010] and *Matsuo and Heki* [2011] also showed that the results of the observation are explained sufficiently by the theory described earlier (the section 4.1), through the calculation using the software package developed by *Sun et al.* [2009] (Figure 4.3).

Han et al. [2010; 2011] detected the coseismic gravity changes of the 2010 Maule earthquake and the 2011 Tohoku-Oki earthquake directly from Leve-1B data, and *Cambiotti and Sabadini* [2013] leveraged the Slepian function for the time series analysis of the coseismic gravity changes. *Sun and Zhou* [2012] analyzed both northward (+ Fan filter) and downward (+ Fan and de-striping filters) gravity components from the GRACE data to study gravity changes by the 2011 Tohoku-Oki earthquake. In every case, they do not report significant differences from *Heki and*

Matsuo [2010] and *Matsuo and Heki* [2011].

The coseismic gravity change of the 2011 Tohoku-Oki earthquake was also caught by the GOCE satellite [*Fuchs et al.*, 2013]. However, the original purpose of the GOCE satellite was to map the static global gravity (and gravity gradient) fields with a high spatial resolution and accuracy as shown in Figure 1.7, and GOCE observed gravity gradients at same points repeatedly for this purpose. Thus, only low-accuracy data with fewer numbers of observations are available for the time series analysis, so the GOCE data should be used carefully only when it is necessary [*Fuchs et al.*, 2015].

Apart from the gravity, there is an interesting report of the observation of the 2011 Tohoku-Oki earthquake using the GOCE satellites. It flew at altitudes lower than 300 km, and was equipped with very sensitive accelerometers. The atmospheric waves excited by the 2011 Tohoku-Oki earthquake propagated up to the sky and the GOCE satellite detected the passage of the wave at 30 and 55 minutes after the earthquake occurrence above the Pacific Ocean and Europe, respectively [*Garcia et al.*, 2013].

[C] ***The 2012 Indian-Ocean earthquake***

By using Slepian function, *Han et al.* [2015] detected coseismic gravity changes of the 2012 Indian-Ocean earthquake (M_w8.6), which is the biggest strike-slip earthquake observed by modern sensors. The spatial pattern of the coseismic gravity changes was different from those of thrust fault earthquakes such as the 2004 Sumatra-Andaman, the 2010 Maule, and the 2011 Tohoku-Oki earthquakes. The coseismic gravity changes of thrust fault earthquakes are characterized by the gravity decrease on the back-arc side of the arc while this earthquake showed two symmetric pairs of positive and negative anomalies. Although they appear different, it merely

stems from the difference of geometries of the faults and dislocations. Both of them are well explained by the same mechanisms, i.e., change in rock density and vertical deformation of boundaries with density contrasts (Figure 4.3).

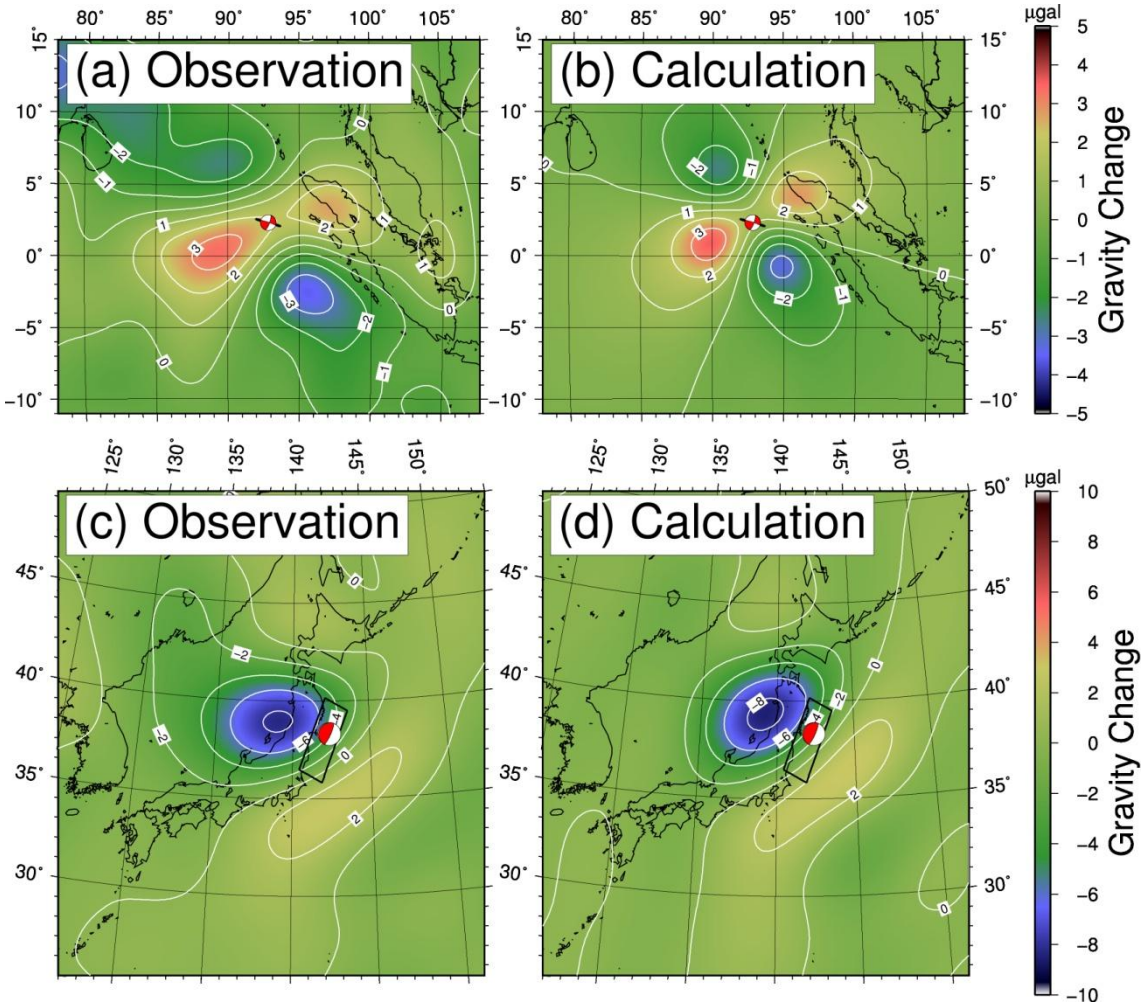

Figure 4.3 Coseismic gravity changes for the 2012 Indian-Ocean earthquake (a, b) and the 2011 Tohoku-Oki earthquake (c, d). The contour intervals are 1 μGal in (a) and (b), and 2 μGal in (c) and (d). (a) and (c) are derived from the GRACE observation data by estimating coseismic steps in the gravity time series at grid points from January 2003 to December 2015. In (a) and (c), contributions of postseismic gravity changes were estimated together with the coseismic steps (see *Tanaka and Heki* [2014] for the function) to avoid their leakage into the coseismic steps. (b) and (d) are calculated by the program developed by *Sun et al*. [2009] using

the fault parameters given in Table 1. Focal mechanisms of the earthquakes are shown at the epicenters of the earthquakes. The black rectangles under beach balls show the surface projections of the faults given in Table 1.

Table 4.1 Fault parameters used to calculate coseismic gravity changes in Figure 4.3. These parameters (rectangular faults with uniform dislocations) were selected so that they well explain the GRACE observation results. Latitudes, longitudes and depths indicate those of the centers of the faults.

	Lat.	Lon.	Disl.	Rake	Depth	Strike	Dip	Length	Width
Indian-Ocean	2.35°	92.82°	35.0 m	185°	20 km	106°	80°	200 km	40 km
Tohoku-Oki	28.00°	142.00°	7.5 m	80°	24 km	205°	9°	450 km	180 km

4.3 The coseismic gravity change of the 2013 Okhotsk deep-focus earthquake

The contents of this section has been published as Tanaka Y.-S., K. Heki, K. Matsuo, and N. V. Shestakov (2015), Crustal subsidence observed by GRACE after the 2013 Okhotsk deep-focus earthquake, Geophysical Research Letters, 42, Issue 9, 3204-3209, doi:10.1002/2015GL063838).

4.3.1 Summary

As explained in Section 4.1, coseismic gravity changes stem from (1) vertical deformation of layer boundaries with density contrast (i.e., surface and Moho) and (2) density (volume) changes of rocks at depth. Such changes have been observed only in large earthquakes with M_w exceeding ~8.5 by the GRACE satellites. On the other hand,

those of M8 class earthquakes have never been detected clearly. Here, I report the coseismic gravity change of the 24 May 2013 Okhotsk deep earthquake (M_w8.3), smaller than the possible detection threshold of M_w8.5. In shallow thrust faulting, the second factor (density change) is dominant, with the first factor (vertical deformation) remaining secondary due to poor spatial resolution of GRACE (i.e., uplift and subsidence occur close by). In the 2013 Okhotsk earthquake, however, the second factor was insignificant because they occur at depth exceeding 600 km. On the other hand, the first factor becomes stronger because the centers of uplift and subsidence are well separated so that GRACE can resolve them. This enables GRACE to map vertical ground movements of deep earthquakes over both land and ocean.

4.3.2 Introduction

Since the launch in 2002, coseismic gravity changes have been observed by the GRACE satellites for several megathrust events as explained in the section 4.2. They are all M_w8.6 or bigger class shallow-depth interplate earthquakes. The detection threshold with GRACE seems to lie around M_w8.5, and coseismic gravity changes have never been detected for M_w8 class earthquakes. It is also important to note that coseismic gravity changes have been detected only for shallow earthquakes.

Earthquakes occurring within subducting slabs with hypocenters deeper than a few hundreds of kilometers seldom exceed M8. Indeed, we know only three recorded M_w8.0 or bigger class earthquakes deeper than 600 km, i.e., the 1970 Colombia earthquake (M_w8.0, depth 645 km) [*Rusakoff et al.*, 1997], the 1994 Bolivian earthquake (M_w8.2, depth 637 km) [*Kikuchi and Kanamori*, 1994], and the 2013 Okhotsk earthquake (M_w8.3, depth 609 km) [*Ye et al.*, 2013; *Zhan et al.*, 2014]. Only the Okhotsk

earthquake occurred after the GRACE launch and provides a unique chance to study coseismic gravity changes induced by a deep-focus earthquake. GNSS stations in Russia have also detected coseismic displacements for this earthquake [*Shestakov et al.*, 2014; *Steblov et al.*, 2014], and they will help us interpret the observed coseismic gravity disturbances.

4.3.3 Gravity data analysis and estimation of coseismic gravity steps

The Stokes' coefficients with degrees and orders complete to 60 in the RL05 monthly GRACE Level 2 data from February 2011 to June 2014 at the Center for Space Research, University of Texas are analyzed. The coefficients of the C_{20} were replaced with those of SLR data [*Cheng and Ries*, 2014]. In order to reduce short-wavelength and striping noises, the Fan filter with the averaging radius of 400 km and the de-striping filter with polynomials of degree 3 for coefficients of orders 15 and higher are applied. Also, the Global Land Data Assimilation System (GLDAS)-NOAH model is leveraged to remove land hydrological signals.

For the time series analysis of gravity changes Δg at a point as the sum of a linear component, average seasonal (annual and semiannual) variation, and a step at May 2013. In other words, the function (2.13) is used with t_{eq} = May 2015 and $P(t - t_{eq}) = 0$ with the least squares at each grid. In addition, their 1σ errors are inferred a posteriori from the post-fit residuals. The linear trend may partly reflect the interannual change of ice volume in the studied region [*Jacob et al.*, 2012].

The least squares estimation is repeated at grid points with 1° separation in order to map the coseismic gravity step C in the function (2.13). Furthermore, two sets of C, i.e., from Δg time series before and after the removal of hydrological signals using

GLDAS are obtained. They are plotted in Figures 4.4 (a) and (b), respectively. Figures 4.4 (c) and (d) show time series of Δg at points where the most significant coseismic steps were seen in (a) and (b), respectively. The point was selected in the oceanic area to show time series with relatively small land hydrological noises. In (d), average seasonal changes are removed, and a negative step associated with the earthquake is recognized. Standard deviations of the post-fit residuals at all grid points at which the time series were calculated ranged only from 0.5 to 1.2 μGal (Figure 4.5), so the signals are significantly larger than the errors.

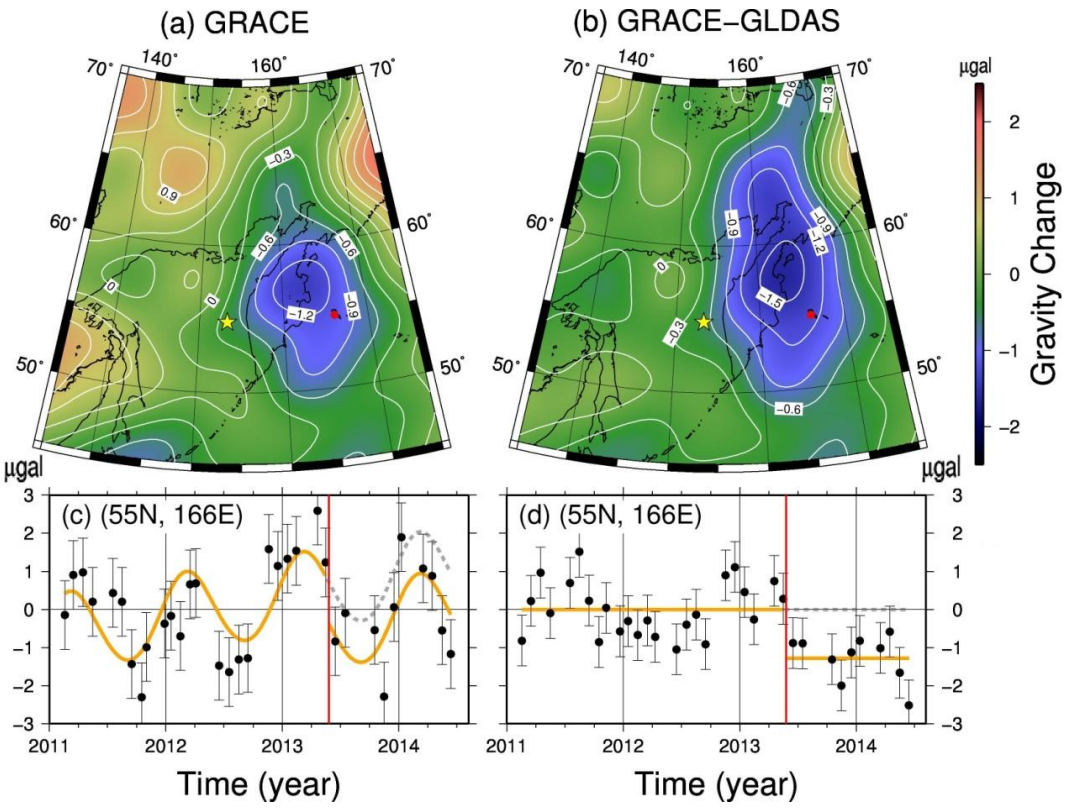

Figure 4.4 (a) The distribution of the coseismic gravity change, *C* in the function (2.13), of the 2013 Okhotsk deep earthquake observed by GRACE. The star shows the epicenter of the earthquake, and the contour interval is 0.3 μGal. (b) Same as (a) but the land hydrological signals have been corrected using the GLDAS model. (c, d) The time series at a grid point (55°N, 166°E) shown as red dots in (a) and (b). In (d), average seasonal changes and the secular trend are removed. There the black circles

show monthly gravity data, whose means are set to zero, and the orange curves and lines are the estimated models (the dashed gray curve and line are the extrapolations of the pre-earthquake model). Error bars represent the root-mean-square error inferred from post-fit residuals. The vertical red lines show the earthquake occurrence.

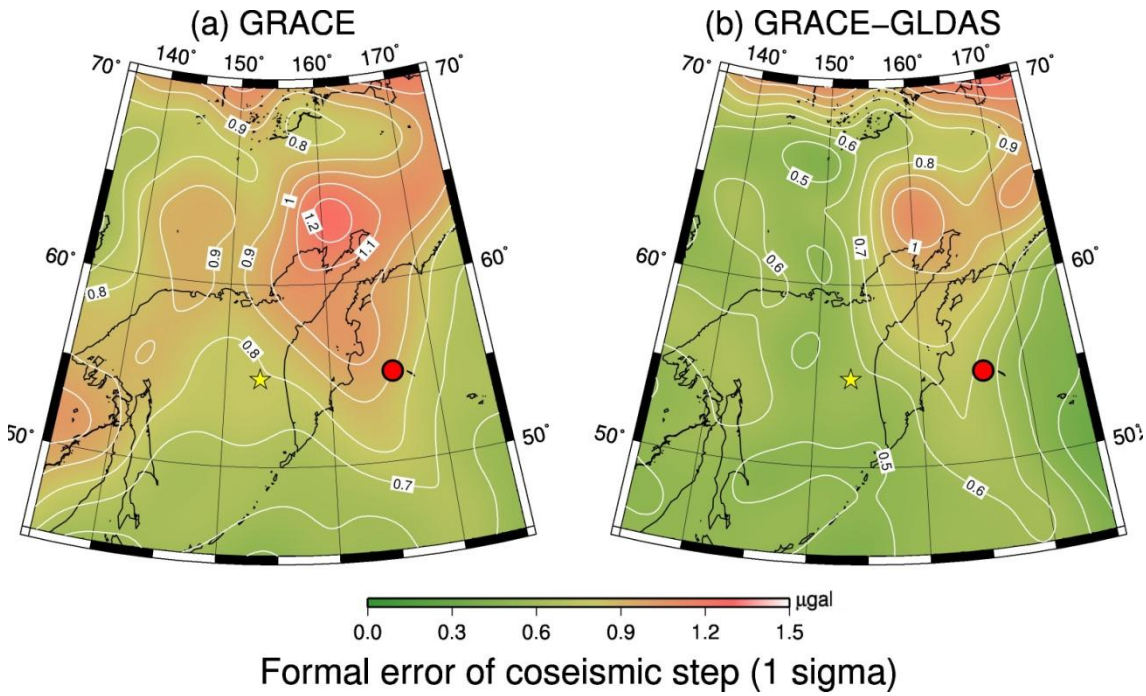

Figure 4.5 The spatial distribution of 1σ formal errors of coseismic gravity step *C* before (a) and after (b) the hydrological correction using the GLDAS model. The error at each grid point was scaled by the post-fit residuals of Δg time series. The red circle is the same as one in Figures 4.3 (a) and (b). Comparison of (a) and (b) suggests that the hydrological correction improves the fit. However, in the region to the north of the Kamchatka Peninsula, uncertainties of *C* still remain large.

In Figure 4.4 (a), a negative anomaly with peak decrease of ~1.5 μGal is seen in the eastern part of the Kamchatka Peninsula. Two positive anomalies appear in the basins of the Amur River (around 130°E, 50°N) and the Lena River (around 130°E,

65°N) in Siberia. These two positive anomalies mostly disappear after the GLDAS corrections and are considered to be of hydrological origin. The GLDAS models often tend to give smaller hydrological changes than GRACE [see *Syed et al.*, 2008, Figure 4], but most of such signals seem to have been removed successfully. On the other hand, the negative anomaly in Kamchatka still remains in Figure 4.4 (b) and is obviously related to the coseismic gravity change of the 2013 deep earthquake. Figure 4.5 shows the standard deviation of the estimated value of C, at each grid. Notable error reduction can be seen after the GLDAS model application because it reduces scatter of gravity data in time series and Δg post-fit residuals (see also Figures 4.4 (c) and (d)). In the next section, I address things that these coseismic gravity changes indicate and the reason why GRACE could detect coseismic gravity changes for an M_w8 class earthquake.

4.3.4 Discussions

[A] ***Gravity changes caused by vertical crustal movements***

Figure 4.6 (a) compares vertical movements observed at 16 GNSS sites and those calculated from the fault parameters by *Shestakov et al*. [2014]. The alternative model by *Steblov et al*. [2014] produces similar displacement pattern. They show relatively large subsidence in Kamchatka and smaller uplift around the Sakhalin Island. The observed displacements show reasonable agreements with the calculated values (Figure 4.6b). The negative gravity changes in Kamchatka from GRACE (Figure 4.4) show similar distribution to the coseismic subsidence (Figure 4.6a).

The contributions of surface vertical movements to gravity changes can be derived by multiplying the vertical displacement by $2\pi\rho G$, where ρ (= 2,700 kg/m^3) is the average crustal density and G is the universal gravitational constant. Then, the

contributions of sea water to the gravity changes are removed (the method is explained in the section 4.1). The sea water correction reduces the gravity changes due to vertical movements of the ocean floor. Results are shown in Figure 4.7 (a). Next, the spatial resolution was adjusted to the same level as GRACE by (1) expanding the calculated distribution into coefficients of spherical harmonics with degrees and orders up to 60, (2) applying the same spatial filters used to process the GRACE data, and (3) converting them back to the space domain. The results are shown in Figure 4.7b. Negative anomalies are expected to appear in Kamchatka, but the signals caused by the uplift near Sakhalin mostly disappear due to the sea water correction and the spatial filtering. Figure 4.7b resembles to Figure 4.4, suggesting that the gravity decreases observed in Kamchatka originate mainly from crustal subsidence.

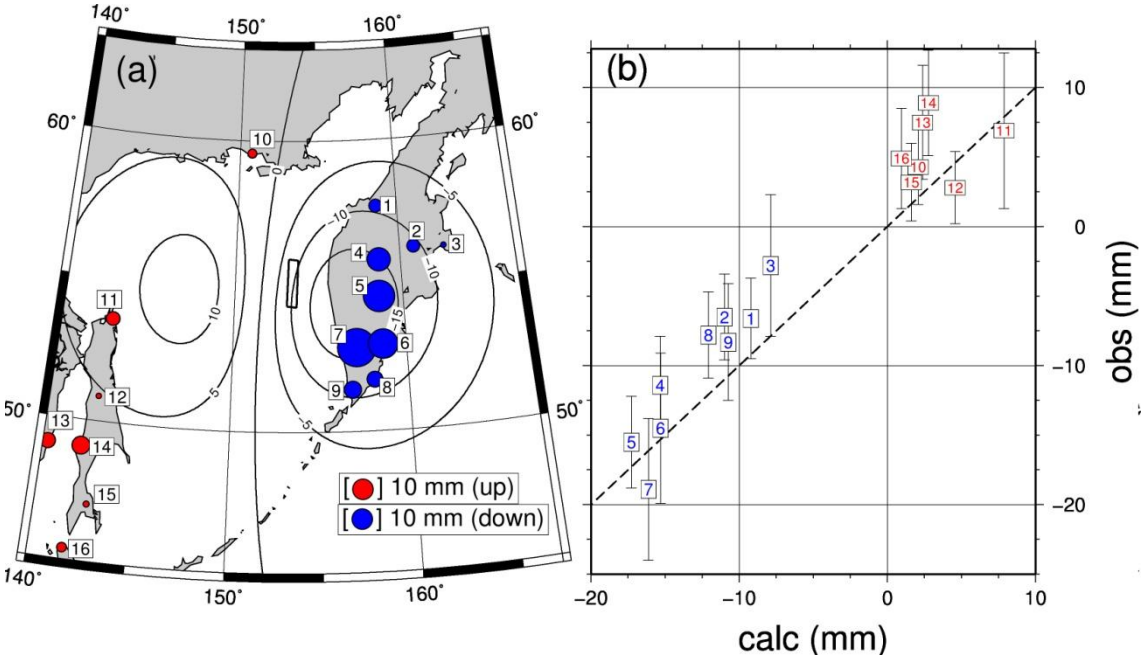

Figure 4.6 (a) Distribution of the observed (circles) and calculated (contours) coseismic vertical displacements after *Shestakov et al.* [2014] and (b) comparison between them. In (a), the contour interval is 5 mm and the black rectangle shows the ruptured fault. The red and blue circles indicate uplift and subsidence, respectively,

and their diameters represent the sizes of displacements. The numbers 1–16 in (a) correspond to those in (b). If the observed and calculated vertical movements are identical, they will align on the dashed line in (b).

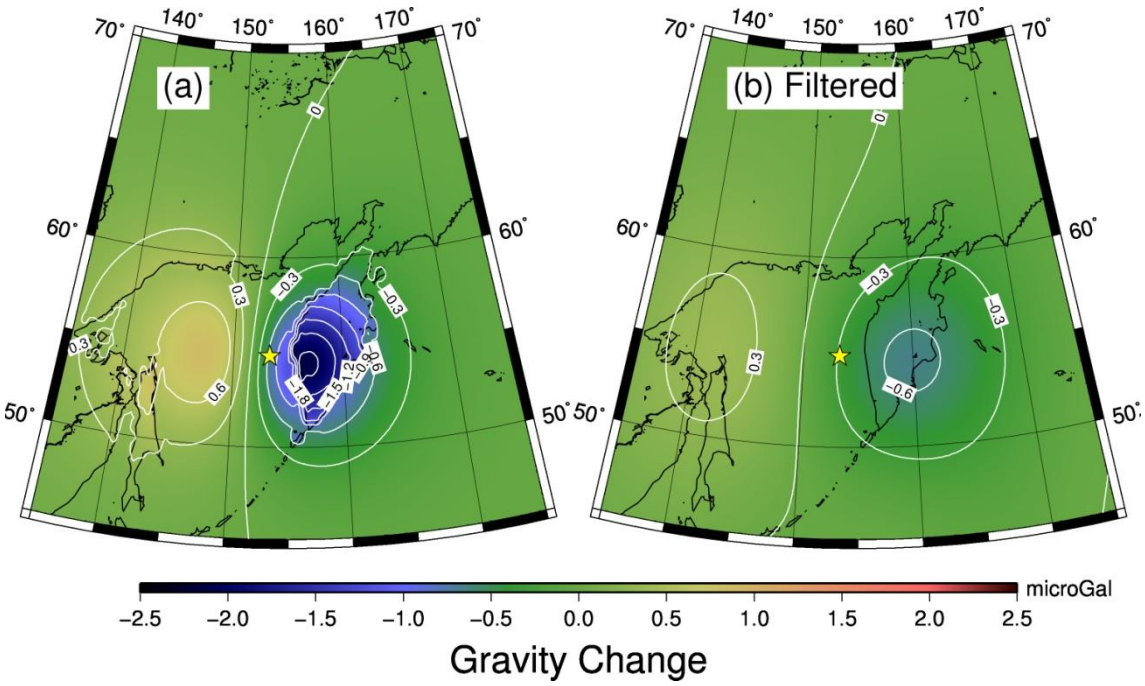

Figure 4.7 (a) The distribution of the gravity change calculated from the vertical displacement and the sea water correction. (b) The same spatial filters as for the GRACE data are applied. The contour intervals are 0.3 μGal. This earthquake also caused horizontal displacements [*Shestakov et al.*, 2014], but they are not considered in the calculation of gravity changes.

[B] ***Density changes versus vertical crustal movements***

Coseismic gravity changes occur by the two mechanisms, i.e., (1) uplift/subsidence of layer boundaries with density contrast, such as surface and Moho, and (2) density changes around the fault edges. In the cases of shallow earthquakes, regions of uplift and subsidence in (1) are close by and the poor spatial resolution of

GRACE often makes it difficult to resolve them. On the other hand, (2) can be detected even from the orbit of GRACE because mass moves downward at the down-dip edge of the fault (in case of shallow thrust faulting).

This can be understood by representing the mass movements with hypothetical mass dipoles using the concept popular in electromagnetics (Figures 4.8a,b). In this analogy, we could compare the positive (excess mass) and the negative (mass deficiency) poles to, e.g., the positive and negative charges of an electric dipole. Then, the perturbing gravity fields would be similar to the electric fields made by the dipole. The mass movement in (1) is equivalent to a horizontal dipole on the ground (although the positive/negative mass anomalies get larger for shallow-angle reverse/normal faulting), while that in (2) is equivalent to a dipole at depth which is nearly vertical for a shallow thrust faulting [see Figure 4a of *Ogawa and Heki*, 2007]. A vertical dipole makes nearly vertical field, while a horizontal dipole makes nearly horizontal field above it (Figure 4.8b). Hence, as long as the vertical components are concerned, a vertical dipole makes larger gravity change signals. The tilt of the vertical dipole may be partly responsible for the shift of the centers of coseismic gravity decrease toward the back-arc side (Figure 4.3c).

In the case of the 2013 Okhotsk deep-focus earthquake, the contributions of the two factor reverse. Two pairs of the density changes occur at the up-dip and down-dip ends of the fault more than 500 km below the surface (Figure 4.9, left). This is equivalent to a gravity quadrupole (Figure 4.8c,d). The gravity field of a quadrupole decays with the fourth power of distance and becomes almost undetectable at the orbital height of GRACE. On the other hand, centers of surface uplift and subsidence go apart as the fault goes downward. The distance becomes comparable to the spatial resolution

of GRACE when the fault is as deep as ~600 km (Figure 4.9, right). They are represented by two monopoles, i.e., positive and negative mass anomalies at the centers of the uplift and subsidence regions, respectively (Figure 4.8c,d). The gravity field of a monopole decays only with the square of the distance and may keep strong enough to be detected at the GRACE orbital height.

This is shown schematically in Figure 4.8 and quantitatively in Figure 4.10. There the contributions of (1) and (2) are composed by assuming an elastic half space [*Okubo*, 1992] by changing the depth of the fault of the 2013 Okhotsk earthquake. Figure 4.10 shows that the factors (1) and (2) are comparable for an earthquake at depth ~10 km. For a fault as deep as ~100 km, (1) becomes 4 times as large as (2). Then, (1) exceeds (2) by an order of magnitude for a fault at ~600 km depth. This simulation study justifies our interpretation that the observed coseismic gravity changes (Figure 4.4) came mostly from vertical crustal movements (Figures 4.6 and 4.7).

The observed changes (Figure 4.4b) are approximately 1 μGal larger than calculated changes (Figure 4.7b). The contribution of Moho uplift/subsidence, not taken into account in this study, may partly account for the underestimation in Figure 4.7b. Although the density contrast of Moho (~500 kg/m^3) is less than that of the Earth's surface (2,700 kg/m^3), the Moho contribution would enhance the gravity change signals because the amplitude of its uplift/subsidence would be greater than that of surface due to its shorter distance to the source of the earthquake. Another complication in this case arises from the non-flat boundaries of density contrast. The cold and dense Pacific Plate slab extends from the trench down to the epicenter of the Okhotsk earthquake, which may slightly modify the coseismic gravity changes. Anyway, these differences do not significantly exceed the errors of the gravity step *C* (Figure 4.5), and quantitative

identification of the error sources might not be easy.

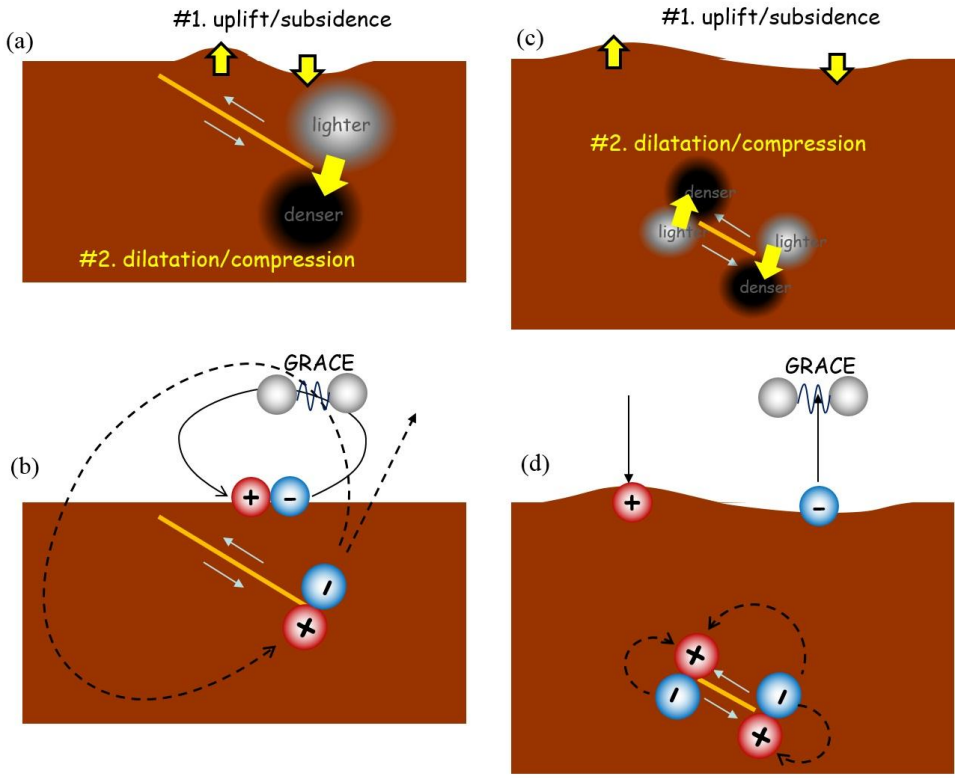

Figure 4.8 The schematic illustration to understand the mechanisms of coseismic gravity changes in shallow (a, b) and deep (c, d) earthquakes with the combination of hypothetical mass dipoles. There are two main mechanisms of the coseismic gravity changes, i.e., (1) surface (and Moho) uplift/subsidence, and (2) dilatation/compression under the ground. In the cases of shallow earthquakes, subsidence and uplift occur close by and GRACE cannot resolve them (a). On the other hand, density changes can be caught because the mass movement is vertical. This can be intuitively understood by considering two hypothetical sets of mass dipoles representing mass movements (strengths of the positive and negative poles do not coincide in real cases), a horizontal dipole for (1) and an upright dipole for (2) (b). Only (2) makes vertical field (i.e., changes the gravity strength) at the GRACE altitude. Solid and dashed arrow lines indicate the gravity perturbing field due to mass movements made by the mechanisms (1) and (2), respectively. In the cases of the deep earthquakes, surface/Moho uplift/subsidence are well separated that GRACE can resolve them (c). At the same time, the contribution of density changes

becomes too small to be detected. This situation could be understood intuitively by considering two mass monopoles for (1) and a deep quadrupole for (2) (d). These situations are quantitatively shown in Figure 4.10.

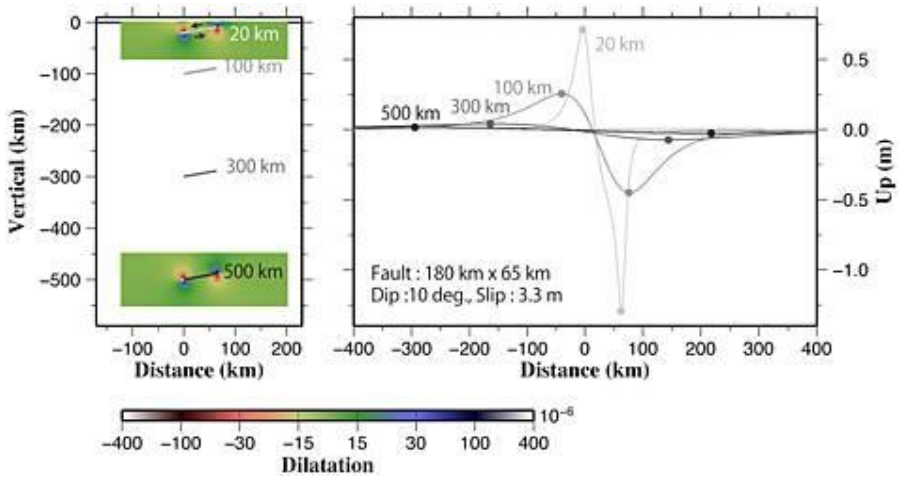

Figure 4.9 The depth of the fault of the 2013 Okhotsk earthquake has been changed to 20 km, 100 km, 300 km, and 500 km (left), and surface vertical crustal movements are compared (right). Density changes due to the faulting are shown with color for the faulting at 20 km and 500 km depths. Although the density change patterns are similar, the centers of surface uplift and subsidence (marked with gray dots) go apart for larger fault depths, exceeding the radius of spatial averaging of the GRACE data (400 km in this study). An elastic half space was assumed in calculating coseismic displacements and strain changes [Okada, 1992].

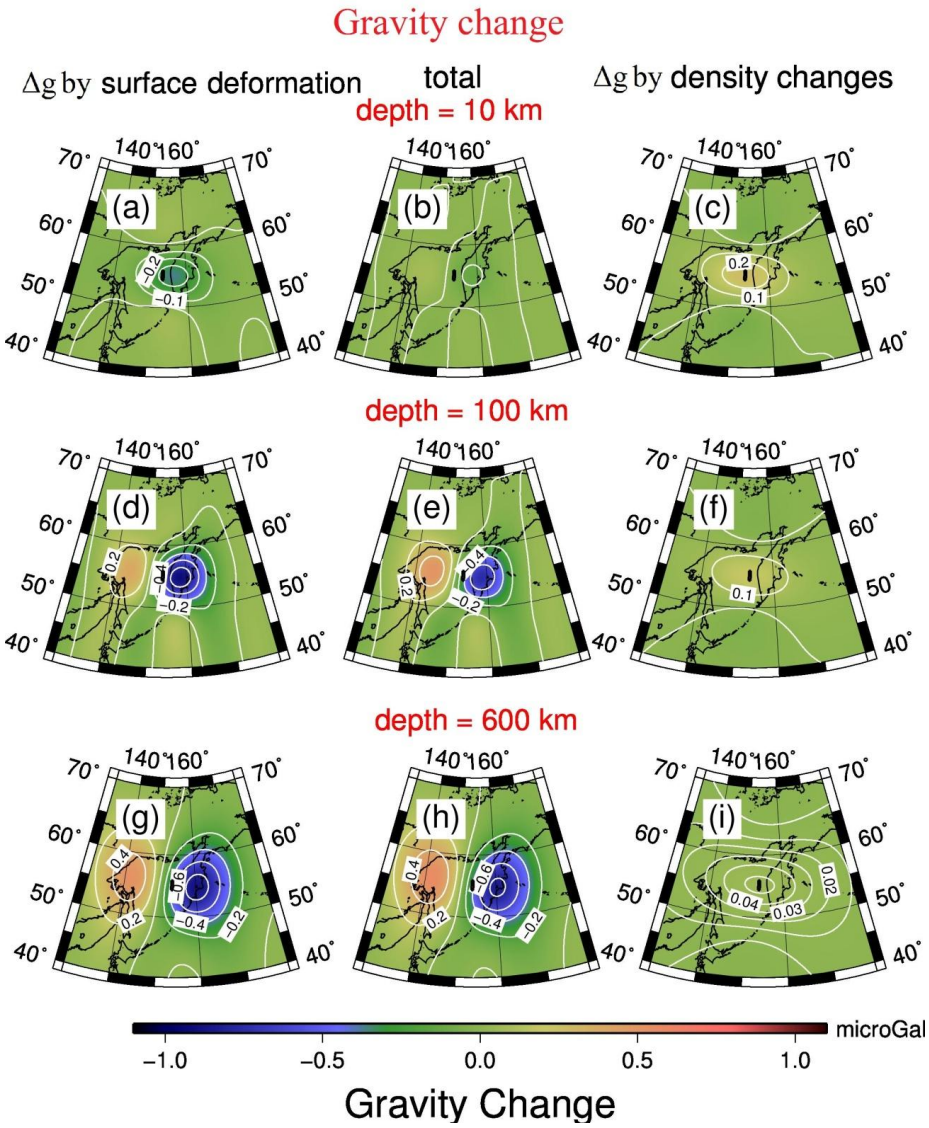

Figure 4.10. Coseismic gravity changes calculated assuming an elastic half space [*Okubo et al.*, 1992] without sea water correction. The same spatial filters as the GRACE data have been applied. The fault parameters are the same as those shown in Figure 4.6 but the fault depth has been changed to 10 km (a-c), 100 km (d-f), and 600 km (g-i). These figures show that deeper earthquakes reduce the importance of the density changes (right) relative to surface vertical movements (left) in the total changes (center). In fact, (a-c) shows that the contribution of the density changes of an earthquake at the depth of 10 km is about 0.2 μGal, similar to that of the vertical deformations (-0.3 μGal). When the fault depth is 100 km, as shown in (d-f), surface vertical movement decreases the gravity by 0.8 μGal. This is much larger than 0.2 μGal by the density changes. The density change contribution diminishes to 0.05 μGal when the fault depth is 600 km (g-i).

4.3.5 Conclusions of the section 4.3

For the first time, the GRACE satellites detected coseismic gravity changes invoked by the deep-focus seismic event—the M_w8.3 2013 Okhotsk earthquake. Its extraordinary focal depth was the key factor to make them visible. Although part of the gravity changes may originate from the deformation of Moho and other subsurface structures, they mainly reflect vertical surface deformation, and this makes GRACE a tool with new perspective to map coseismic vertical ground deformations. Although its spatial resolution is limited, satellite gravimetry is useful in both land and sea and could complement interferometric synthetic aperture radar (InSAR) satellites and terrestrial GNSS networks in mapping vertical crustal movements of deep earthquakes.

4.4 Other related studies

The results and conclusions of *Tanaka Y.-S. et al.* [2015] about the coseismic gravity changes of the 2013 Okhotsk deep-focus earthquake was supported by *Zhang et al.* [2016]. They calculated coseismic gravity changes of the 2013 Okhotsk deep-focus earthquake based on a spherical earth model and reached the same conclusion: the GRACE satellite can map two-dimensional vertical crustal deformation by deep-focus earthquakes. They also indicate that the contribution of the vertical displacements to coseismic gravity changes of this earthquake was four times as large as that of impression and dilatation in mantle.

Wang et al. [2012b] estimated fault parameters of the 2010 Maule earthquake from the spatial distribution of the coseismic gravity changes derived by the time series analysis of coefficients of the Slepian functions. *Fuchs et al.* [2015] reported that joint inversion method of the GRACE and GOCE gravity data, and the GNSS displacement

data can improve fault slip inversion results because satellite gravimetry provides the data over the ocean and the land with the same accuracy.

Han et al. [2013] estimated fault parameters using the Slepian functions for five large earthquakes, i.e., the 2004 Sumatra-Andaman, the 2007 Bengkulu, the 2010 Maule, the 2011 Tohoku-Oki, and the 2012 Indian-Ocean earthquakes. Recently, *Dai et al.* [2016] also estimated fault parameters of these five earthquakes and the 2005 Nias earthquake, using the north components of coseismic gravity and gravity gradient changes following the method proposed by *Han et al.* [2013]. However, the estimated fault parameters are not consistent with those derived in other reports based on GNSS, seismometer, or so on. According to *Dai et al.* [2016], the difference comes from the ability of GRACE to measure the gravity over the land and ocean with the same accuracy, but it is still unclear that the parameters can explain observation results from other sensors. *Cambiotti and Sabadini* [2012] also analyzed the time series of the GRACE data with the Slepian functions to detect the coseismic gravity changes of the 2011 Tohoku-Oki earthquake, and estimated the fault parameters.

Montagner et al. [2009] reported that they detected gravity signal of the on-going fault rupture during the main shock of the 2011 Tohoku-Oki earthquake. This was the first observation of a phenomenon predicted by the theory connecting the gravity perturbation and fault dislocation by *Harms* [2006]. The signal of gravity changes expands at the speed of light, so the gravity observation would allow us to detect occurrences of earthquakes with less time delay in the future.

4.5 Conclusions of the Chapter 4

The validity of the theory on the mechanisms of coseismic gravity changes has

already been repeatedly tested. The GRACE observations of coseismic gravity changes are now leveraged together with other data such as GNSS or seismometers to study physical processes of earthquakes.

In Japan, we have dense observation networks of GNSS and seismometers. The GRACE data are inferior to those of GNSS or seismometers in the spatial and temporal resolutions (~300 km and ~30 days, respectively). Nevertheless, the GRACE data have certain advantages over GNSS and seismometers because the GRACE satellites can measure the world-wide gravity change with uniform accuracy over the ground and the ocean. The coseismic gravity changes from GRACE observations have already begun to be used to recover fault slip distributions by joint analyses with other kinds of data. The GRACE data are also found useful to evaluate fault parameters estimated by other observations by examining if they also can explain coseismic gravity changes. They will certainly continue to contribute to earthquake studies in the future.

Chapter 5
Postseismic gravity changes

5.1 Mechanisms

Following rapid ground movements by main shocks of earthquakes, slow movements are often observed by GNSS. They can be caused by afterslip (slow fault slip following the rapid rupture), poroelastic rebound (followed by water diffusion), and viscoelastic relaxation (viscous flow of the mantle as Newtonian fluid). Mass redistribution by those mechanisms can also cause postseismic gravity changes, which would proceed slowly after coseismic gravity changes. Among others, viscoelastic relaxation is considered to cause long-term postseismic gravity changes, continuing for years to decades. Theoretical studies about postseismic gravity changes by viscoelastic relaxation have been performed by *Pollitz* [1992; 1997; 2003] and *Tanaka Y.-Y. et al.* [2006; 2007; 2009] using preexisting theoretical works to explain glacial isostatic adjustment (GIA) based on normal-modes [*Peltier*, 1974]. The gravity changes predicted by these theories have been compared with the GRACE observation results of postseismic gravity changes, e.g. after the 2004 Sumatra-Andaman earthquake [*Tanaka Y.-Y. et al.* 2015]. On the other hand, the contributions of afterslip and water diffusion are not discussed in those reports.

5.2 Long-term postseismic gravity changes of the 2004 Sumatra-Andaman earthquake

Ogawa and Heki [2007] first detected postseismic gravity changes by satellite gravimetry for the 2004 Sumatra-Andaman earthquake. At that time, they used the Level-2, Release 1 GRACE data, which are noisier than the latest solutions because of older geophysical models used for various corrections to the range-rate between GRACE-A and GRACE-B. In order to reduce noise, *Ogawa and Heki* [2007] converted the GRACE data into geoid heights which are more sensitive to lower degree components. They analyzed the time series of the geoid height, changing the $P(t - t_{eq})$ in function (2.13) into

$$P(t - t_{eq}) = a_7 \left\{1 - \exp\left(\frac{-(t-t_{eq})}{0.6}\right)\right\} \qquad (5.1)$$

where a_7 is a constant to be estimated by the least-squares method, and 0.6 (year) is the time constant for postseismic gravity changes.

By eliminating hypotheses with serious difficulties, *Ogawa and Heki* [2007] considered that the water diffusion was the most probable mechanism responsible for the observed postseismic gravity (geoid height) changes. First, they ruled out the afterslip because it would change gravity with the same polarity as the coseismic gravity changes. In fact, the co- and postseismic gravity changes had different polarities. Second, they considered that viscous relaxation of the upper mantle unlikely. They thought that the time constant of 0.6 year, observed for the postseismic change, is too short for viscoelastic relaxation. The Maxwell time of the upper mantle beneath arcs would be ~20 years if we assume the mantle viscosity of $\sim 2.5 \times 10^{19}$ (Pa s) inferred from the 1960 Chile earthquake [*Hu et al.*, 2004].

However, after *Ogawa and Heki* [2007], several reports suggested that the

viscosity of upper mantle might be lower than it had been thought and the long-term postseismic gravity changes were dominated by viscoelastic relaxation. For example, *Tanaka Y.-Y. et al.* [2015] and *Han et al.* [2014] reported that the observation results of the postseismic gravity changes of the 2004 Sumatra-Andaman earthquake can be explained sufficiently by viscoelastic relaxation with the viscosity of the order of 10^{18} Pa s.

5.3 Two components of postseismic gravity changes

The contents of this section except for the section 5.3.4 have already been published as Tanaka Y.-S. and K. Heki (2014), Long- and short-term postseismic gravity changes of megathrust earthquakes from satellite gravimetry, Geophysical Research Letters, 41, Issue 15, 5451-5456, doi:10.1002/2014GL060559)

5.3.1 Summary

The time series analysis with monthly GRACE data revealed that postseismic gravity changes are composed of short- and long-term components. The result of the analysis about three M9 class earthquakes (the 2004 Sumatra-Andaman earthquake, 2010 Maule earthquake, and the 2011 Tohoku-Oki earthquake) showed that the gravity typically (1) decreases coseismically, (2) continues to decrease for a few months, and (3) increases over a longer period. Therefore, postseismic gravity changes have two components with different time constants and polarities. The mechanisms of short- and long-term postseismic gravity changes are not as clear as coseismic changes at the

moment, but might be explained to some extent with afterslip and the Maxwell viscoelasticity, respectively. These two components are difficult to discriminate with surface velocity measurements because the forearc area moves trenchward at both stages. They appear in different polarities in gravity, making satellite gravimetry a unique tool to separate them.

5.3.2 Introduction

As explained above, the GRACE satellites observed co- and postseismic gravity changes of the 2004 Sumatra-Andaman earthquake. Especially, postseismic gravity changes were first found after this earthquake [*Ogawa and Heki*, 2007; *Chen et al.*, 2007]. Postseismic gravity changes of this earthquake are characterized by gravity increases around the ruptured fault, while its coseismic gravity changes are characterized by gravity decreases on the back arc side (Figure 5.1). Postseismic gravity changes have been attributed to viscous relaxation of low-viscosity upper mantle rocks [e.g. *Han et al.*, 2008; *Panet et al.*, 2010]. However, all of the reports were based on GRACE data older than Release 5, which became available in 2012. Also, it is only for the 2004 Sumatra-Andaman earthquake that postseismic gravity changes have been investigated. Thus, here, I study all of the three M9 class earthquakes after the GRACE launch in 2002, i.e., the 2004 Sumatra-Andaman earthquake, the 2010 Maule earthquake, and the 2011 Tohoku-Oki earthquake, using the Release 5 data in order to find common features in the three examples.

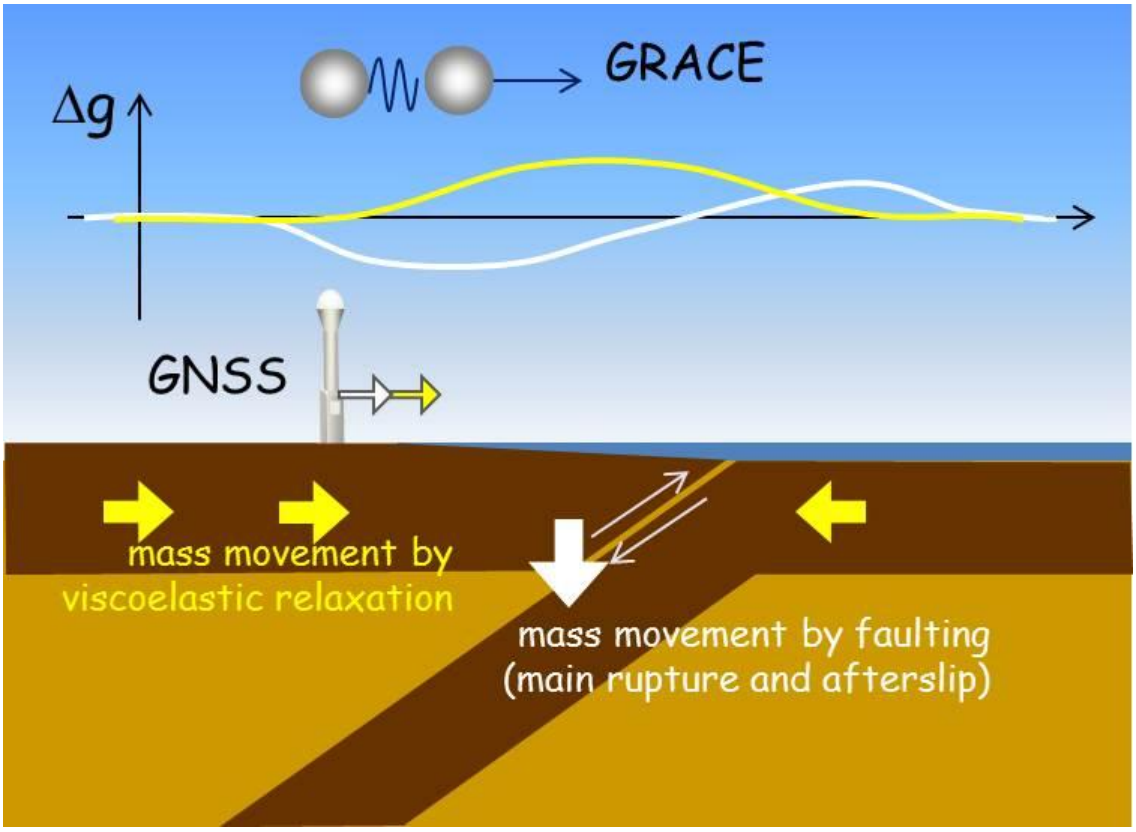

Figure 5.1 Rough sketch of mass movements associated with faulting (white arrow) and Maxwellian viscous relaxation (yellow arrows). Both of them cause trenchward movements of GNSS stations on the arc, but GRACE can see the transition from the former to the latter because gravity changes associated with these two stages occur in opposite polarities.

5.3.3 Gravity data and time series analyses

Here I use the Stokes' coefficients with degrees and orders up to 60 in the Release 5 monthly GRACE data from August 2002 to December 2013 analyzed at the Center for Space Research, Univ. Texas. In the time series analyses, a time window of August 2002 - December 2008 is set for the 2004 Sumatra-Andaman earthquake, January 2006 - December 2013 for the 2010 Maule earthquake, and January 2008 - December 2013 for the 2011 Tohoku-Oki earthquake. For the 2004 earthquake, the GRACE data after January 2009 is excluded to make its time window of similar length to the other two

cases.

To reduce short-wavelength and striping noises, Fan filter with an averaging radius of 250 km and de-striping filter with polynomials of degree 3 for coefficients of orders 15 and higher are applied. About land water contributions, two cases are examined, with and without the land hydrology correction by the GLDAS model. Here, the data without the correction are employed, and only average seasonal hydrological contributions are removed by modeling the average annual and semiannual variations in the gravity time series. The Sumatra and Northeast Japan regions are dominated with sea, and the GLDAS corrections do not yield significant differences. In the Chilean case, fairly large hydrological signals were seen in the continental region to the east, but GLDAS did not effectively reduce them. There was a severe drought in South America in 2010 [e.g. *Lewis et al.*, 2011], and this may not be well modeled in GLDAS.

Figure 5.2 shows the gravity time series at a point just above the fault of the 2004 Sumatra-Andaman earthquake (black circle in Figure 5.3a). Average seasonal changes and linear trends were removed. Here, the time series was modeled with the function (2.13). The postseismic gravity changes represented by $P(t - t_{eq})$ are modeled with the combination of two exponential functions with different time constants of τ_1 and τ_2 ($\tau_1 < \tau_2$), i.e.,

$$P(t - t_{eq}) = a_7 \left\{1 - exp\left(\frac{-(t-t_{eq})}{\tau_1}\right)\right\} + a_8 \left\{1 - exp\left(\frac{-(t-t_{eq})}{\tau_2}\right)\right\} \quad (5.2)$$

In Figure 5.2, the time series was modeled in two different ways. First (red curve), the postseismic change is modeled with a single exponential decay function (i.e., a_7 is fixed to zero). The time constant τ_2 is fixed to 1.5 years, and the eight parameters of a_1

– a_6, a_8 and C in the function (2.13) with (5.2) are estimated with the least-squares method. The data show slight misfit from the model at the early postseismic stage, i.e., gravity keeps decreasing for a few months immediately after the earthquake.

Second (blue curve), two exponential decay functions are considered, and a_7 is added as a parameter to be estimated. Various values for the time constants τ_1 and τ_2 are verified and τ_1 = 0.25 (yr) and τ_2 = 0.90 (yr) minimized the post-fit residuals of the gravity data (Figure 5.2 right). The shorter time constant (τ_1 = 0.25 yr) fits well (and the longer time constant τ_2 does not) with the eastward movement of the GNSS station at SAMP in North Sumatra (Figure 5.5a) for the three months postseismic period (the 2005 Nias earthquake occurred ~3 months after the Sumatra-Andaman event and disrupted the time series).

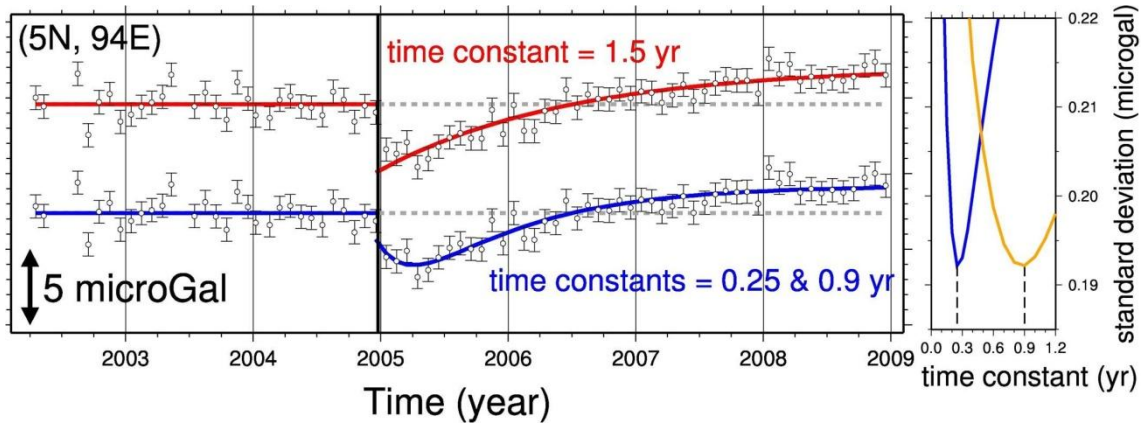

Figure 5.2 Time series of gravity changes before and after the 2004 Sumatra-Andaman earthquake (black vertical line) at (5N, 94E) fitted with two different models. Average seasonal changes and the secular trend have been removed. With the red and blue curves, the postseismic changes are modeled with one ($\tau_1 = 1.5$ yr) and two exponential decay functions ($\tau_1 = 0.25$ yr and $\tau_2 = 0.90$ yr), respectively. The right figure shows the sensitivity of the standard deviation of

the gravity data residuals 2005.0 - 2005.5 to the changes of one of the time constants (blue: τ_1, yellow: τ_2) for the two-function model. The data and the blue curve appear again and are compared with other events in Figure 5.3.

At each of the grid points with 1 degree separation, the time series of the GRACE data are modeled using the function (2.13) and (5.2). The same values for τ_1 and τ_2 are used and the same set of parameters is estimated. The average post-fit residual of the gravity was ~0.5 μGal. The residuals tend to be larger/smaller at grid points within land/sea, but remain within 0.4-0.7 μGal at most of the points. The geographical distributions of the estimated parameters C, a_7 and a_8 are shown in Figure 5.3a-c (a_7 and a_8 are scaled so that they show 1 year cumulative changes).

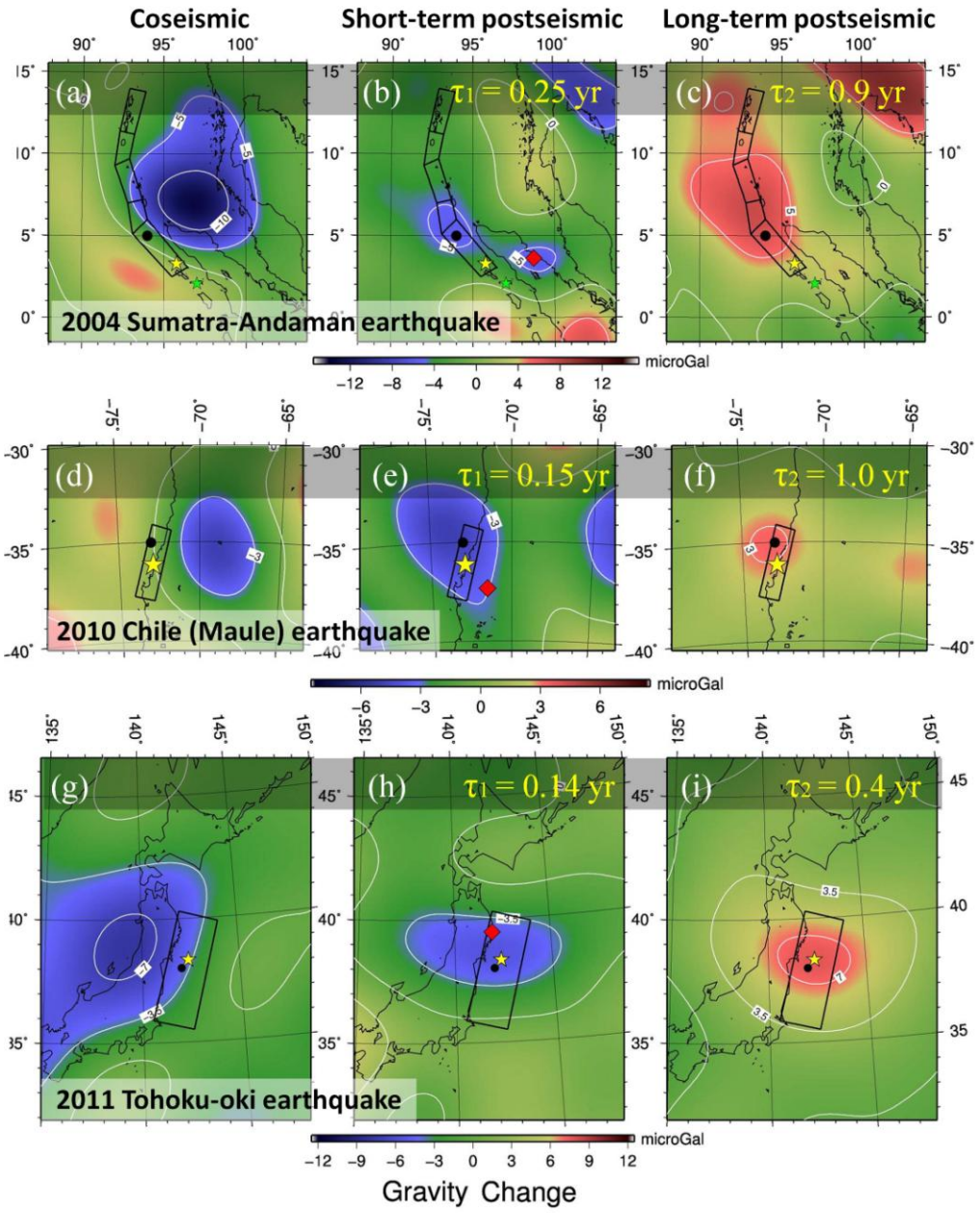

Figure 5.3 Coseismic (left), and short- (middle) and long-term (right) postseismic gravity changes (expressed with 1 year cumulative changes) of the 2004 Sumatra-Andaman earthquake (high), the 2010 Maule earthquake (middle), and the 2011 Tohoku-Oki earthquake (low). Time constants for the postseismic changes are shown on the middle and right columns. The yellow stars and black rectangles show the epicenters and the ruptured faults. The black circles show points whose gravity changes are shown in Figures 5.2 and 5.4, and red diamonds in the middle column show GNSS stations shown in Figure 5.6. The contour intervals in high, middle, and low rows are 5, 3, and 3.5 μGal, respectively.

The time series for the 2010 Maule earthquake and the 2011 Tohoku-Oki earthquake were also modeled using the functions (2.13) and (5.2), and shown in Figure 5.4. For these two earthquakes, it was difficult to constrain the shorter time constants in this way (residuals did not show clear minima like in the 2004 Sumatra-Andaman earthquake). Instead, based on an assumption that the short-term postseismic gravity changes in these two earthquakes obey the same exponential decay as surface displacements, the time constants of 0.15 and 0.14 yr are given because of their best-fits to the GNSS data during the first four postseismic months (Figure 5.5b, c). In such a short timescale, Maxwellian viscous relaxation would contribute little, and afterslips would be mainly responsible for these changes. Figure 5.3d–h shows the distribution of C, a_7 and a_8 for these two events. The values of τ_1 and τ_2 are shown in the middle and right columns of Figure 5.3.

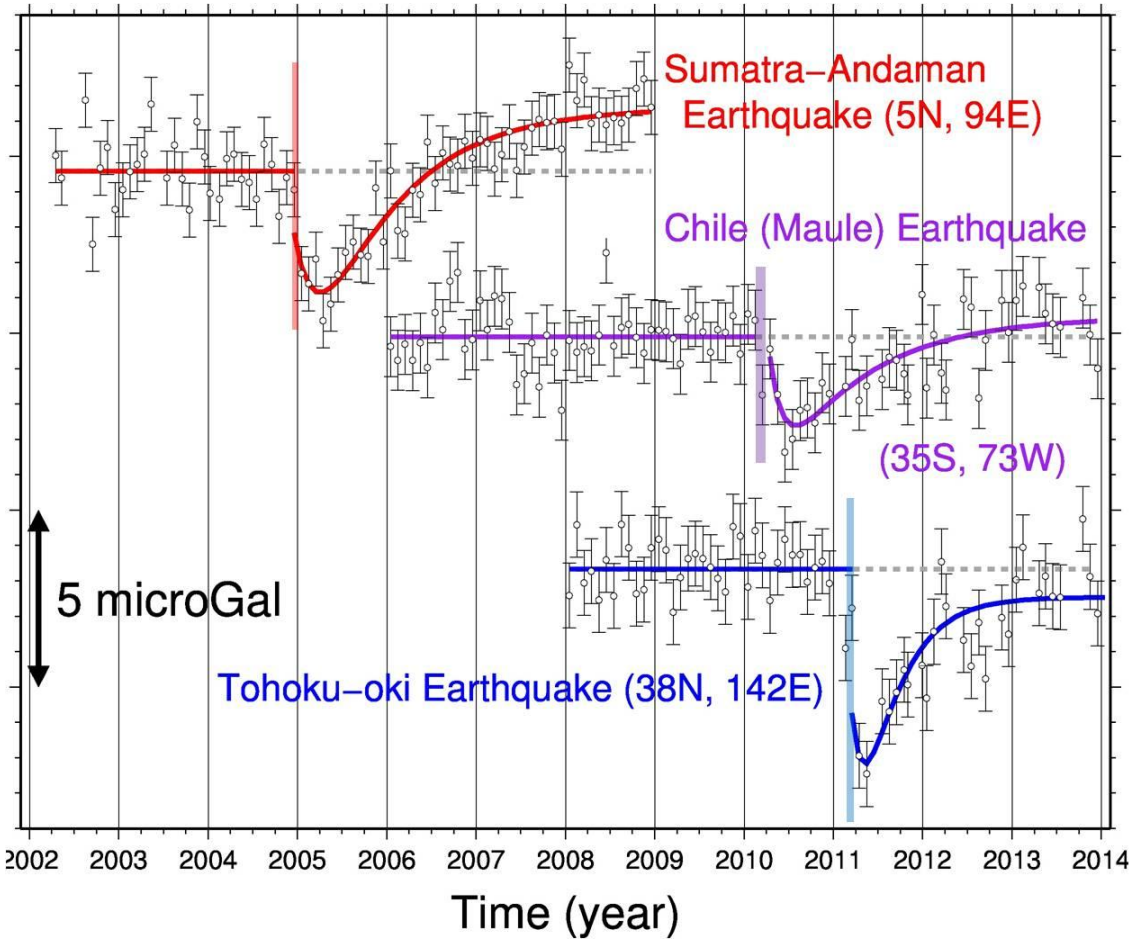

Figure 5.4 Time series of gravity changes before and after the three megathrusts (colored vertical lines) at points close to the epicenters (black circles in Figure 5.3). Errors are assumed uniform in time, and have been scaled using post-fit residuals (0.5 - 0.6 μGal in this figure). Land hydrology corrections are not performed, but the average seasonal changes and secular trends are removed. All the three cases suggest the existence of two postseismic gravity change components with distinct time constants and polarities. The transition from decrease to increase is quicker in the 2011 Tohoku-Oki earthquake than the other two because the time constant of its long-term component is relatively short (0.4 yr).

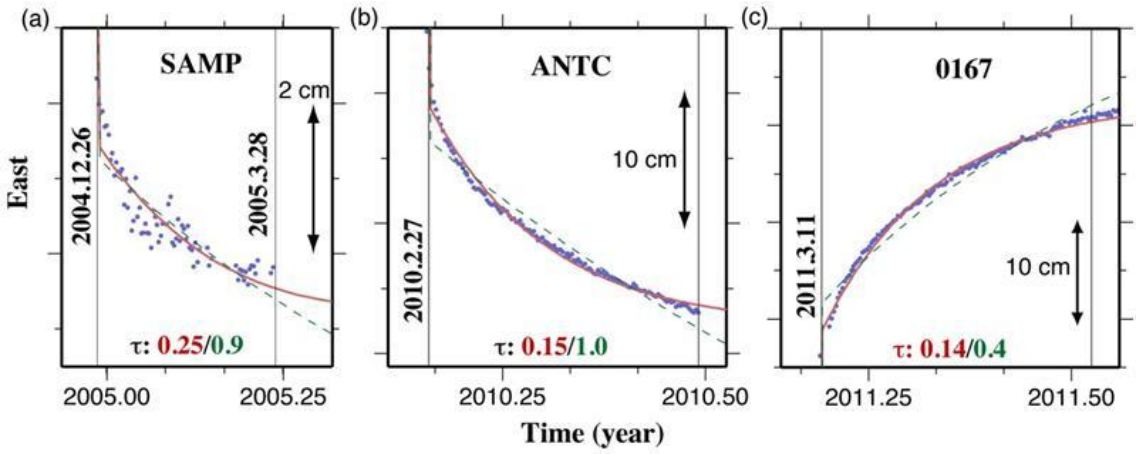

Figure 5.5 East components of the movements of the GNSS stations (SAMP, ANTC, and 0167 shown in Figure 5.3b, e, h) showing postseismic crustal movements over 3–4 months after the three megathrust events. The data are from http://sideshow.jpl.nasa.gov/post/series.html (SAMP and ANTC) and http://mekira.gsi.go.jp (0167). The solid (red) and dashed (blue) curves are the best-fit exponential decay functions with the time constants of the short- and long-term postseismic gravity changes (shown at the bottom), respectively.

5.3.4 Verification with AIC

In order to justify the selection of the function I employed (5.2) objectively, I use the Akaike's Information Criterion (AIC) [*Akaike*, 1974]. AIC helps us infer the appropriateness of a given statistical model. In this case, the fitted function giving the least AIC is considered to be the most appropriate model from a statistical point of view. According to *Nishimura et al.* [2013], AIC can be calculated as follows:

$$\mathrm{AIC} = n\ln(2\pi) + n\ln\frac{\sum_{i=1}^{n}(O_i - C_i)^2}{n} + n + 2k$$

where n and k are the numbers of the observations and the model parameters,

respectively, and O_i and C_i are the i-th observation and calculation, respectively.

I calculated AICs using the three gravity time series shown in Figure 5.4 over the one-year period after the earthquake, changing the number of exponential functions of $P(t - t_{eq})$ in the equation (5.2) from one to four. The time constants except for those used above were estimated by the grid search from 0.1 to 40 years with the step of 0.1 year to all the data used in Figure 5.4. The results are summarized in Table 5.1. For the 2004 Sumatra-Andaman earthquake and the 2010 Maule earthquake, the models with short- and long-term exponentials give the least AICs. However, for the 2011 Tohoku-Oki earthquake, the single exponential model gives the least AIC probably because this earthquake occurred in the middle of March, and the data used to calculate AIC (April 2011 to March 2012) may not include the most significant part (March 12- March 31) of the afterslip contribution. Moreover, the GRACE data for June 2011 is missing, which also reduces the afterslip contribution to the gravity time series. Without afterslip, the postseismic gravity changes come dominantly from viscoelastic relaxation of the mantle. Hence, the statistical results may indicate that just a single exponential function is enough to model the observed changes.

Table 5.1 Comparison of the AIC for the gravity time series shown in Figure 5.4. The AICs were calculated for the one-year data after the earthquakes. The number of exponential functions of $P(t - t_{eq})$ in the equation (5.2) is changed from one to four to find which model gives the least AIC.

Earthquake	The number of EXPs	Time constants (year)	AIC
The 2004 Sumatra-Andaman Earthquake (5N, 94E)	1	2.7	44.5
	2	**0.25, 0.9**	**43.0**
	3	0.25, 0.9, 0.1	44.3
	4	0.25, 0.9, 0.1, 5.6	45.6
The 2010 Maule earthquake (35S, 73W)	1	40	39.3
	2	**0.15, 1.0**	**31.0**
	3	0.15, 1.0, 0.1	32.8
	4	0.15, 1.0, 0.1, 5.0	32.5
The 2011 Tohoku-Oki Earthquake (38N, 142E)	**1**	**1.2**	**39.0**
	2	0.14, 0.4	41.2
	3	0.14, 0.4, 40	42.5
	4	0.14, 0.4, 40, 0.8	44.4

5.3.5 Results and discussion

[A] *Coseismic gravity changes*

Figure 5.3 compares the distribution of coseismic, and short- and long-term postseismic gravity changes of the three megathrust events. Although their signal-to-noise ratio is sometimes low, common gravity change signatures are seen. Coseismic signatures of the three earthquakes (Figure 5.3a, d, g) are dominated by gravity decreases on the upper-plate side of the fault, mainly in the back arc area, with

smaller increases on the incoming-plate side. The latter are often attenuated by the existence of seawater [*Heki and Matsuo*, 2010; *Matsuo and Heki*, 2011]. Such coseismic changes are well explained as the elastic response of the realistic Earth to fault slip as explained in Chapter 4.

[B] ***Short-term postseismic gravity changes***

Figure 5.4 shows that the gravity decreases as the continuation of the coseismic step for a few months, and increases over longer periods. The short-term postseismic gravity changes (Figure 5.3b, e, h) are largely negative and similar to coseismic changes (Figure 5.3a, d, g), although their maxima seem to shift somewhat trenchward. On the other hand, the long-term postseismic gravity changes (Figure 5.3c, f, i) are mostly positive with their maxima residing roughly above the ruptured faults. These features are common in the three earthquakes.

The elastic response to the afterslip should occur as the continuation of the coseismic gravity changes, and their spatial distribution should show some similarity. The time constants (0.14 – 0.25 yr) in the displacement of GNSS stations over the first few postseismic months are consistent with such short-term negative changes, and not with the long-term positive changes (Figure 5.5). These similarities in temporal signatures strongly indicate that the short-term gravity changes are due to afterslips (delayed elasticity by the transient rheology [*Wang K. et al.*, 2012] may contribute to some extent). Afterslip occurs both up-dip and down-dip of the coseismic rupture zone. The trenchward shifts of the centers of the short-term postseismic gravity decreases might reflect the sensitivity contrast, i.e., shallower slips make larger gravity signals. The short-term gravity change of the Maule earthquake is almost as large as the

coseismic change, although the other two earthquakes do not show such peculiarity. This might suggest the role of transient viscoelastic relaxation, but needs future studies.

It should be noted here that the short-term postseismic change of the 2004 Sumatra-Andaman earthquake (Figure 5.3b) might include the signal of the coseismic gravity steps of the 2005 March 28 Nias earthquake (M_w8.6), as shown by a small negative anomaly around (99W, 6S).

Additionally, the existence of the short-term postseismic component in the gravity time series is indicated statistically by AIC verification for the 2004 Sumatra-Andaman earthquake and the 2010 Maule earthquake.

[C] ***Long-term postseismic gravity changes***

The Maxwell viscoelasticity causes the slow convergent movements of lithosphere in subduction zones over years to decades after megathrust earthquakes (see Figure 2 of *Wang L. et al.*, [2012b]). Such a movement would promote gravity increase around the ruptured fault (Figure 5.1).

The "long-term" postseismic gravity change of the 2004 Sumatra-Andaman earthquake has been often explained by such viscous relaxation of the upper mantle [e.g. *Han et al.*, 2008; *Panet et al.*, 2010]. Indeed, the cumulative gravity changes over the two postseismic years calculated assuming a spherically symmetric viscoelastic Earth model (Figure 5.6) [*Tanaka Y.-Y. et al.*, 2006; 2007, and *Tanaka Y.-Y.*, 2013] show striking similarity to Figure 5.3 (c), suggesting its strong potential to explain long-term postseismic gravity changes. However, in order to match the calculation with the observation, we have to assume the upper mantle viscosity (e.g. Figure 5.6 assumes 3×10^{18} Pa s) lower by two orders of magnitude than the global average of $10^{20} – 10^{21}$ Pa

s [*Moucha et al.*, 2007]. In this context, the upward diffusion of supercritical water around the down-dip end of the ruptured fault, as suggested by *Ogawa and Heki* [2007], could help explain some parts of the postseismic gravity recoveries that are too fast to be due to the Maxwell viscoelasticity.

In the top two cases in Figure 5.4, the long-term gravity increases are more than the short-term drops causing net gravity increase just above the faults. However, gravity shows net decrease in the back arc side of trenches. A long-term balance of gravity changes in a whole earthquake cycle is an interesting issue. However, quantitative discussion is premature at the moment because satellite gravimetry has not succeeded in detecting slow gravity changes associated with interseismic strain build-up yet.

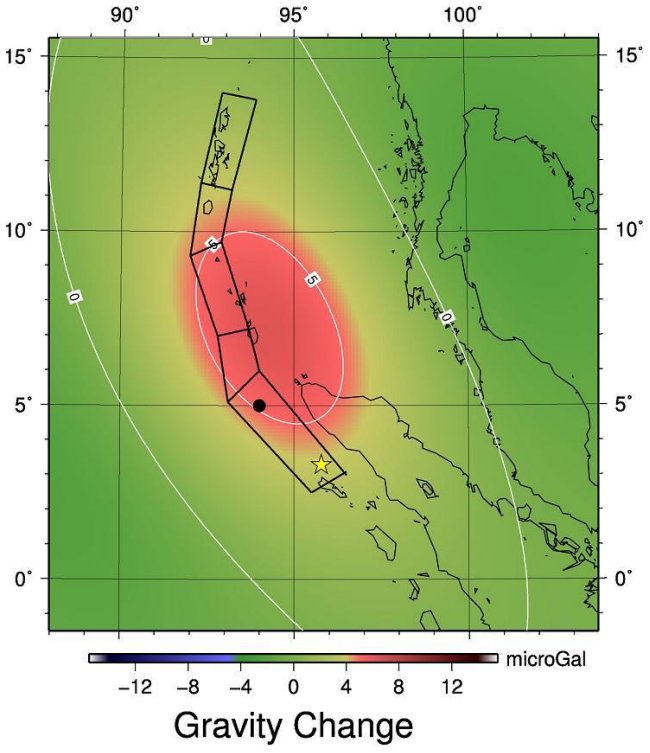

Figure 5.6 Postseismic gravity changes of the 2004 Sumatra-Andaman earthquake due to the viscoelastic mantle relaxation. Figure 3 (middle) in *Tanaka Y.-Y.* [2013] was re-drawn using the upper mantle viscosity of 3×10^{18} Pa s.

5.3.6 Supporting information

Before the conclusion, two pieces of supporting information are added. First, the time series with GLDAS corrections for the three cases are provided in Figure 5.7. Second, the sensitivity of the results to different values of τ_1 in the function (5.2) is shown in Figure 5.8. These two figures show that the overall story is not affected by hydrological noises and little differences of the time constant of the short-term component.

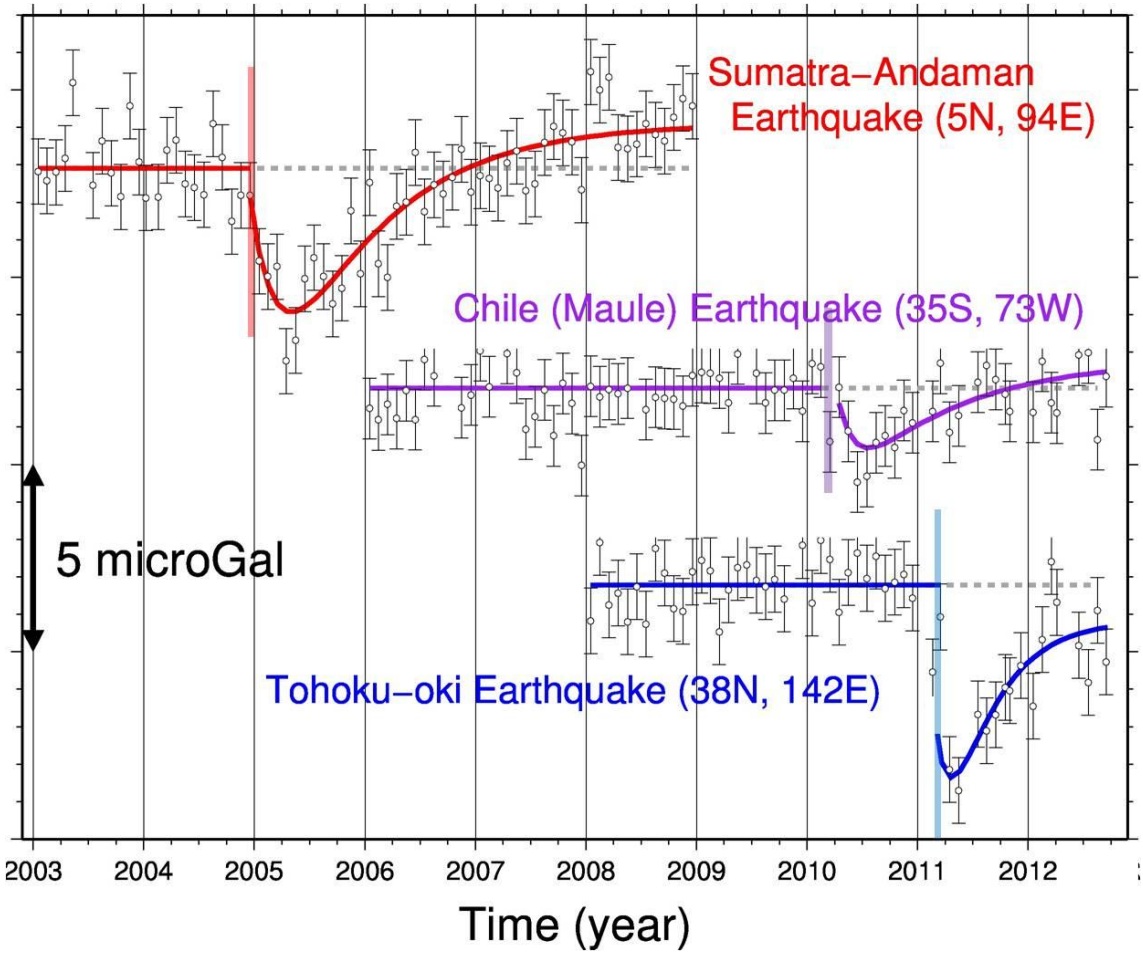

Figure 5.7 Same as Figure 5.4, but the GLDAS/Noah model was used to correct for land hydrological signals. Average seasonal changes and secular trends are removed. There are slight increases of post-fit residuals, but the whole picture remains the same as Figure 3.4.

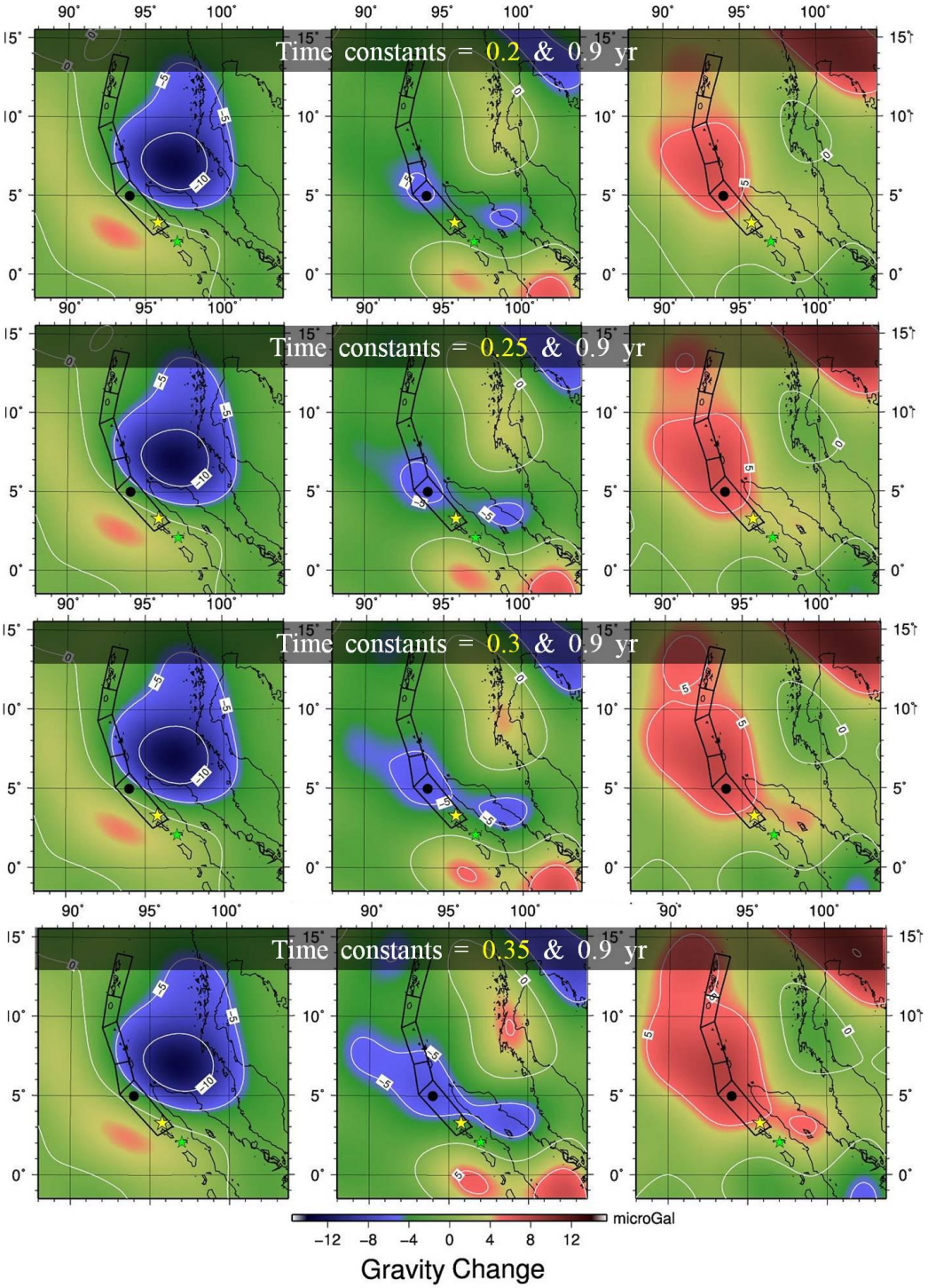

Figure 5.8 Same as Figure 5.3 (a), (b), and (c), but the time constants of the short-term postseismic changes (τ_1) were changed from 0.2 yr to 0.35 yr. Distributions of the changes in the middle and right columns have some sensitivity to τ_1, but remain consistent with the nominal case (τ_1: 0.25 yr).

5.3.7 Conclusions of the section 5.3

Postseismic gravity changes following three M9 class earthquakes had two components, i.e., short- and long-term gravity changes. The coseismic gravity drop is followed by continuing decrease in the first few months, and then gradual increase over years. The physical mechanisms of the short- and long-term postseismic gravity changes would be explained with afterslip (and partly by the transient rheology) and relaxation of Maxwell viscoelastic material (and partly by the movement of supercritical water at depth).

GNSS networks are deployed in many convergent plate boundaries. However, they are on the island/continental arcs with a certain distance from trenches. As shown in *Wang K. et al.* [2012], both afterslip and viscoelastic relaxation cause trenchward movements there, and it is difficult for GNSS receivers to observe the transition from the former to the latter. The satellite gravimetry offers a new sensor to investigate deformation cycles of subduction earthquakes in a unique approach different from conventional sensors (Figure 5.1).

5.4 Other related studies

Han et al. [2008] and *Han et al.* [2014] compared observed and calculated postseismic gravity changes assuming afterslip and viscoelastic relaxation for the 2004 Sumatra-Andaman earthquake and the 2011 Tohoku-Oki earthquake, respectively. *Han et al.* [2014] suggested that afterslip could cause postseismic gravity changes with the same polarity as coseismic gravity changes, which is opposite to *Tanaka and Heki* [2014]. However, the fault slip model for the calculations about afterslip is estimated from GNSS observations for 1.5 years after the 2011 Tohoku-Oki earthquake and they

include contributions of viscoelastic relaxation as well as afterslip. Both of afterslip and viscoelastic relaxation move GNSS stations on the ground trenchward (Figure 5.1), so it is difficult to separate these two mechanisms based on only GNSS observations.

Tobita [2016] analyzed the time series of GNSS station coordinates and reported that they are composed of three components, i.e., (1) a very-short-term component represented by a logarithm with a time constant of a few days, (2) a short-term component represented by an exponential function with a short time constant, and (3) a long-term component represented by another exponential function with a long time constant. *Tobita* [2006] also suggested that the very-short-, short-, and long-term components stem from afterslip, short-term viscoelastic relaxation, and long-term viscoelastic relaxation, respectively. This follows *Hoechner et al.* [2011] and *Sun et al.* [2014], who pointed out that short-term viscoelastic relaxation of Burgers rheology can contribute to short-term postseismic surface movements. Provided that this theory is correct, the short-term postseismic gravity changes observed by the GRACE satellites may reflect both afterslip and short-term viscoelastic relaxation.

Han et al. [2016] discovered that "2006-2007 earthquake doublet", the combination of the 2006 M_w8.3 thrust and 2007 M_w8.1 normal fault earthquakes on the central Kuril Islands caused larger postseismic gravity changes than expected from their magnitudes, fault mechanisms and depths. They considered that the large postseismic gravity changes reflected a unique viscosity structure around the hypocenters and this unique structure drove unexpected large viscoelastic relaxation. They also tried to estimate the viscosity structure there using the gravity change data. This is one of the first attempts to investigate subsurface structures from postseismic gravity changes.

5.5 Conclusions of the Chapter 5

Long-term postseismic gravity changes are considered to stem mainly from viscoelastic relaxation of the upper mantle by comparing the observations and the calculations [e.g. *Tanaka Y. –Y. et al.*, 2015]. However, in these reports, they assumed that the postseismic gravity changes are caused by viscoelastic relaxation and estimated upper mantle viscosity that can reproduce the observation results. Thus, the theory would need to be verified in future by more observations using different approaches.

Postseismic gravity changes also have a short-term component, which governs the gravity changes for a few months immediately after earthquakes. This can be caused by afterslip and short-term viscoelastic relaxation. However, further physical considerations need to be made to confirm they are the unique interpretation.

It is certain that postseismic gravity changes provide more chances to understand physical mechanisms of earthquake cycles on subduction zone from a viewpoint of mass redistribution. Hence, it is necessary to pursue quantitative researches of earthquakes taking time-variable gravity observations into account, for future better understandings of the Earth's subsurface structures, physical properties, and so on.

Chapter 6

Reanalysis of co- and long-term postseismic gravity changes of the 2004 Sumatra-Andaman earthquake with the latest GRACE data

6.1 Introduction

The 2004 Sumatra-Andaman earthquake (M_w9.2) is the first M_w9 class earthquake after the launch of the GRACE satellites in 2002, and is still the biggest earthquake observed by the GRACE satellites. Here, I show results of time series analysis about the co- and postseismic gravity changes of the 2004 Sumatra-Andaman earthquake from Jan 2003 to July 2016 based on the latest GRACE data.

6.2 Latest GRACE data from UTCSR

I analyzed the time series with the latest GRACE data provided by UTCSR as the spherical harmonics coefficients with degrees and orders up to 60 with the function (2.13) with the term $P(t - t_{eq})$ expressed using double exponential functions with the time constants of 0.25 and 2.8 years. The Fan filter of 250 km averaging radius and the

de-striping filter with a cubic function to degrees and orders of 15 and more are applied for the analysis of the downward components of the gravity field. For the analysis of the northward component, however, only the Fan filter is applied (The details are provided in the Chapter 2). The vertical and northward gravity changes related to the earthquake are shown in Figures 6.1 and 6.2, respectively. In these figures, the distributions of co- and short- and long-term postseismic gravity changes are indicated as (a), (b), and (c), respectively. The total co- and postseismic gravity changes are shown in (d).

Figures 6.1a and 6.2a appear different but they reflect the same origin of mass re-distribution. When the downward components of the gravity become strong (weak) above one point, the "north-to-south" spatial pattern of the northward components around the point becomes "weak-to-strong" (strong-to-weak). Thus, when the north-to-south spatial pattern of the downward components is weak-to-strong, that of the northward components should be "strong-weak-strong" (Figure 6.3). The difference between Figures 6.1b-d and 6.2b-d can be explained as well. For example, the Figure 6.1c shows that the downward components of the gravity become stronger along the fault and Figure 6.2c shows that the northward components become weaker and stronger on the north and south sides of the fault, respectively. They are completely matched to Figure 6.3 (left).

Additionally, the "upward gradient of the vertical component of the gravity field" changes are analyzed by using the function (2.3) with the same Fan and de-striping filters. The results are shown in the Figure 6.4. *Wang L. et al.* [2012a] suggests that the gravity gradient changes have better sensitivity to short-wave components and they are useful to get better spatial resolution of coseismic gravity changes. However, it is also suggested in the same report that the GRACE observation cannot recover the

amplitudes of gravity gradient changes as accurately as the gravity changes. Hence, the gravity gradient changes from GRACE should be used to as the secondary observable to support other information.

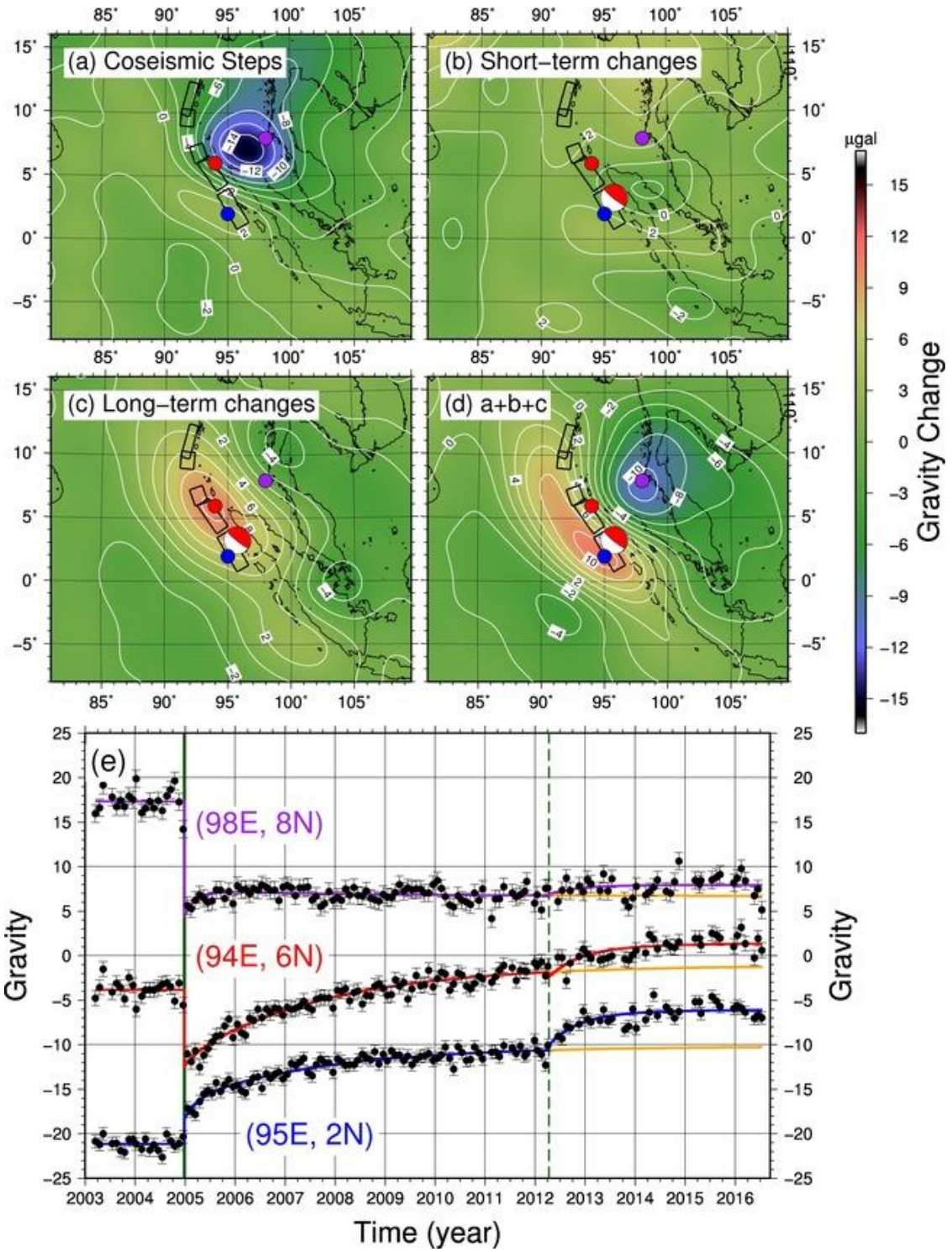

Figure 6.1 The distributions of co- (a) and short-term (b) and long-term (c) postseismic gravity (down component) changes of the 2004 Sumatra-Andaman earthquake, (d) the map showing the total co- and postseismic gravity changes, and (e) the gravity time series at three points indicated as blue, red, and purple circles in (a-d). The average seasonal changes have been removed. The contour intervals are 2μGal. The focal

mechanisms are shown at the epicenter of the earthquake. The black rectangles under beach balls show the segments of the faults ruptured in this earthquake. The time constants of double exponential functions for the time series after the 2004 Sumatra-Andaman earthquake and single exponential function after the 2012 Indian-Ocean earthquake are 0.25, 2.8, and 0.6 years, respectively. In (e), the black circles show monthly gravity data, the blue, red, and purple curves are the estimated models, and the orange curves represents the postseismic gravity changes after removing the contributions of the 2012 Indian-Ocean earthquake. Error bars represent the root-mean-square error inferred from post-fit residuals. The solid and dashed vertical dark green lines indicate the 2004 Sumatra-Andaman earthquake and the 2012 Indian-Ocean earthquake occurrences, respectively.

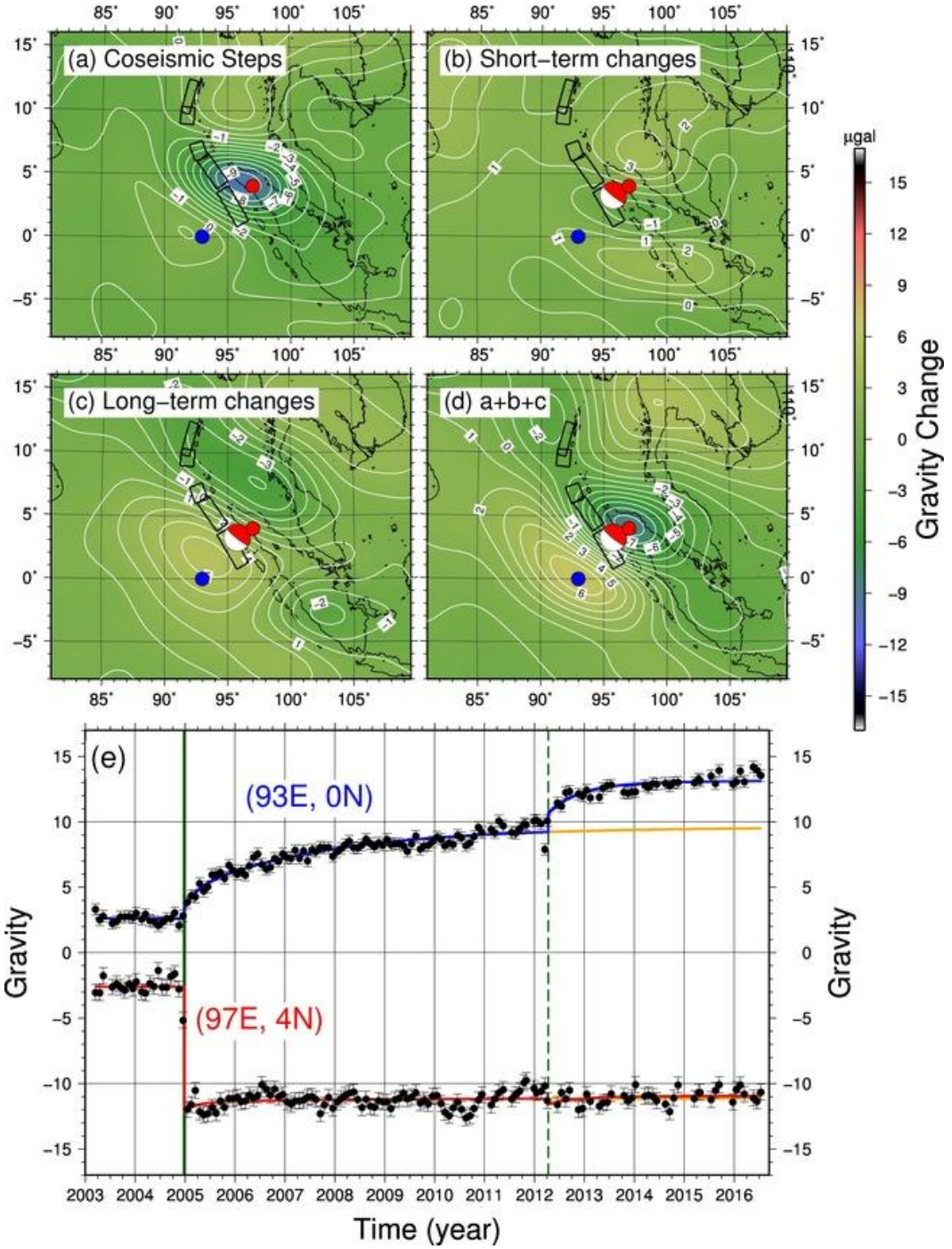

Figure 6.2 The same figure as Figure 6.1 except the following five points: (1) the north components of the gravity field are shown, (2) The de-striping filter is not applied (only the Fan filter with averaging radius 250 km is applied), (3) time series represent two new points shown with blue and red circles in (a-d), (4) the beach balls in (a) and (d) are removed to show the distribution clearly, and (5) contour intervals are 1 μGal.

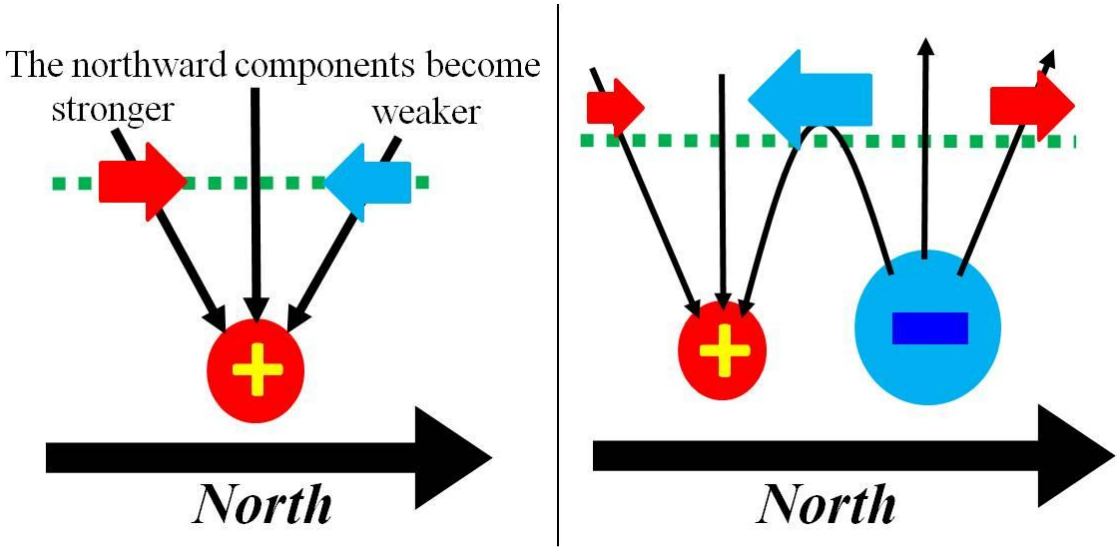

Figure 6.3 The schematic image of the relationship between downward and northward gravity changes. [Left] When the downward components of the gravity become strong (weak) above a certain point, the north-to-south spatial pattern of the northward components around the point becomes “weak-to-strong” (strong-to-weak). [Right] Thus, when the north-to-south spatial pattern of downward components is “weak-to-strong”, that of northward components is “strong-weak-strong”.

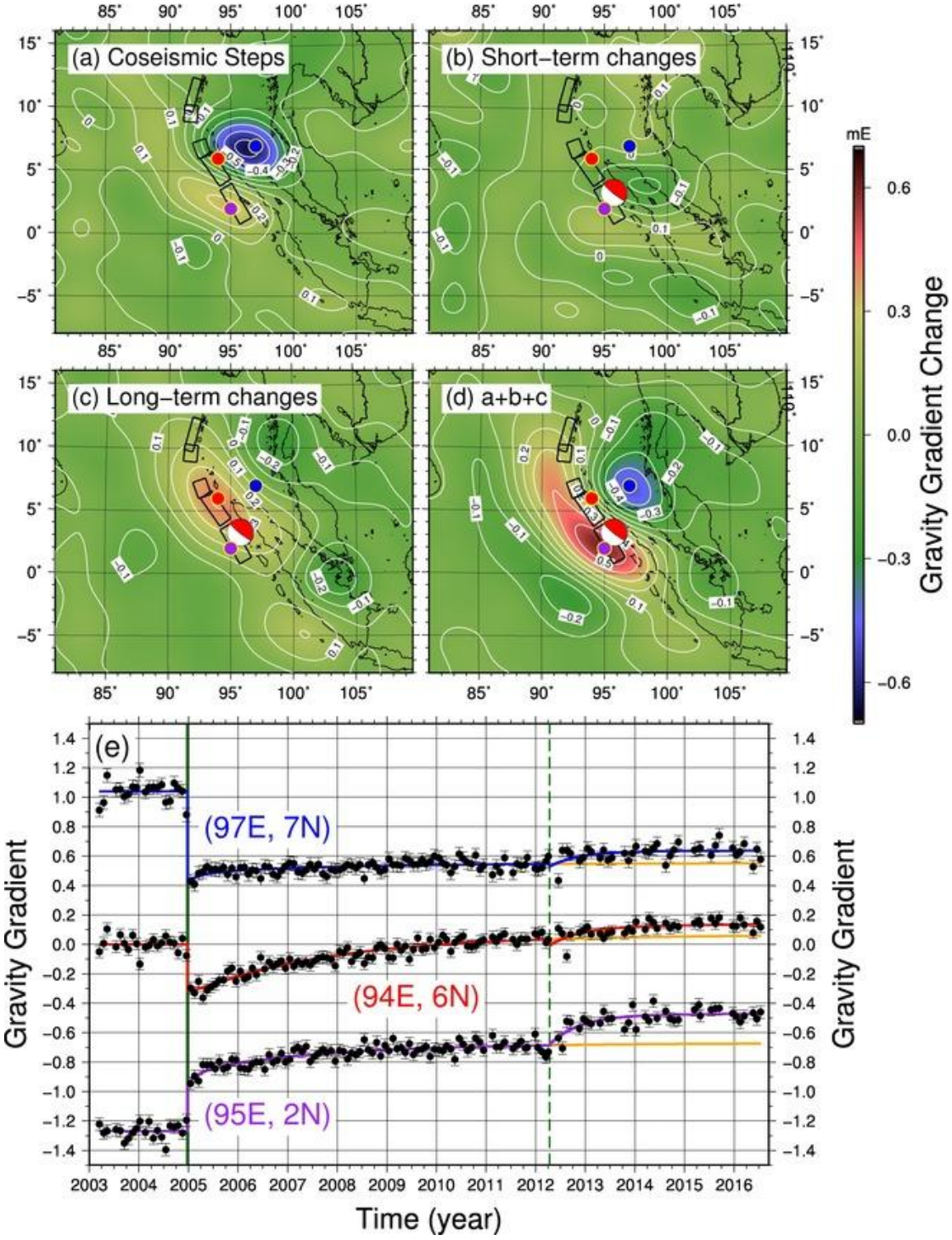

Figure 6.4 The same figure as Figure 6.1 except the following five points: (1) the changes in the upward gradient of the vertical component of the gravity field are shown, (2) the unit is mE (mili-Eötvös; 1 E = 10^{-9} Gal/cm = 10^{-9}/s^2), (3) time series represent new points are shown (blue, red and purple circles in the maps), (4) contour intervals are 0.1 mE, and (5) the color scale is different.

6.3 Latest GRACE data from CNES/GRGS

The Centre National d'Etudes Spatiales/Groupe de Recherches de Géodésie Spatiale (CNES/GRGS), one of unofficial analysis centers of the GRACE data, provides Level-2 data, with degrees and orders complete to 80, after stripe and short-wavelength noises are removed. The data can be downloaded through their website (http://grgs.obs-mip.fr/en).

The results based on the data by CNES/GRGS are shown in the Figures 6.5, 6.6, and 6.7. They are the same as those in the section 6.2 except the source of the data and the highest degree/order of the coefficients (80). The amplitudes of the gravity (and the gravity gradient) changes appear somewhat larger. The spatial resolution is higher than those by UTCSR reflecting higher maximum degree and order used to plot the figures. However, the basic spatial patterns are quite similar.

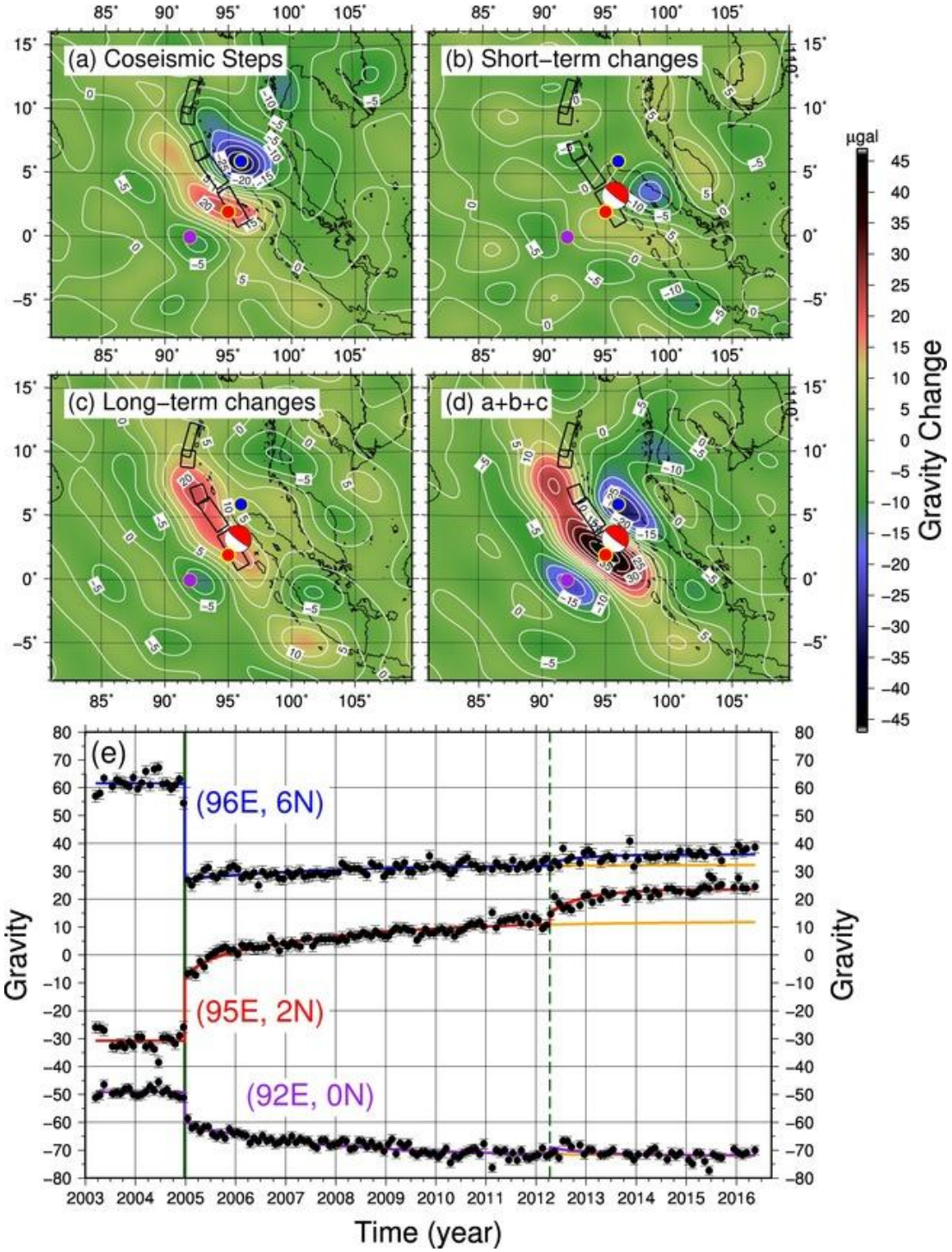

Figure 6.5 The same figure as Figure 6.1 apart from the following four points: (1) we used the coefficients with degrees and orders complete to 80 from CNES/GRGS, (2) The de-striping and Fan filters are not applied by myself, (3) time series reflect gravity changes at new points shown in the map as blue, red and purple circles, and (4) contour intervals are 5 μGal.

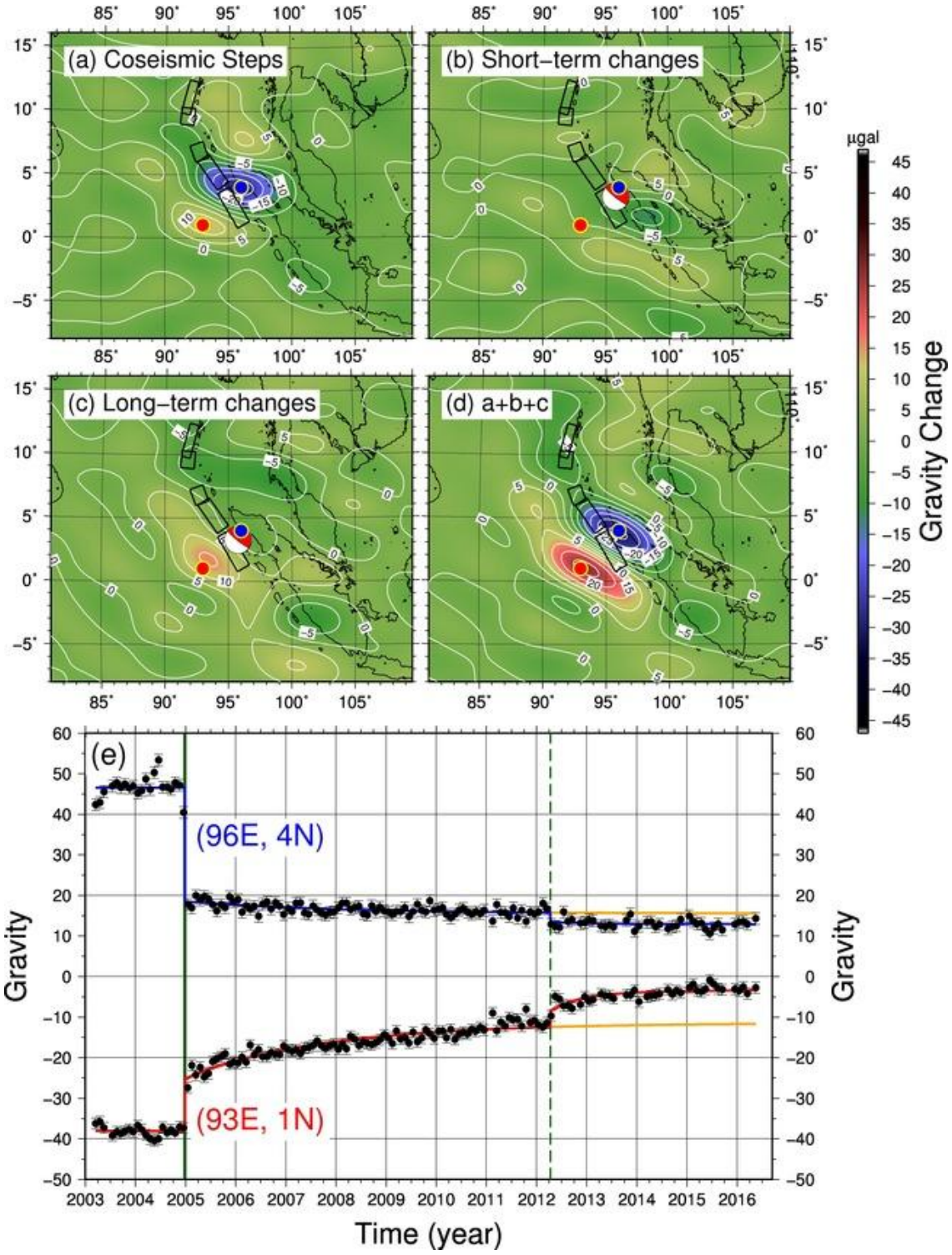

Figure 6.6 The same figure as Figure 6.5 except the following three points: (1) the northward components are shown, (2) time series represent different points (see circles on the map), (3) the beach balls in (a) and (d) are removed for the visual clearity.

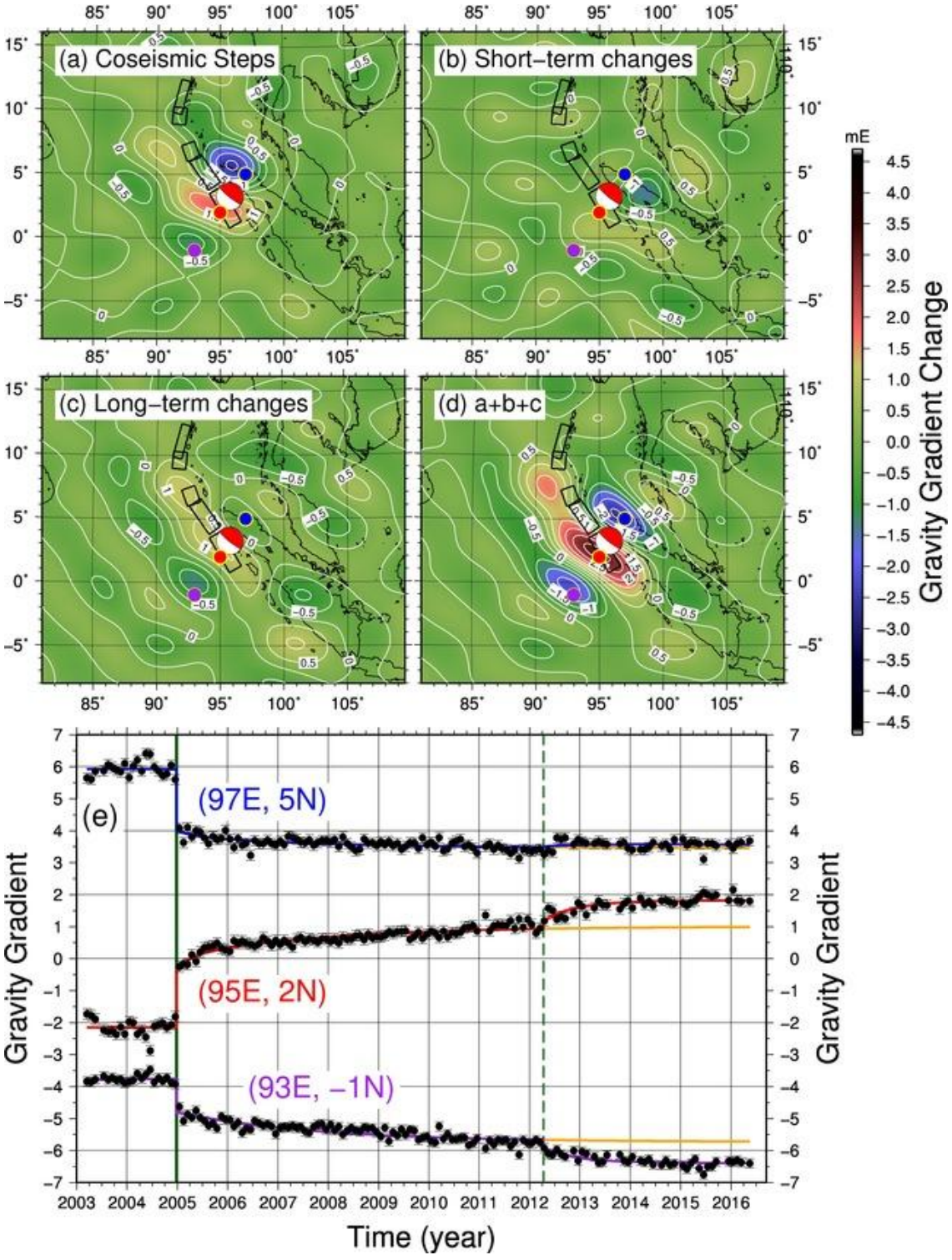

Figure 6.7 The same figure as Figure 6.5 except the following five points: (1) I plot the changes in the upward spatial gradient of the vertical component of the gravity field, (2) the unit is mE, (3) time series are shown for points shown on the map, (4) contour intervals are 0.5 mE, and (5) the color scale is different.

6.4 Discussions and conclusions of Chapter 6

Both of the time series analyses using the data from UTCSR and CNES/GRGS gave almost same results except for the differences in the signal amplitudes and spatial resolutions coming from the differences of maximum degree and order, 60 and 80, respectively.

The coseismic gravity changes in the down and north components show consistent spatial patterns (Figures 6.1 - 6.3 and 6.5 - 6.6). They are similar to those of the 2011 Tohoku-Oki earthquake (Figure 4.3), which are explained sufficiently by the numerically calculated coseismic gravity changes (Figures 4.1 and 4.8). Coseismic gravity gradient changes look similar to coseismic downward gravity changes (Figures 6.1 and 6.4). The gradient changes have larger sensitivities to shortwave components, but they are more difficult to recover using the GRACE data than gravity changes [*Wang L. et al.*, 2012a], so the gradient changes should be used as secondary information to support results from the gravity changes.

Further studies about postseismic gravity changes are necessary to understand various postseismic phenomena in order to reveal physical processes governing earthquake cycles in subduction zones. The GNSS observations can also be used for this purpose with even higher temporal and spatial resolutions. However, the GNSS stations are located mainly on land, and afterslip and viscoelastic relaxation are often difficult to distinguish from the surface velocity data with limited spatial coverage (i.e. island arcs tend to move in the same direction). After all, the GRACE observations have two advantages, i.e., the same sensitivity to both land and ocean areas, and the different polarities of short- and long-term postseismic gravity changes.

The gravity time series shown in Figures 6.1 - 6.7c (except 6.4) indicate that the

postseismic gravity trend is approaching zero. This suggests that the long-term postseismic gravity changes of the 2004 Sumatra-Andaman earthquake is almost over up to now. This would provide useful information on the upper mantle viscosity because the dominant mechanism for the long-term postseismic gravity changes is viscoelastic relaxation in the upper mantle.

The spatial patterns of the sum of the co- and postseismic gravity changes, together with those of the static gravity anomalies (Figure 6.8), may give some insight into the interseismic gravity changes. The static gravity anomaly is formed by the repetition of the cycles of inter-, co-, and postseismic gravity changes. In the sum of co- and postseismic gravity changes (Figure 6.5d), the gravity decreased in the Sumatra Island, increased around the trench, and decreased on the outer rise side. This is roughly opposite to the static gravity anomaly (Figure 6.8). This can mean that the interseismic gravity changes would urge the static gravity anomaly grow while interplate thrust earthquakes (sum of co- and postseismic gravity changes) would partly reduce it. Based on this speculation, the static gravity anomaly could be the integration of the surplus of interseismic gravity changes not cancelled by co- and postseismic gravity changes of lots of different earthquakes.

In any case, the postseismic gravity changes of the 2004 Sumatra-Andaman earthquake are almost over, and the present static gravity anomaly must have been formed by the repetition of earthquake cycles over a geological timescale. Hence, this earthquake presents, for the first time, a clue to understand the growth of the static gravity anomalies through accumulations of co-, post- and interseismic gravity changes over numerous earthquake cycles.

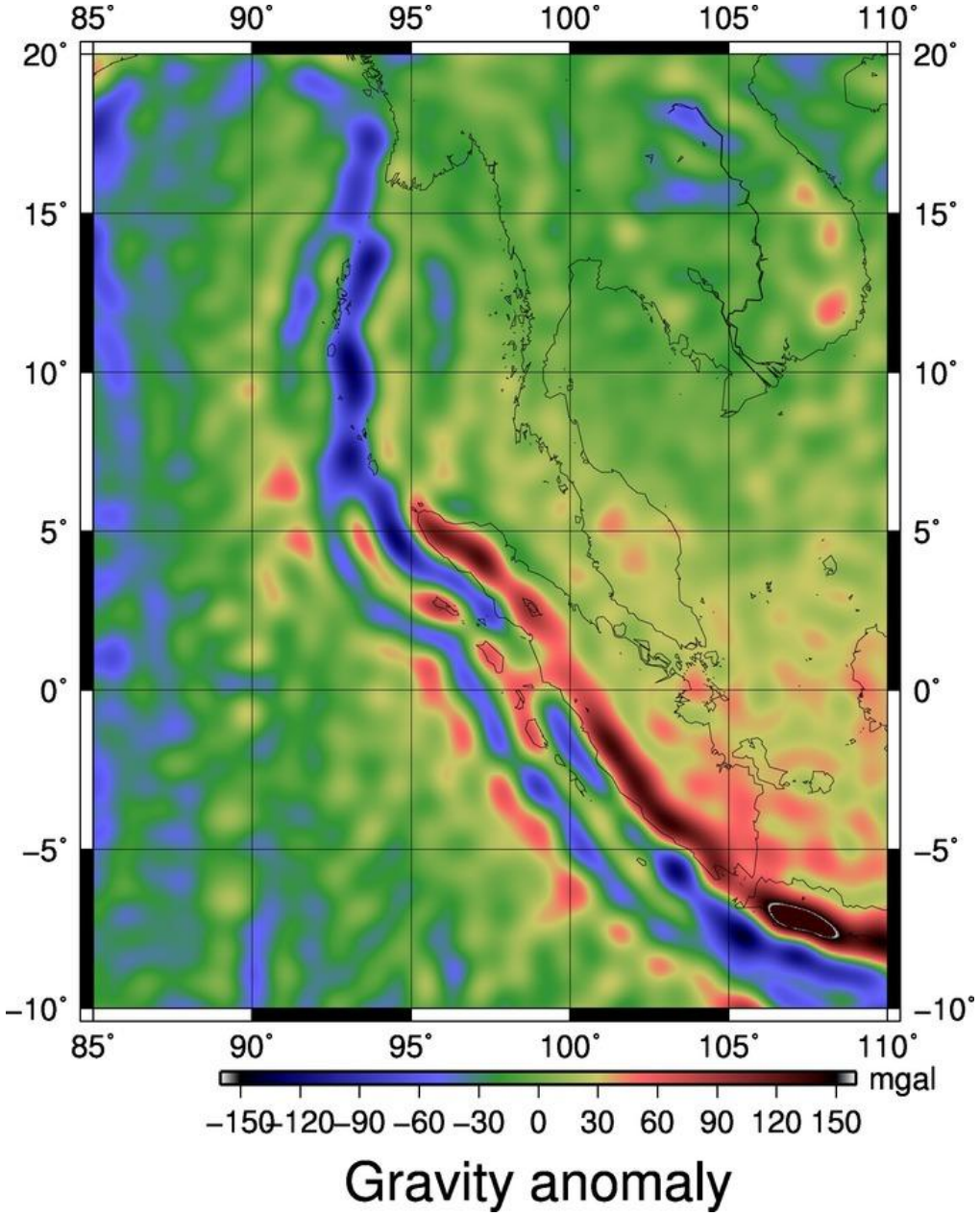

Figure 6.8 The static gravity anomalies around the faults of the 2004 Sumatra-Andaman earthquake. For the detail of the figure, see the caption of Figure 1.7.

Chapter 7

Summary

The GRACE satellites launched in 2002 enabled us to study earthquakes using the two-dimensional and continuous observations of the Earth's gravity fields. Earthquakes change gravity field through mass redistributions associated with fault dislocations. Time-variable gravity would provide unique information on earthquakes from variety of viewpoints.

In this study, I try to reveal physical processes in the earthquakes cycles of subduction zones through gravity changes. Here I discussed gravity changes caused by several large earthquakes that occurred after the GRACE launch in 2002, i.e., the 2004 Sumatra-Andaman earthquake, the 2010 Maule earthquake, the 2011 Tohoku-Oki earthquake, the 2012 Indian-Ocean earthquake, and the 2013 Okhotsk deep-focus earthquake.

In this study, I used the Stokes' coefficients with degrees and orders complete to 60 provided by the Level-2 RL05 GRACE data by UTCSR. After applying the Fan and de-striping filters, I calculated gravity fields at grid points over the Earth's surface, and analyzed the gravity time series at these points. The function for the least square

analysis consists of an offset, a secular trend, annual and semiannual components representing seasonal changes, a step function representing coseismic gravity changes, and various functions to model postseismic gravity changes. The GLDAS models are used to reduce land hydrological contributions in several cases.

I showed several examples of gravity changes of non-earthquake origins, and compared them with the gravity changes by earthquakes. For example, land hydrology is one of the fundamental targets of the GRACE satellites. The signals of seasonal changes of soil moistures, secular decrease caused by ice loss and artificial depletion of groundwater often appear clearly as gravity changes. Glacial Isostatic Adjustments are also observed as secular gravity increase by the GRACE satellites.

Coseismic gravity changes are caused by the following three mechanisms: (1) uplift/subsidence of the boundaries with density contrast (solid earth's surface and Moho), (2) density changes by dilatation and compression in the crust or mantle, and (3) sea water movements by vertical deformation of the sea floor. The theoretical models for coseismic gravity changes have been examined repeatedly by comparing with the gravity changes observed by GRACE. In addition to them, horizontal movements of the terrane with significant slopes are equivalent to vertical deformation, and may contribute to coseismic gravity changes. However, its contribution to the gravity changes are usually smaller than those by (1) – (3).

Three types of the spatial patterns of the downward components of coseismic gravity (G_r) changes have been found so far. First one comes from shallow megathrust earthquakes such as the 2004 Sumatra-Andaman earthquake, the 2010 Maule earthquake, and the 2011 Tohoku-Oki earthquake. They are characterized by dominant gravity decrease at the back arc sides and smaller gravity increase at the trench side.

Second one is caused by large shallow strike-slip earthquakes like the 2012 Indian-Ocean earthquake. The signals consist of symmetric four peaks (two negative and two positive peaks) of gravity changes. The last one is found for deep-focus earthquakes such as the 2013 Okhotsk earthquake (down-dip compression mechanism), showing widely-separated two peaks of gravity changes with different polarities. The differences among these three types simply reflect the difference in fault geometry and depths, and remain within the framework of (1) – (3).

These three types are explained as follows. As for the first type, the shallow thrust earthquakes cause vertical deformations of the surface. Because the distance between the uplift peaks and the subsidence peaks are much shorter than the spatial resolutions of GRACE, they do not contribute much to the gravity changes. However, compressions and dilatations beneath the ground are distributed along near-vertical lines, and they change the gravity field over regions large enough to be observed by GRACE. In the second type, shallow-focus strike-slip fault earthquakes cause pairs of density changes (dilatation and compression) and vertical deformations (subsidence and uplift) around the two ends of the faults. They make gravity changes, so the spatial pattern of coseismic gravity changes by such earthquakes have symmetric 2 x 2 peaks. The third type emerges after deep-focus earthquakes. In these earthquakes, two pairs of compressions and dilatations occur at the both ends of the fault buried at depth. Their signals, made by two pairs of positive and negative mass anomalies, decay more rapidly with distance and contribute little to the gravity changes at the altitude of the GRACE satellites. At the same time, the two peaks of vertical deformations are separated sufficiently so that the GRACE satellites can resolve them. Hence, all of the three types of the spatial patterns of coseismic gravity changes just reflect the difference in the

geometry and the depth of the fault.

Additionally, I found that the results of time series analysis for northward components of the gravity changes (G_θ) and upward components of downward gravity gradient changes (G_{rr}) are also well explained by the same models as the downward components of coseismic gravity changes. The data provided by another data analysis center (CNES/GRGS) were examined and found to give similar results to the CSR data set.

The observations of coseismic gravity changes are moving up to the next stage from just verifying the pre-existing theory to, for example, reinforcing the estimations of coseismic fault slip models by combining with data from other sensors, such as GNSS, seismometer, and SAR. A large benefit of GRACE, in comparison with such conventional sensors, is that we can observe coseismic gravity changes over the land and ocean with uniform accuracy.

On the other hand, physical processes responsible for "postseismic" gravity changes have not been understood sufficiently. I found that postseismic gravity changes after megathrust earthquakes have both short- and long-term components with different polarities. I hypothesized that they stem from afterslip and viscoelastic relaxation, respectively. The time constants of short-term postseismic gravity changes of the 2010 Maule earthquake and the 2011 Tohoku-Oki earthquake are very similar to those of surface deformations observed by GNSS. This supports the hypothesis that the short-term component represents afterslip, although there might be a certain contribution from the delayed elasticity (the Burgers rheology). Long-term postseismic gravity changes are often attributed to the viscoelastic relaxation of the upper mantle. However, in these studies, viscosities of the upper mantle are tuned so that they

reproduce the observed gravity changes. This means that the hypothesis is yet to be verified by external evidences. In order to understand geophysical processes over entire earthquake cycles, uniform accuracy of GRACE both on land and ocean is important. Among others, different polarities of short- and long-term postseismic gravity changes would provide a key in understanding them.

Last but not least, the postseismic gravity changes of the 2004 Sumatra-Andaman earthquake seem to have almost ended by now. This will allow us to constrain the time constant of the postseismic gravity changes, and it will provide a new insight into the viscosity structures of the upper mantle. Moreover, this enables us to start discussions on interseismic gravity changes that contribute to build-up of the static gravity anomaly field by repeating the cycles of interseismic, coseismic, and postseismic gravity changes. As the first approximation, the static gravity anomaly seems to be explained as the accumulation of the excess interseismic gravity changes that failed to be cancelled by co- and postseismic gravity changes.

In 2017, the GRACE-FO (Follow-On) satellites are going to be launched. In addition to conventional inter-satellite ranging with microwaves, they plan to test the measurement inter-satellite distances using laser techniques. Higher accuracy of the GRACE-FO and extended observation periods would further improve our knowledge on gravity changes associated with earthquakes, especially on the longer-term gravity changes over subduction zone earthquake cycles.

References

Akaike, H., 1974, A new look at the statistical model identification, IEEE Transactions on Automatic Control, **19-6**, 716-723, doi: 10.1109/TAC.1974.1100705

Aus der Beek, T., F. Voß, and M. Flörke, 2011, Modelling the impact of Global Change on the hydrological system of the Aral Sea basin, Phys. Chem. Earth, **36**, 684-694

Barnes, D. F., 1966, Gravity changes during the Alaska earthquake, J. Geophys. Res., **71**, 451-456

Cambiotti, G. and R. Sabadini, 2012, A source model for the great 2011 Tohoku earthquake (M_w=9.1) from inversion of GRACE gravity data, Earth and Planetary Sci. Lett., **335-336**, 72-79, doi:10.1016/j.epsl.2012.05.002

Cambiotti, G. and R. Sabadini, 2013, Gravitational seismology retrieving Centroid-Moment-Tensor solution of the 2011 Tohoku earthquake, J. Geophys. Res., **118**, 183-194

Chao, B. F., 2016, Caveats on the equivalent water thickness and surface mascon solutions derived from the GRACE satellite-observed time-variable gravity, Journal of Geodesy, **90**, Issue 9, 807-813, doi:10.1007/s00190-016-0912-y

Chen, J. L., C. R. Wilson, B. D. Tapley, and S. Grand, 2007, GRACE detects coseismic and postseismic deformation from the Sumatra-Andaman earthquake, Geophys. Res. Lett., **34**. L13302, doi:10.1029/2007GL030356.

Cheng, M. and B. D. Tapley, 2004: Variations in the Earth's oblateness during the past 28 years, J. Geophys. Res., **109**, B09402, doi:10.1029/2004JB003028.

Cheng, M. and J. Ries, 2014, Monthly estimates of C_{20} from 5 SLR satellites based on GRACE RL05 models, GRACE Technical Note 07, Center for Space Research. [Available at ftp://podaac.jpl.nasa.gov/allData/grace/docs/TN-07_C20_SLR.txt.]

Cox, C. M. and B. F. Chao, 2002, Detection of a large-scale mass redistribution in the terrestrial system since 1998, Science, **297**, 831-833, 2002.

Dai, C., C. K. Shum, J. Guo, K. Shang, B. Tapley, and R. Wang, 2016, Improved source parameter constraints for five undersea earthquakes from north component of GRACE gravity and gravity gradient change measurements, Earth and Planetary Science Letters, **443**, 118-128, doi;10.1016/j.epsl.2016.03.025

Döll, P., F. Kaspar, and J. Alcamo, 1999, Computation of global water availability and water use at the scale of large drainage basins, Mathematische Geologie, **4**, 111-118

Fuchs, M. J., J. Bouman, T. Broerse, P. Visser, and B. Vermeersen, 2013, Observing coseismic gravity change from the Japan Tohoku-Oki 2011 earthquake with GOCE gravity gradiometry, J. Geophys. Res., **118**, 5712-5721, doi:10.1002/jgrb.50381

Fuchs, M. J., A. Hooper, T. Broerse, and J. Bouman, 2016, Distributed fault slip model for the 2011 Tohoku-Oki earthquake from GNSS and GRACE/GOCE satellite gravimetry, J. Geophys. Res., **121**, 1114-1130, doi:10.1002/2015JB012165

Garcia, R. F., S. Bruinsma, P. Lognonné, E. Doornbos, and F. Cachoux, 2013, GOCE: The first seismometer in orbit around the Earth, Geophys. Res. Lett., **40**, 1015–1020, doi:10.1002/grl.50205

Han, S. C., Shum C. K., M. Bevis, C. Ji, and C. Y. Kuo, 2006, Crustal Dilatation Observed by GRACE After the 2004 Sumatra-Andaman Earthquake, Science, **313**, 658-662, doi:10.1126/science.112866

Han, S. C., J. Sauber, S. B. Luthcke, C. Ji, and F. F. Pollitz, 2008, Implications of postseismic gravity change following the great 2004 Sumatra-Andaman earthquake from regional harmonic analysis of GRACE intersatellite tracking data, J. Geophys. Res., **113**, doi:10.1029/2008JB005705

Han, S. C., J. Sauber, and S. Luthcke, 2010, Regional gravity decrease after the 2010 Maule (Chile) earthquake indicates large-scale mass redistribution, Geophys. Res. Lett., **37**, doi:10.1029/2010GL045449

Han, S. C., J. Sauber, and R. Riva, 2011, Contribution of satellite gravimetry to understanding seismic source processes of the 2011 Tohoku-Oki earthquake, Geophys. Res. Lett., **38**, doi:10.1029/2011GL049975

Han, S. C., R. Riva, J. Sauber, and E. Okal, 2013, Source parameter inversion for recent great earthquakes from a decade-long observation of global gravity fields, J. Geophys. Res., **118**, 1240-1267, doi:10.1002/jgrb.50116

Han, S. C., J. Sauber, and F. Pollitz, 2014, Broad scale postseismic gravity change following the 2011 Tohoku-Oki earthquake and implication for deformation by viscoelastic relaxation and afterslip, Geophys. Res. Lett., **41**, 5797-5805, doi:10.1002/2014GL060905

Han, S. C., J. Sauber, and F. Pollitz, 2015, Coseismic compression/dilatation and viscoelastic uplift/subsidence following the 2012 Indian Ocean earthquakes quantified from satellite gravity observations, Geophys. Res. Lett., **42**, 3764-3772, doi:10.1002/2015GL063819

Han, S. C., J. Sauber, and F. Pollitz, 2016, Postseismic gravity change after the 2006-2007 great earthquake doublet and constraints on the asthenosphere structure in the central Kuril Islands, Gophys. Res. Lett., **43**, 3169-3177, doi:10.1002/2016GL068167

Harig, C. and Simons F. J., 2012, Ice mass loss in Greenland, the Gulf of Alaska, and the Canadian Archipelago: Seasonal cycles and decadal trends Geophys. Res. Lett., **43(7)**, 3150-3159, doi:10.1002/2016GL067759

Harig, C. and Simons F. J., 2015, Accelerated West Antarctic mass loss continues to outpace East Antarctic gains, Earth and Planetary Science Letters, **415**, 134-141

Harms, J., 2016, Transient gravity perturbations from a double-couple in a homogeneous, Geophys. J. Int., **205**, 1153-1164, doi:10.1093/gji/ggw076

Heki, K. and K. Matsuo, 2010, Coseismic gravity changes of the 2010 earthquake in central Chile from satellite gravimetry, Geophys. Res. Lett., **37**, doi:10.1029/2010GL045335

Heiskanen, W. and H. Moritz, 1967, Physical Geodesy

Hoechner, A., S. V. Sobolev, I. Einarsson, and R. Wang, 2011, Invesigation on afterslip and steady state and transient rheology based on postseismic deformation and geoid change caused by the Sumatra 2004 earthquake, Geochemistry Geophysics Geosystems, **12**, doi:10.1029/2010GC003450

Hu, Y., K. Wang, J. He, K. Klotz, and G. Khazaradze, 2004, Three-dimensional viscoelastic finite element model for postseismic deformation of the great 1960 Chile earthquake, J. Geophys. Res., **109**, doi:10.1029/2004/JB003163

飯田汲事・早川正巳・片寄邦之, 1951, 1950 ~ 1951 年の三原山活動時における重力測定, 地学雑誌, **60(3),** 133-136, doi:10.5026/jgeography.60.133

Imanishi, Y., T. Sato, T. Higashi, W. Sun, and S. Okubo, 2004, A network of superconducting gravimeters detects submicrogal coseismic gravity changes, Science, **306**, 476-478, doi:10.1126/science.1101875

Jacob, T., J. Wahr, W.T. Preffer and S. Swenson, 2012, Recent contributions of glaciers and ice caps to sea level rise, Nature, **482**, 514-518, doi:10.1038/nature10847

Kaula 1966, Theory of satellite geodesy: Applications of satellites to geodesy

Kikuchi, M. and H. Kanamori, 1994, The mechanism of the deep Bolivia earthquake of June 9, 1994, Geophys. Res. Lett., **21**, 2341–2344, doi:10.1029/94GL02483

Lewis, S., L., P. M. Brando, O. L. Phillips, G. M. F. van der Heijden, and D. Nepstad, 2011, The 2010 Amazon drought, Science, **331**, doi:10.1126/science.1200807

Li, J., J. L. Chen, and C. R. Wilson, 2016, Topographic effects on coseismic gravity change for the 2011 Tohoku-Oki earthquake and comparison with GRACE, J. Geophys. Res., **121**, Issue 7, 5509 – 5537.

Matsuo, K. and K. Heki, 2011, Coseismic gravity changes of the 2011 Tohoku-Oki earthquake from satellite gravimetry, Geophys. Res. Lett., **38**, doi:10.1029/2011GL049018

Matsuo. K, 2013, Large scale mass transportations on the Earth from satellite gravimetry: Climate changes and earthquakes, http://www.ep.sci.hokudai.ac.jp/~geodesy/pdf/Matsuo_Dsc_Thesis.pdf

Matsuo, K., B. F. Chao, T. Otsubo, and K. Heki, Accelerated ice mass depletion revealed by low-degree gravity field from Satellite Laser Ranging: Greenland, 1991-2011, Geophys. Res. Lett., **40**, 1-6, doi:10.1002/grl.50900, 2013.

Matsuo, K. and K. Heki, 2014, Glacier mass balance in Asian high mountains: Reconsideration of satellite gravimetry estimates, SEPPYO, **76(1)**, 45-57 (in Japanese).

Montagner, J.-P., et al., 2016, Pronmpt gravity signal induced by the 2011 Tohoku-Oki earthquake, nature COMMUNICATIONS, **7,** doi:10.1038/ncomms13349

Moucha, R., A. Forte, J. X. Mitrovica, and A. Daradich, 2007, Lateral variations in mantle rheology: implications for convention related surface observables and inferred viscosity models, Geophys. J. Int., **169**, 113-135, doi:10.1111/j.1365-246X.2006.03225.x.

Munekane, H., 2013, The Satellite Gravimetry Mission GRACE from Below, Journal of the Geodetic Society of Japan, **59(3)**, 111-118 (in Japanese)

Nerem, R. S., Chao, B. F., Au, A. Y., Chan, J. C., Klosko, S. M., Pavlis, N. K., and Williamson, R. G., 1993: Temporal variations of the Earth's gravitational field from satellite laser ranging to Lageos. Geophys. Res. Lett., **20**, 595-598.

Nishimura, T., T. Matsuzawa, and K. Obara, 2013, Detection of short-term slow slip events along the Nankai Trough, southwest Japan, using GNSS data, J. Geophys. Res. Solid Earth, **118**, 3112-3125, doi:10.1002/jgrb.50222.

Okada, Y., 1992, Internal deformation due to shear and tensile faults in a half-space, Bull. Seismol. Soc. Am., **82**, 1018–1040.

Okubo, S., 1992, Gravity changes due to shear and tensile faults in a half-space, J. Geophys. Res., **97**, 7137-7144, doi:10.1029/92JB00178

Panet, I., V. Mikhailov, M. Diament, F. Pollitz, G. King, O. de Viron, M. Holschneider, R. Biancale, and J. M. Lemoine, 2007, Coseismic and post-seismic signatures of the Sumatra 2004 December and 2005 March earthquakes in GRACE satellite gravity, Geophys. J. Int., **171**, 177–190, doi:10.1111/j.1365-246X.2007.03525.x.

Peltier, W. R., 1974, The impulse response of a Maxwell Earth, Rev. Geophys. Space. Phys., **12**, 649-669

Pollitz, F. F., 1992, Postseismic relaxation theory on the spherical earth, Bull. Seism. Soc. Am., **82**, 422-453

Pollitz, F. F., 1997, Gravitational viscoelastic postseismic relaxation on a layered spherical Earth, J. Geophys. Res., **102**, 17921-17941, doi:10.1029/97JB01277

Pollitz, F. F., 2003, Postseismic relaxation theory on a laterally heterogeneous viscoelastic model, Geophys. J. Int., **155**, 57-78

Pollitz, F. F., R. Bürgmann, and P. Banerjee, 2006, Post-seismic relaxation following the great 2004 Sumatra-Andaman earthquake on a compressible self-gravitating Earth, Geophys. J. Int., **167**, 397-420

Rodell, M., et al., 2004, The Global Land Data Assimilation System, Bull. Am. Meteorol. Soc., **85**, 381-394, doi:10.1175/BAMS-85-3-381

Rusakoff, D., G. Ekström, and J. Tromp, 1997, A new analysis of the great 1970 Colombia earthquake and its isotropic component, J. Geophys. Res., **102**, 20,423–20,434, doi:10.1029/97JB01645

Shestakov, N.V., Ohzono, M., Takahashi, H. et al., 2014, Modeling of coseismic crustal movements initiated by the May 24, 2013, $M_w = 8.3$ Okhotsk deep focus earthquake, Dokl. Earth Sc. **457**, 976-981. doi:10.1134/S1028334X1408008X

Simons, F. J., F. A. Dahlen, and M. A. Wieczorek, 2006, Spatio-spectral concentration on a sphere, SIAM Rev., **48**, 504-536, doi:10.1137/S0036144504445765

Steblov, G. M., et al., 2014, First geodetic observations of a deep earthquake: The 2013 Sea of Okhotsk M_w 8.3, 611 km-deep, event, Geophys. Res. Lett., **41**, 3826–3832, doi:10.1002/2014GL060003

Sun, W., S. Okubo, G. Fu, and A. Araya, 2009, General formulations of global and co-seismic deformations caused by an arbitrary dislocation in a spherical symmetric earth model – Applicable to deformed earth surface and space-fixed point, Geophys. J. Int., **177**, 817-833, doi:10.1111/j.1365-246X.2009.04113.x

Sun, T., K. Wang, T. Iinuma, R. Hiro, J. He, H. Fujimoto, M. Kido, Y. Osada, S. Miura, Y. Ohta, and Y. Hu, 2014, Prevalence of viscoelastic relaxation after the 2011 Tohoku-oki earthquake, Nature, **514**, 84-87, doi:10.1038/nature13778

Swenson, S. C. and J. Wahr, 2006, Post-processing removal of correlated errors in GRACE data, Geophys. Res. Lett., **33**, doi:10.1029/2005GL025285

Syed, T. H., J. S. Famiglietti, M. Rodell, J. Chen, and C. R. Wilson, 2008, Analysis of terrestrial water storage changes from GRACE and GLDAS, Water Resour. Res., **44**, W02433, doi:10.1029/2006WR005779

Tamisiea, M.E., Mitrovica, J.X., Davis, J.L., 2007, GRACE gravity data constrain ancient ice geometries and continental dynamics over Laurentia. Science, **316**, 881-883

Tanaka, Y.-Y., S. Okubo, M. Machida, I. Kimura, and T. Kosuge, 2001, First Detection of Absolute Gravity Change Caused by Earthquake, Geophys. Res. Lett., **28(15)**, 2979-2981, doi:10.1029/2000GL012590.

Tanaka, Y.-Y., J. Okuno, and S. Okubo, 2006, A new method for the computation of global viscoelastic post-seismic deformation in a realistic earth model (I) – vertical displacement and gravity variation, Geophys. J. Int., **164(2)**, 273-289,

Tanaka, Y.-Y., J. Okuno, and S. Okubo, 2007, A new method for the computation of global viscoelastic post-seismic deformation in a realistic earth model (II) – horizontal displacement, Geophys. J. Int., **170(3)**, 1031-1052, doi:10.1111/j.1365-246X.2007.03486.x

Tanaka, Y.-Y., 2013, Theoretical computation of long-term postseismic relaxation due to a great earthquake using a spherically symmetric viscoelastic Earth model, J. Geod. Soc. Japan, **59**, 1-10 (in Japanese).

Tanaka, Y.-Y., T. Hasegawa, H. Tsuruoka, V. Klemann and Z. Martinec, 2015, Spectral-finite element approach to post-seismic relaxation in a spherical compressible Earth: application to the gravity field variations due to the 2004 Sumatra-Andaman earthquake, Geophys. J. Int., **200**, 299 – 321, doi:10.1093/gji/ggu391

Tanaka, Y.-S. and K. Heki., 2014, Long- and short-term postseismic gravity changes of megathrust earthquakes from satellite gravimetry, Geophys. Res. Lett., **41(15)**, 5451-5456, doi:10.1002/2014GL060559

Tanaka, Y.-S., K. Heki, K. Matsuo, and N. V. Shestakov, 2015, Crustal subsidence observed by GRACE after the 2013 Okhotsk deep-focus earthquake, Geophys. Res. Lett., **42**, 3204-3209, doi:10.1002/2015GL063838

Tanaka, Y.-S. and K. Heki, 2017, GRACE Seismilogy: Review and Perspective of Satellite Gravimetry for Earthquake Sciences, ZISIN (Journal of the seismological society of Japan), **69**, 69-85 (in Japanese).

Tapley, B.D., S. Bettadpur, J.C. Ries, P.F. Thompson, and M.M. Watkins, 2004, GRACE measurements of mass variability in the Earth system, Science, **305**, 503-505.

Tobita, M., 2016, Combined logarithmic and exponential function model for fitting GNSS time series after 2011 Tohoku-Oki earthquake, Earth, Planets and Space, **68(41)**, doi:10.1186/s40623-016-0422-4

Yoder, C.F.,Williams, J.G., Dickey, J.O., Schutz, B.E., Eanes, R.J. and B.D. Tapley, 1983, Secular variation of Earth's gravitational harmonic J coefficient from Lageos and non-tidal acceleration of Earth rotation, Nature, **303**, 757-762

Wahr, J., M. Molenaar, and F. Bryan, 1998, Time variability of the Earth's gravity field: Hydrological and oceanic effects and their possible detection using GRACE, J. Geophys. Res., **103**, 205-229

Wang, K., Y. Hu, and J. He, 2012, Deformation cycles of subduction earthquakes in a viscoelastic Earth, Nature, **484**, 327–332, doi:10.1038/nature11032

Wang, L., C. K. Shum, and C. Jekeli, 2012a, Grvitational gradient changes following the 2004 December 26 Sumatra-Andaman Earthquake inferred from GRACE, Geophysical Journal International, **191**, 1109-1118.

Wang, L., C. K. Shum, F. J. Simons, A. Tassara, K. Erkan, C. Jekeli, A. Braun, C. Kuo, H. Lee, and D. Yuan, 2012b, Coseismic slip of the 2010 Mw 8.8 Great Maure, Chile earthquake quantified by GRACE observation, Earth Planet. Sci. Lett., **335-336**, 167-179, doi:10.1016/j.epsl.2012.04.044

Zhan, Z., H. Kanamori, V. C. Tsai, D. V. Helmberger, and S. Wei, 2014, Rupture complexity of the 2994 Bolivia and 2014 Sea of Okhotsk deep earthquakes, Earth Planet. Sci. Lett., **385**, 89–96.

Zhang, G., W. Shen, C. Xu, and Y. Zhu, 2016, Coseismic Gravity and Displacement Signatures Induced by the 2013 Okhotsk Mw8.3 Earthquake, Sensor, **16(9)**, 1410, doi:10.3390/s16091410

Zhang, Z. –Z., B. F. Chao, Y. Lu, and H. –T. Hsu, 2009, An effective filtering for GRACE time-variable gravity; Fan filter, Geophys. Res. Lett., **36**, L17311, doi:10.1029/2009GL039459